The Pennsylvania State University

The Graduate School

INFLUENCE OF STRESS ON THE PERFORMANCE OF LEAD ZIRCONATE

TITANATE THIN FILMS

A Dissertation in

Materials Science and Engineering

by

Kathleen Coleman

Submitted in Partial Fulfillment

of the Requirements

for the Degree of

Doctor of Philosophy

December 2020

The dissertation of Kathleen Coleman was reviewed and approved by the following:

Susan Trolier-McKinstry
Professor of Ceramic Science and Engineering
Professor of Electrical Engineering
Dissertation Advisor
Chair of Committee

Clive A. Randall
Professor of Materials Science and Engineering

Jon-Paul Maria
Professor of Materials Science and Engineering

Brian Foley
Assistant Professor of Mechanical and Nuclear Engineering

Raul Bermejo
Special Member
Professor of Materials Science and Engineering
Montanuniversität Leoben

John C. Mauro
Professor of Materials Science and Engineering
Chair of Intercollege Graduate Degree Program in Materials Science and Engineering

Abstract

Lead zirconate titanate (PbZr$_x$Ti$_{1-x}$O$_3$, PZT) thin films are used in piezoelectric microelectromechanical systems (PiezoMEMS) such as sensors, actuators, and energy harvesting devices. The performance of PZT films depends on the piezoelectric response and the structural integrity of the piezoelectric film. Typically, films are driven to higher fields, stresses, and strain levels compared to bulk devices. The relationship between these large input signals, particularly high stresses, and the performance of these films needs to be quantified. This thesis investigates the influences of various stresses on the properties of PZT films and determines their mechanical limits.

With small changes in the stress state (~200 MPa), the piezoelectric, dielectric, and ferroelectric properties of PZT films may be tuned. The dielectric and piezoelectric properties of 0.6 μm thick {001} sol-gel Pb$_{0.99}\square_{0.01}$(Zr$_{0.52}$Ti$_{0.48}$)$_{0.98}$Nb$_{0.02}$O$_3$ (PZT) films on Si substrates and thin Ni foils were measured as a function of applied strain and total stress. These films are under different residual stresses arising from thermal expansion mismatch between the film and the substrate. With no additional applied stress, the remanent polarization, P_r was approximately 21 ± 0.2 μC/cm^2 and 39.5 ± 2.3 μC/cm^2 for PZT films on Si and Ni, respectively. The higher P_r on Ni originates from more "c" domains (out-of-plane polarization) due to the compressive stresses. The link between stress and domain orientation was further explored by applying uniaxial strains. PZT film on 50 μm Ni foil had uniaxial strains of -0.2% to 0.5% applied, while films on Si were only exposed to strains between -0.06 and 0.06%, because of substrate failure. When PZT films on Ni foil were under a 0.5% tensile strain, their P_r decreased by 7-10% and their relative permittivity increased by ~20% relative to zero applied strain. This trend reversed upon compressive strain. In addition, the piezoelectric coefficient, $e_{31,f}$ was -9.0 ± 0.45 μC/cm^2 and -7.1 ± 0.35 μC/cm^2 on Ni

and Si, respectively, and increased in magnitude with applied uniaxial compressive strain. These changes suggest some ferroelastic reorientation.

The extent of property changes with stress was also shown to differ for the films on Si and Ni. To explore the relationship between the tunability of properties with residual stress, the PZT films on Ni and Si were electrically characterized from 15 K up to room temperature. At room temperature, the dielectric irreversible Rayleigh parameter, α_{ray}, was 15.5 ± 0.1 and 28.4 ± 1.6 cm/kV for PZT on Si and Ni, respectively. The higher α_{ray} suggests more irreversible domain wall motion at room temperature, and may be explained by the lower stiffness on the Ni foil reducing the degree of clamping of these films. Below 200 K, α_{ray} for the PZT/Si sample exceeds that of the PZT/Ni sample. This is believed to arise from differences in the energy landscape of pinning centers for domain wall motion and was supported by Preisach analysis and the third harmonic phase angle results.

The second portion of this thesis focuses on understanding the mechanical limits of PZT thin films. Piezoelectric thin films are vulnerable to fracture, which results in degradation of the structural integrity and device performance. This work explores the fracture process in PiezoMEMS, which is a combination of a crack initiation event in the thin piezoelectric film followed by crack propagation through the subsequent layers. Biaxial bending tests, using the Ball-on-three-Balls (B3B) technique, were performed on stacks containing $Pb(Zr_{0.52}Ti_{0.48})O_3$ (PZT) thin films on thick (~500 μm) Si wafers.

First, a series of PZT films of varying thicknesses (i.e. 0.7 μm, 1.3 μm, or 1.8 μm) was tested using the B3B method to determine the relationship between crack initiation stress and film thickness. Crack initiation stress increased when the film thickness decreased. PZT films that were 0.7 μm thick required ~590 MPa to initiate a crack, where 1.8 μm thick films required only 490

MPa to crack. This trend was modeled using a finite fracture mechanics model that necessitates a coupled stress-energy criterion for crack initiation in brittle ceramics. In this model, it was shown that for PZT in this film thickness regime (0.1 to a few microns), the crack initiation stress depended on the thickness.

At higher loads, the entire stack would fail. First, a fracture would initiate in the PZT film, enter the LaNiO$_3$ layer, and arrest in the compressive SiO$_2$ layer. With higher loads, the crack could then propagate through the SiO$_2$ and Si layer, failing the entire stack. Weibull analysis shows a significant effect of the thin film thickness on the stack's strength. The characteristic strength and Weibull modulus were $\sigma_0 \sim 1110$ MPa and $m \sim 28$ for the stacks with the 0.7 µm thin PZT film stack, $\sigma_0 \sim 1060$ MPa and $m \sim 26$ for the 1.3 µm film stack, $\sigma_0 \sim 880$ MPa and $m \sim 10$ for the 1.8 µm film stack. This trend in crack propagation was rationalized using linear elastic fracture mechanics indicating the importance of the PZT layers thickness on the initial crack length and the stack's strength.

Since films are typically under electromechanical loading conditions, electromechanical failure was also explored by investigating the relationship between the direction of applied stress and failure pattern. Cracks consistently propagated perpendicular to the maximum tensile stress direction and connected thermal breakdown events, suggesting correlations between electrical and mechanical failure. Additionally, the influence of electric history on the crack initiation stress was also determined using the B3B method. Electrical fields are important for enhancing the properties of piezoelectric thin film, but in this thesis, have been shown to decrease the mechanical load the films can withstand. For 1.6 µm thick PZT films, the crack initiation stress was reduced by ~15% when it was poled or under a DC bias compared to a virgin film. This may be due to a reduction in domain wall motion when poled, or development of local strain from some ferroelastic domain

reorientation with an applied field.

Overall, residual stress in PZT thin films was shown to influence the properties; at lower applied stress level these properties can be tuned. At higher stresses (around 500 MPa), cracks initiate in the PZT films and the thickness and the electrical history of the PZT layer affects the crack initiation stress. At stress levels greater than 800 MPa, failure was observed in the multilayer stack, as the crack that initiated in the PZT layer would then propagate through the underlying layers. These trends observed in this thesis will allow for further commercialization and improved performance of thin films. Additionally, the methods, models, and calculations used in this study can be expanded to other piezoelectric thin films, brittle ceramic coatings, and multilayers stacks.

Table of Contents

List of Figures

List of Tables

Acknowledgements

First of all, I would like to thank my advisor, Professor Susan Trolier-McKinstry. She has invested a tremendous amount of time in me during my studies at Penn State. I met Dr. Trolier-McKinstry at the Penn State open house and from her presentation and our conversations, I realized she was a caring, dedicated, hardworking, and humble professor. These qualities make her an incredible scientist and mentor. She has helped me over the course of this Ph.D. by challenging me, teaching me, encouraging me, and supporting me. I would not have flourished without her. I will always strive to be as sincere, dedicated, and thorough in my career as she is. Thank you Dr. McKinstry—it has been a true pleasure learning and working with you.

Secondly, I would like to thank my committee member, Raul Bermejo. Raul visited Penn State during my second year of graduate school, and after his colloquium talk, we had lunch and discussed ways that we could collaborate. Raul taught me the fracture mechanics of ceramics, stress-energy coupled criterion for crack initiation, the ball on three ball (B3B) test, and linear elastic fracture mechanics. In addition, Raul invited me to work at the Institute for Structural and Functional Ceramics at the University of Leoben. Raul, Eva, and their three kids (Nora, Emil, and Theo) gave me a very warm welcome as I arrived in Austria. Thanks, Raul, for taking me on and teaching me a lot even from abroad.

In addition, I would like to thank my extremely knowledgeable and approachable committee. First, Clive Randall, who would often stop by my desk to discuss my CDP project. He suggested books and ideas to explore, which was always a delight. After my candidacy exam, he offered to teach me a course on the fundamentals of ferroelectrics to help me make the bigger connections. These discussions both in MSC and Liberty helped me develop the fundamentals, but also made me think about connections to other areas of materials science. I would also like to thank

Brian Foley, who even back at the 2017 ISAF conference was excited to discuss research and collaborate. I also thank Jon-Paul Maria who taught me an excellent course on electroceramics. He is an excellent instructor and helped me make bigger connections. Both JP and his group have been very approachable, and helpful.

In addition to my committee, I would like to thank Julian Walker, who was a postdoctoral scholar in the STM group for my first two years in graduate school. He guided me through the initial ropes of our Center for Dielectrics and Piezoelectrics (CDP) project. Julian would stay late in the cleanroom and give up weekends to help me reach deadlines. He always answered my knocks to his door to fix equipment, discuss good or bad results, and answer my questions. He also would discuss my future career and find good collaborators for our project. Being able to go to Julian's office made everything those first few year more manageable and helped me enjoy this research.

I would also like to acknowledge and thank several collaborators on this work. First Brendan Hanrahan, who approached me after a CDP meeting to try measuring pyroelectric coefficients on PZT on Ni and Si. He taught me about pyroelectricity and phenomenology, and this led to a nice study. Secondly, I would like to thank Maximillian Ritter, who was a fantastic master student in Leoben, who came to Penn State to execute several B3B studies with me. It was a great summer being able to work with you. I would also like to thank the entire ISFK (particularly Josef Kreith, Robert Danzer, Peter Supancic, Irena Kraleva, and Walter Harrer) and the ESI (Markus Alfreider, and Daniel Kiener) for their help when I visited the University of Leoben. In addition, I would like to thank Dominique Leguillon who help us model several crack-initiation studies for PZT films, which complemented our experimental results quite nicely. I would also like to thank Herb McKinstry for helping update the model for the Preisach data. I would also like

discussions with them and they have all been excellent co-workers, friends, and this group dynamic made all the difference.

I would also like to thank the MRI nanofabrication staff. In particular, I would like to acknowledge Beth Jones for teaching me to make PZT samples, answering my questions, and for all of our pleasant conversations and laughs. Guy Lavallee for a tremendous help in making nearly impossible samples for me while I was in Austria and training me on several etch tools. I know I was "trouble". I would also like to thank Mike LaBella and Kathy Gehoski who helped with the lithography of these challenging samples. I would also like to thank Kathy for driving me home when I became extremely sick in the cleanroom one day. I would also like to thank Bill Drawl, Bangzhi Liu, Shane Miller, Andy Fitzgerald, and Bill Mahoney for training me on several pieces of equipment. They always encouraged me even if I was timid and answered my questions. I also enjoyed all of our conversations in the gowning room. I would also like to thank the material characterization staff. In particular, I would like to thank Nichole Wonderling, Gino Tambourine, Maria Dicola, Manuel Villalpando, and Tanner Mengle for their help. In the electrical characterization lab, I would like to thank Jeff Long for always checking equipment and explaining some basic electrical circuitry to me. He also would generously lend me expensive pieces of equipment that I have dragged around campus for various experiments. I would also like to thank Dr. Libby Kupp, and Sarah Eichfeld for additional help with experiments, equipment, and lab safety.

I would also like to acknowledge the larger MRI community, the CDP community, and the Materials Science and Engineering Department at Penn State, where everyone has been willing to collaborate and despite being in different groups and even different buildings, and in the case of CDP, different universities, countries, and companies. In particular I would like to thank Hayley

Coley, the MatSE graduate coordinator as well as Joanne Aller and Brenda Gainey, the CDP administrative assistants. I would also like to thank many graduate students, and post docs, who all have helped me in one way or another complete this thesis and my Penn State journey. Thank you: Timothy Walter, Nisha Sheth, Kayla Cooley, Jess Kopatz, Thorsten Bayer, Jason Lapano, Jared Carter, Lisheng Gao, Kosuke Tsuji, Mike Vecchio, Mengxue Yuan, Jiawei Luo, Nate Martin, Ama Agyapong, Beecher Watson, Tom Nigl, Alex Wilson-Heid, Joseph Roth, Alex Molina, Hari Padmanabhan, Sun Hwi Bang, and many others.

I would also like to acknowledge those that have not directly invested in this research but my growth as a materials scientist, engineer, and researcher. I would first like to thank many friends and mentors from UConn (Sam Brown, Megan Gauer, Laura Wilcox, Emily Bousaada, Aliya Carter, Jess Guerrera, Tori Radovic, and Christine Doherty), and the Institute for Material Science (Avi Dongare, Rainer Hebert, Radenka Maric, and Bryan Huey). I would like to acknowledge the UConn Engineering diversity and outreach center, the Bridge program, and especially the director Kevin McLaughlin who invested so much in me and helped me become a confident and understanding leader and engineer. Thank you all for supporting me through this graduate school journey from afar.

Last but far from least, I would like to thank my family— especially my parents, my brother Michael, my sister Maryanne, my Granny Nonie, and my Grandma Sammon. My dad was the first person to encourage me to consider engineering and every morning as I walked to school, he would always be sure I had a ham sandwich and weather permitting a snowball. My family has always encouraged me regardless of how much they understood and have been there in all the ups and downs. My mom, my Grandma Sammon, and my Granny were my first teachers. My grandmothers have always been role models and they worked hard and gave up so much, which has allowed me

to have this opportunity. I'll never forget my Grandma Sammon's math lessons, where I could not leave the table until I recited my times tables as fast as she could ask them. She was persistent and said math was so important and her favorite subject. Despite the aggravating lessons and tears, math has always been my favorite too. While she will never see this work, she is always with me and for the rest of my life I will "strike the nail a'right" and "give to the world the best I can." I can only hope she would say "*go maith*" to the work in this thesis, as if we finished a math lesson. Thank you.

Note: The findings and conclusions in this thesis do not necessarily reflect the view of the funding agency.

Chapter 1.   Motivation and Thesis Organization

This chapter outlines the motivation for the work described in this thesis and the contents of the following chapters. **Section 1.1** gives a brief overview of various applications of thin film ferroelectrics. **Section 1.2** defines various metrics used to assess the performance of several thin film devices. **Section 1.3** gives a short overview of the work done in the following chapters.

1.1   Ferroelectric Thin Film Applications

Ferroelectric thin films are utilized in various devices, including piezoelectric microelectromechanical systems, also called piezoMEMS (sensors, actuators, and energy harvesting devices [1,2]), infrared imagers [3,4], thermal energy harvesters [4–7], heat detectors [8–12], and memory devices [13]. These devices contain multilayer stacks composed of active ferroelectric thin film layers and their electrodes, with additional layers for adhesion and support. Commercially, the demand for sensors, self-powered and miniaturized devices has increased due, in part, to the Internet of Things (IoT). Therefore, the development of thin film ferroelectrics, pyroelectrics, and piezoelectrics devices is of increasing interest.

Materials with high pyroelectric and piezoelectric coefficients, such as lead zirconate titanate with a morphotropic phase boundary composition of $Pb(Zr_{0.52}Ti_{0.48})O_3$ (PZT) [1,2,14], are typically used in high sensitivity sensors and large displacement actuators. Due to the demand for higher outputs, many of these devices optimize the thickness of the piezoelectric film and drive the film in rather harsh conditions. For example, energy harvesters require flexible stacks to reach higher strains and achieve greater power densities [15–17]. As a result, the film can be under tremendous strain. Changing the substrate and residual stress in the film can tune the film's domain structure and thus its piezoelectric response [15,18–20], improving device performance. Initial

studies have suggested these stresses may also alter the breakdown strength [21]. Due to the differences in microstructure and loading conditions, the fundamental relationship between stresses in the film and its performance must be determined.

1.2   Factors that Influence Performance

The performance of piezoMEMS depends both on the piezoelectric or pyroelectric properties of the film and the structural limits of the device. For example, in energy harvesters, the power output (**Equation 1-1**) [22] depends on the figure of merit (FoM) of the film (**Equation 1-2**), as well as the strain (*x*) the piezoelectric layer can withstand [16,22].

$$P_{rms} = \frac{\omega}{4} \left(\frac{e_{31,f}^2}{\varepsilon_o \varepsilon_{33}^T} \right) (At) x_i^2 \tag{1-1}$$

where P_{rms} is the root mean square of power, ω is the frequency, ε_o is the permittivity of free space, and ε_r is the relative permittivity of the piezoelectric film. *A* and *t* are the area and thickness of the piezoelectric film, respectively.

$$\text{FoM} = \frac{e_{31,f}^2}{\varepsilon_r} \tag{1-2}$$

Other piezoMEMS and pyroelectric devices have different FoMs. **Equation 1-3** and **Equation 1-4** shows the FoM for voltage-based and charge-based sensors, respectively [23–25] and **Equation 1-5** shows that of actuators [25,26].

$$\text{FoM} = g = \frac{d}{\varepsilon_o \varepsilon_r} \tag{1-3}$$

$$\text{FoM} = e_{31,f} \tag{1-4}$$

$$\text{FoM} = e_{31,f} \tag{1-5}$$

As shown by **Equations 1-1** through **1-5**, each application has different requirements. This thesis aims to understand the influences of stress on the performance of lead zirconate titanate thin films, so that the performance of such films can be enhanced. The relationship between the total stress in the film and its observed properties and structural limits are investigated.

1.3   Dissertation Overview

The following chapters of this thesis probe the relationship between stresses in PZT films and the functional properties. **Chapter 2** outlines the background and previous work that has been done in the field of piezoelectrics and ferroelectrics. Additionally, **Chapter 2** introduces the lead zirconate titanate (PZT) system, with an emphasis on similarities and differences of PZT films versus bulk ceramics. **Chapter 3** discusses the effects of total stress in PZT films on the dielectric and piezoelectric properties. These results show how stresses can tune film properties and the importance of residual stresses on domain structure. This is further explored in **Chapter 4**, where the differences in the domain structure of films with different residual stresses were investigated from 10 K to room temperature. These results suggest differences in the energy barrier landscape of pinning sites as a function of the residual stresses in the films.

Chapter 5 explores the mechanical limits of PZT thin films as a function of thickness and suggests the failure strains of films are greater than that of bulk counterparts. The experimental results were compared with a finite fracture mechanics model. **Chapter 6** examines changes in the crack initiation when films are loaded both electrically and mechanically. The electrical history is shown to affect both the properties and the stress the film can withstand. This was attributed to the domain structure changes with field. The results establish the limits for electromechanical failure on PZT thin films, which is critical to exploitation of these films in piezoMEMS. These

relationships are summarized in **Chapter 7**. **Chapter 7** also outlines future directions for the studies that are presented in this thesis.

Chapter 2.   **<u>Introduction and Background</u>**

This chapter overviews the literature that laid the foundation for the work done in this thesis. **Section 2.1** discusses the properties of piezoelectricity and electrostriction, **Section 2.2** defines pyroelectricity, **Section 2.3** introduces ferroelectricity. **Section 2.4** discusses the nonlinear nature of ferroelectrics and defines intrinsic and extrinsic contributions to their properties. **Section 2.4.1** and **Section 2.4.2** go through the electrical techniques of Rayleigh and Preisach analysis, respectively, to quantify the nonlinear behaviors of ferroelectrics. **Section 2.5** discusses lead zirconate titanate, the material of interest of this thesis.

2.1   Piezoelectricity

Piezoelectrics are materials that exhibit a coupling between electrical and mechanical energy. For example, when a stress (σ) is applied to a piezoelectric material, a dielectric displacement (D) will develop; this is given by **Equation 2-1,** where d_{ijk} is the piezoelectric charge coefficient [8,27].

$$D_i = d_{ijk}\sigma_{jk} \tag{2-1}$$

This relationship is known as the direct piezoelectric effect. Additionally, if an electric field (E) is applied, the piezoelectric material's shape will change, creating a strain (x); this is known as the converse effect as defined by **Equation 2-2**.

$$x_{ij} = d_{kij}E_k \tag{2-2}$$

The direct effect is typically used in sensors and energy harvesters, while the converse effect is used in actuators.

There are a number of piezoelectric coefficients that have been defined to relate either stress or strain to polarization or field [8,28]. The piezoelectric coefficient e is used through this thesis and is defined by **Equation 2-3.**

$$\text{Direct effect: } D_i = e_{ikl}x_{kl} \qquad\qquad \text{Converse effect: } \sigma_{ij} = -e_{kij}E_k \qquad (2\text{-}3)$$

The piezoelectric coefficients g and h are defined in **Equation 2-4** and **Equation 2-5,** respectively. The coefficients reported depend on the application and measurement methods used [28] .

$$\text{Direct effect: } E_i = -g_{ijk}\sigma_{jk} \qquad\qquad \text{Converse effect: } x_{ij} = g_{kij}D_k \qquad (2\text{-}4)$$

$$\text{Direct effect: } E_i = -h_{ijk}x_{jk} \qquad\qquad \text{Converse effect } \sigma_{jk} = -h_{ijk}D_i \qquad (2\text{-}5)$$

Piezoelectricity is the linear response between changes in polarization and the mechanical stress in the material. Thus, a material needs to be non-centrosymmetric to exhibit this third rank tensor. Of the 32 crystallographic point groups, 21 groups are non-centrosymmetric [27,29,30]. However, the point group 432, while not centrosymmetric, has other symmetry elements that prevent piezoelectricity [27,29,30]. As a result, only 20 of the point groups have this property. While piezoelectricity is a third rank tensor, it is often reported using matrix notation. In this thesis, e_{311} is reported using matrix notation as e_{31}.

Because thin films are clamped to their substrates, it is not possible to measure the true e_{31} (e.g. while the in-plane strains are known, the out-of-plane strain is not known during measurement. Instead, the out-of-plane stress is known (and is typically zero). As a result, an effective piezoelectric coefficient $e_{31,f}$ which accounts for the mixed boundary conditions is defined by **Equation 2-6** [24,31].

$$e_{31,f} = \frac{-\sigma_1}{E_3} = e_{31} - e_{33}\left(\frac{c_{13}}{c_{33}}\right) \qquad (2\text{-}6)$$

Piezoelectricity can be used in many applications including timing standards, inkjet printers, ignitors, and in piezoelectric microelectromechanical systems (piezoMEMS) such as sensors, actuators, piezoelectric micromachined ultrasonic transducers (pMUT), and energy harvesters [1,32].

2.2 Pyroelectricity

A subset of the piezoelectric point groups exhibits pyroelectricity. Pyroelectric materials have a spontaneous polarization; the magnitude and/or the direction of the polarization is a function of temperature, as defined by **Equation 2-7** [8].

$$\Pi_i = \left(\frac{dP_i}{dT}\right) \qquad (2\text{-}7)$$

Of the 20 crystallographic point groups, only 10 exhibit a unique polar axis; these are referred to as the polar point groups. Pyroelectric thin films are used in a variety of applications including infrared imagers [3,4], thermal energy harvesters [4–7], and heat detectors [8–12].

2.3 Ferroelectricity

In certain pyroelectrics, the spontaneous polarization can be switched to other polarization directions (defined by their crystal structure), under an applied electric field; this subclass of pyroelectrics is known as ferroelectric materials. Some features of the crystal that favor the observation of ferroelectricity include: d^0 ions (like Ti^{4+}), atoms with lone electron pairs (like Pb^{2+}), and displacements relative to a prototype phase that are small enough to allow for reorientation but large enough to exceed the amplitude of thermal vibrations in the system [29]. Not all pyroelectrics are ferroelectric; sometimes an extremely large electric field would be required to reorient the spontaneous polarization and this may be much greater than the electrical breakdown strength of the material.

In many ways, ferroelectrics are the electrical analog to ferromagnets. At high temperatures, most ferroelectrics undergo a phase transformation to a paraelectric phase [27]. As a result, the system transitions from a polar ferroelectric to a non-polar paraelectric phase. The transition temperature is known as the Curie temperature (T_c), analogous to ferromagnets. Above this transition, the dielectric constant (ε_r) follows Curie-Weiss behavior, described in **Equation 2-8**, where θ is the Curie-Weiss temperature [27].

$$\varepsilon_r = \varepsilon_0 + \frac{C}{T-\theta} \qquad (2\text{-}8)$$

If the ferroelectric transition is second order, then θ is T_c. However, for a first order transition, θ is lower than T_c [27].

When a ferroelectric is cooled below T_c, the spontaneous polarization increases and ferroelastic strain increases. Due to the multiple possible orientations for the spontaneous polarization and the drive to lower both the strain and depolarization energy, ferroelectrics form regions with different spontaneous polarization directions [8]. Each region that has the same spontaneous polarization direction (or at least nearly so) is defined as a domain. The allowed polarization direction of the domains in the system depends on the crystal structure and the symmetry lost on cooling through T_c.

Domain walls separate domains and are described by the angle between the polar axis between the two domains in the system. The various domain walls are typically broken up into two categories, 180° domain walls and non-180° domain walls. 180° domain walls are only ferroelectrically active; an electric field must be applied for the domain wall to move. However, non-180° domain walls are both ferroelectrically and ferroelastically active, and therefore can move due to either an applied electric field or a mechanical force. This results in a change in polarization and strain in the material. As a result of the various polarization orientations of each

8

of the domains, most ferroelectrics will have no net remanent polarization upon cooling [8,27]. However, when an electric field is applied, domains can be reoriented to align in the direction of the field and give rise to their signature polarization electric field (P-E) hysteresis loop. This is shown in **Figure 2-1**.
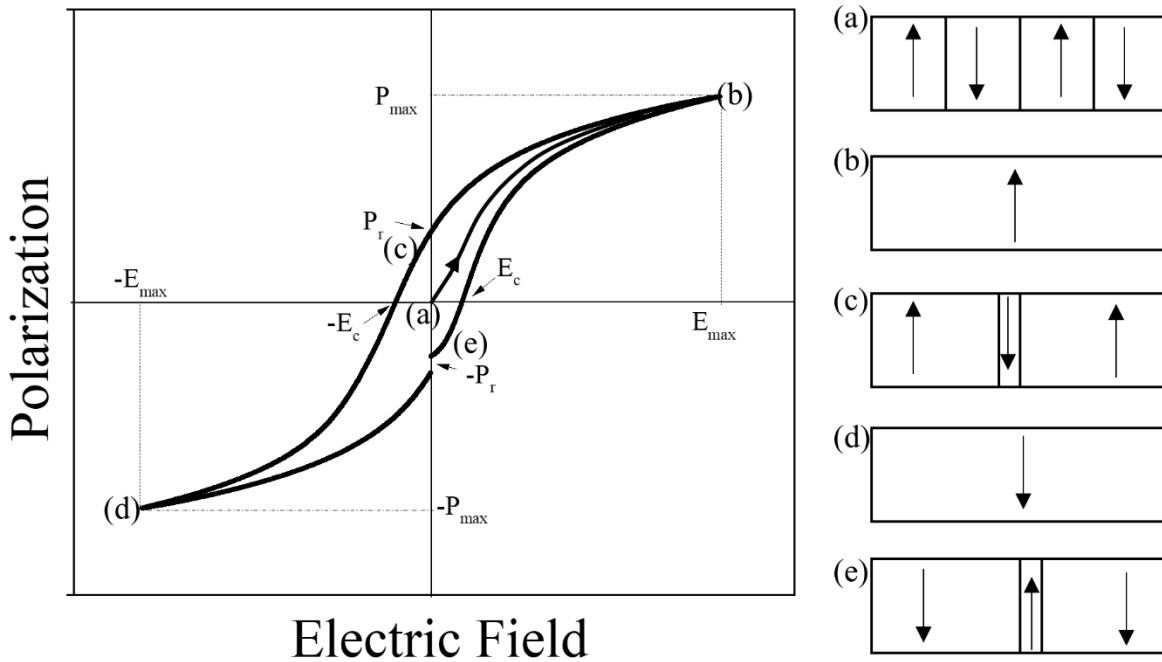
Figure 2-1 Polarization-Electric field (P-E) hysteresis loop from a lead zirconate titanate sample. The remanent polarizations ($+P_r$ and $-P_r$) are defined as the net polarization remaining in the sample when field is removed, and the coercive fields ($+E_c$, and $-E_c$) are the fields required to return the polarization to zero. (a)-(e) show schematics of the domain structure at various points on the hysteresis loop. The domain structures shown are for an appropriately aligned single crystal.

As described above, a cooled sample under no applied field has a random domain structure and no net polarization, as shown in **Figure 2-1a.** With the application of a *small* electric field, a linear increase of the polarization (*P*) occurs, as described by **Equation 2-9**.

$$P= \varepsilon_0(\varepsilon_r-1)E \qquad (2\text{-}9)$$

As the field is increased, the linear relationship does not hold. At intermediate fields, domain walls move, leading to an increase in the permittivity. At even higher fields, in the limit of an appropriately oriented single crystal, domains with a polarization direction parallel to the applied field nucleate and grow, increasing the nonlinearity significantly [14]. Ideally, the resultant ferroelectric will contain one domain aligned with the electric field direction, as depicted schematically in **Figure 2-1b**. With the removal of the field, the ferroelectric should retain its polarization. However, local strains and electrical fields cause some back switching and reduce the polarization [14]. Therefore, the remaining polarization at zero field is known as the remanent polarization (P_r). As a negative electric field is applied, there will be some nucleation of new domains with the reverse polarization direction or one most nearly aligned with the electric field direction, as shown by **Figure 2-1c**. At a certain field level, the net polarization will reach zero as domains in the opposite direction begin to nucleate and grow. This x-intercept of the hysteresis loops is known as the coercive field (E_c). As the reverse field's magnitude increases, the domains nucleate and grow until the domain state saturates, as shown by **Figure 2-1d**. Again, the removal and reversal of the field will change the domain structure, as shown in **Figure 2-1e**.

For each ferroelectric, the hysteresis loop will show a characteristic P_r and E_c. The loop shape will depend on frequency [33]. Therefore, loops should only be compared at the same maximum field and frequency. Hard ferroelectrics have a larger E_c than soft ferroelectrics. The shape of the loop should be well saturated. An unsaturated loop could be caused by a leaky loop or a minor loop where a higher field is required to reach full saturation [34]. Differences in the magnitude of $+E_c$ and $-E_c$ as well as in $+P_r$ and $-P_r$ can be used to characterize imprint in the ferroelectric, likely due to a favored polarization direction. This is usually caused by dopants and the defect chemistry in the sample [35]. Overall, the shape of the hysteresis loop and the values of

P$_r$ and *E$_c$* are one characteristic of the quality of the ferroelectric sample. They also determine the sample's piezoelectric and pyroelectric responses, which are proportional to *P$_r$*.

2.4   Nonlinearity

As the hysteretic response of ferroelectric materials shows, there is an electric field amplitude dependence of the polarization response. This is also seen in the piezoelectric and dielectric response. **Equation 2-9** is only valid at low fields for ferroelectrics, since ε depends on the driving fields. **Equation 2-10** shows the higher order terms [36].

$$P = P_o + \alpha_1 E + \alpha_2 E^2 + \alpha_3 E^3 + \alpha_4 E^4 + \cdots \tag{2-10}$$

This nonlinearity is extremely important as it can increase the material's response. To understand these nonlinear behaviors, it is essential to distinguish between various contributions to the dielectric and piezoelectric properties. In ferroelectric ceramics, both intrinsic and extrinsic contributions are responsible for the primary dielectric, pyroelectric, and piezoelectric material responses. Intrinsic contributions arise from the changes in the unit cell and the average response of a single domain. Extrinsic contributions are due to motion of boundaries in the materials, which includes domain wall motion and phase boundaries.

Thus, the nonlinearity can be explained by extrinsic contributions such as domain wall motion. Domain wall motion depends on any local electric or elastic fields in the material. For example, various defect dipoles can pin domain wall motion by creating local electric fields. Additionally, local strains may act to pin the motion of non-180° domain walls. Certain defects require higher energies for domain wall motion than others, creating a distribution of barrier heights for domain wall motion. This is shown in **Figure 2-2a.** When the energy supplied by an applied electric field is small with respect to the energy barrier, the domain wall may only displace slightly within the potential well and will return to its original position with the removal of the

field. This is referred to as reversible domain wall motion. An example of this is shown in **Figure 2-2b**. When the applied field allows a domain wall to overcome the barrier height, the domain wall can move to another well, resulting in hysteresis and non-linear behavior; this is known as irreversible domain wall motion (**Figure 2-2c**).
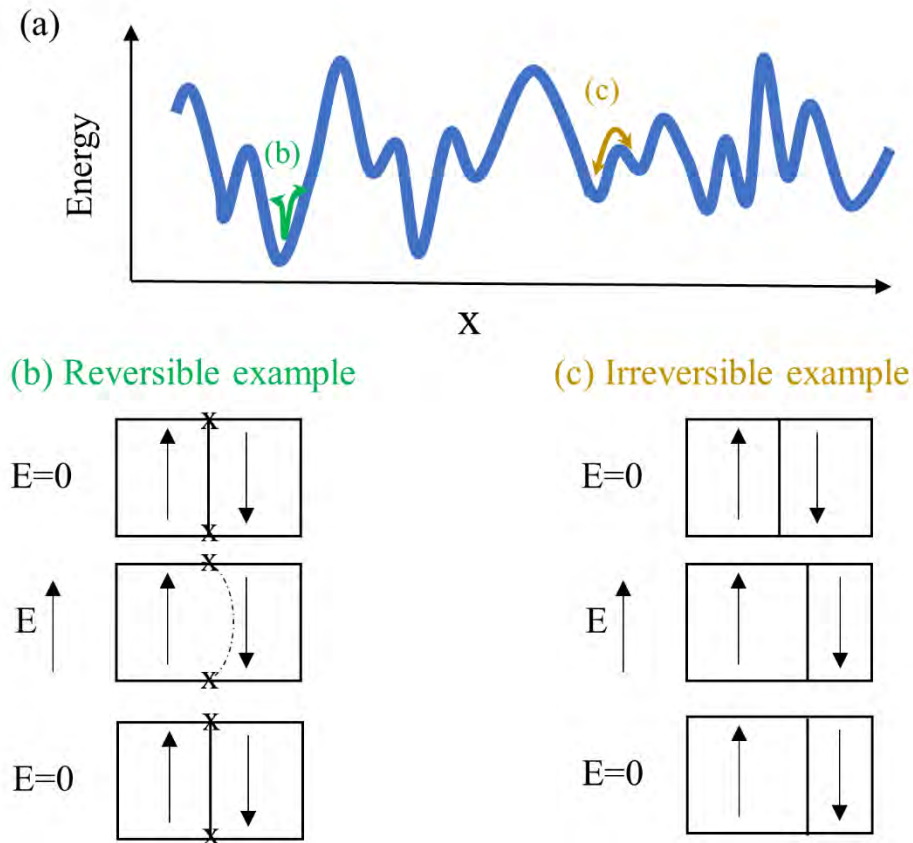
Figure 2-2. Energy landscape for pinning centers vs. position of domain wall. (a) shows an example of reversible domain wall motion where the domain wall is fully pinned to one potential well, and (b) shows irreversible domain wall motion where the domain wall can overcome the barrier height and move. Pinning sites are denoted by X.

2.4.1 Rayleigh Law

Domain wall motion can be understood in terms of the pinning and unpinning of these walls from their original position, depending on the potential energy landscape, as schematically

shown in **Figure 2-2a**. This has been described for both ferromagnets and ferroelectrics. For ferromagnets, the linear dependence of the permeability on the magnetic field was first observed by Lord Rayleigh [37] and further described by Neel [38,39], defining the Rayleigh Law. This law states that for an intermediate field regime there is a linear change in the permeability as a function of field amplitude, which is due to the motion of magnetic domain walls through a potential energy landscape with a Gaussian distribution of restoring forces [40–42].

While the Rayleigh law was originally applied to magnetic permeability in ferromagnets, it also holds true for the piezoelectric and dielectric response of many ferroelectrics [40–42]. The Rayleigh regime is typically observed for AC electric fields with amplitudes up to roughly half of E_c. The Rayleigh law (**Equation 2-11** and **Equation 2-12**) shows the linear relationship between sub-switching ac fields and the measured property [40–42]. The Rayleigh parameters ε_{init} and d_{init} describe the sum of the intrinsic and reversible domain wall motion contributions to the ε_r and d, respectively. α_{Ray} describes irreversible domain wall motion contribution to the properties [40,42]. This reversible domain wall motion is favored for domain walls in deep local minima in the potential distribution (as shown by the green arrows in **Figure 2-2**), and irreversible motion occurs when the interface moves from one potential energy well to another (as shown by the brown arrow in **Figure 2-2**).

$$\varepsilon_r = \varepsilon_{init} + \alpha_{Ray}E_{ac} \qquad (2\text{-}11)$$

$$d = d_{init} + \alpha'_{Ray}E_{ac} \qquad (2\text{-}12)$$

Various values for the Rayleigh coefficients have been reported in the literature for the same material systems [15,40,42–44]. It has been shown that the values will depend on defect concentrations [35,45], clamping state [43,46–48], substrate choice [44], sample thickness [15,49,50], grain size [42,51], stresses [47,52], and composition [51].

13

2.4.2   Preisach Analysis

Rayleigh behavior is only valid for a random Gaussian distribution of potential energy barriers for domain wall motion, and for sub switching fields. In fact, the Rayleigh law is not valid for all ferroelectrics, including some samples of $BaTiO_3$ [53], and is not always valid even at all sub-coercive fields [54]. For a more general approach, Preisach analysis and first order reversal curves (FORC) can be used to understand the hysteresis behavior over larger field ranges, without requiring assumptions on the potential energy landscape [55–58]. The Preisach distribution can give valuable insight to the local coercive fields which may depend on the pinning of domains through imprinting [35,45] and the variation in stresses [47,52] and clamping [47,48] of the films.
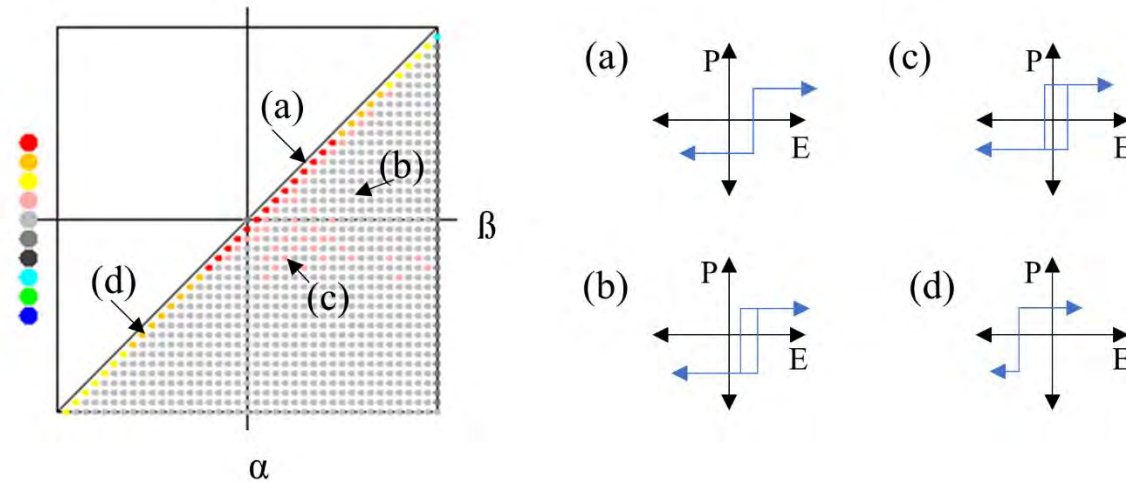
Figure 2-3. A schematic representation of the Preisach distribution on an α vs β plot (otherwise known as the Preisach plane). At four points on the plot the hysteron's P-E loops are represented schematically. The color bar (far left) represents the intensity at each (α, β) point, where the red circles is the highest intensity and blue is the lowest in this schematic example.

Preisach modeling can be used to describe switching in a ferroelectric [55–58] for an arbitrary electrical excitation. Instead of describing nucleation and growth, this model assumes that the ferroelectric response of a material consists of a series of rectangular hysteresis loops defined as hysterons which are distinguished by their upwards switching field (α), and downward

switching field (β) [56]. It is assumed that there are only upward and downward switching states, and $\alpha \geq \beta$. **Figure 2-3** shows a schematic of a Preisach distribution and the various hysterons based on their location on the α-β plot. When $\alpha=\beta$ (such as (a) and (d) in **Figure 2-3**)**,** the hysteron is reversible and when $\alpha \neq \beta$ (such as (b) and (c) in **Figure 2-3**), the hysteron is irreversible.

The distribution of these hysterons gives rise to the polarization of the ferroelectric, as described by **Equation 2-13** [56].

$$P=q(\alpha>\beta)\iint(\alpha,\beta)\cdot P_{irr}(\alpha,\beta)d\alpha d\beta + k(\alpha)\cdot P_{rev}(\alpha)\int d\alpha. \quad\quad (2\text{-}13)$$

P_{irr} and P_{rev} are the irreversible and reversible Preisach distributions and indicate the range of fields required for upward and downward switching in the ferroelectric. First order reversal curves (FORC) loops may be used to determine the Preisach distribution, as shown in **Figure 2-4.** When the applied field is increased up to a given field value, all of the hysterons that have an α value less than or equal to that field will contribute to the polarization. This is shown by the green square in **Figure 2-4b.** When the field is removed, certain hysterons will switch to the opposite polarization once the field is reduced to their β value, as shown in the purple square (**Figure 2-4c**). As the field is increased again, as shown by the blue square (**Figure 2-4d**), some hysterons will switch back. There is some path dependence and memory in the polarization behavior of some of the hysterons; these hysterons did not switch back when their β field was not reached on the field down section. As higher fields were reached, this observed memory was lost when all the hysteron aligned in the same direction, as shown by the orange square (**Figure 2-4e**).
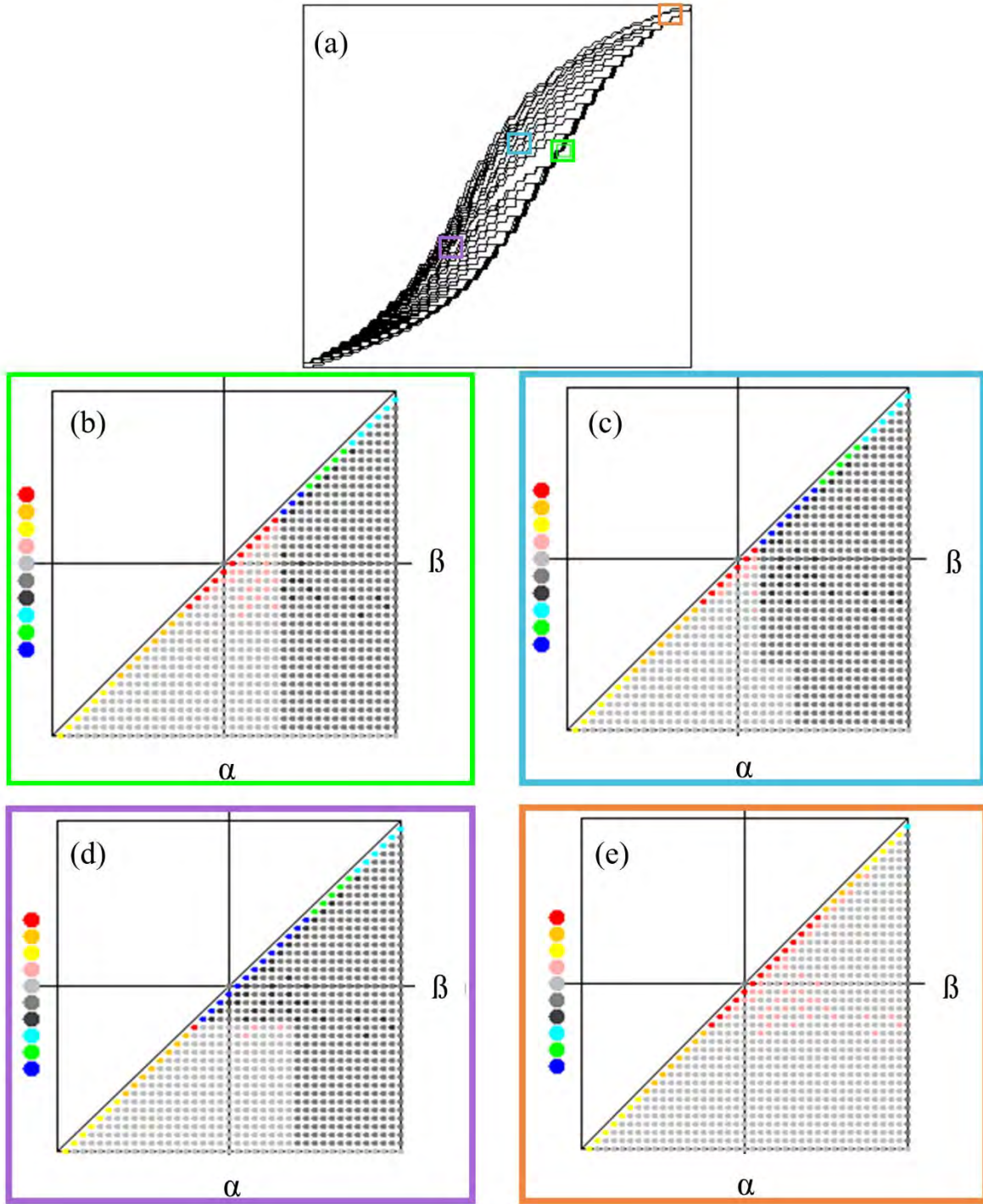
Figure 2-4. FORC reversal curves (a) showing the various minor P-E loops of a PZT film. (b-e) shows the Preisach hysteron distribution for PZT at a given field based on the field applied to the sample. The light and darks shades of the hysteron distribution represent upward and downward polzarization directions for the hysteron, respectively. The legend of circle colors from blue up to red represent increasing number of hysterons with the various values of α and ß.

2.5   Pb(Zr, Ti)O₃ Systems

Many useful ferroelectric materials have a distorted perovskite structure. The prototype perovskite structure is a cubic ABX_3 structure with point group $m\bar{3}m$. **Figure 2-5a** shows the cubic perovskite structure, where the corners have the larger A site cation, the center of the faces have the anion (typically O), and at the center of the cell is the B site, which is usually a smaller cation. Below the T_c, this perovskite structure can be distorted in one of many polar phases, including a tetragonal (point group 4mm) and rhombohedral (point group 3m) phases. For the tetragonal phase the unit cell is distorted by elongation in one of the six <100> directions where the B moves towards one of the oxygens. In the rhombohedral phase, the B ion moves along the body diagonals towards three of the oxygens.

These ferroelectric phases are derivative structures of the paraelectric $m\bar{3}m$ phase. The number of polarization directions come from the number of lost equivalent points from the stereographic projection. For example, the cubic $m\bar{3}m$ phase has 48 equivalent points, and the tetragonal 4mm phase (**Figure 2-5b**) has 8 equivalent points, which is $1/6^{th}$ the number of equivalent points resulting in 6 polar directions. There are 6 polar directions along <001> directions. From these polarization directions, the angle between two adjacent domains in a tetragonal perovskite phase would be 180° and 90°. Thus, the boundary between these walls are referred to as 180° domain walls or 90° domain walls, respectively. The rhombohedral 3m phase (**Figure 2-5c**) has $1/8^{th}$ the equivalent points of $m\bar{3}m$ and has 8 directions along <111>, which gives rise to possible 180°, 109° or 71° domain walls.

17
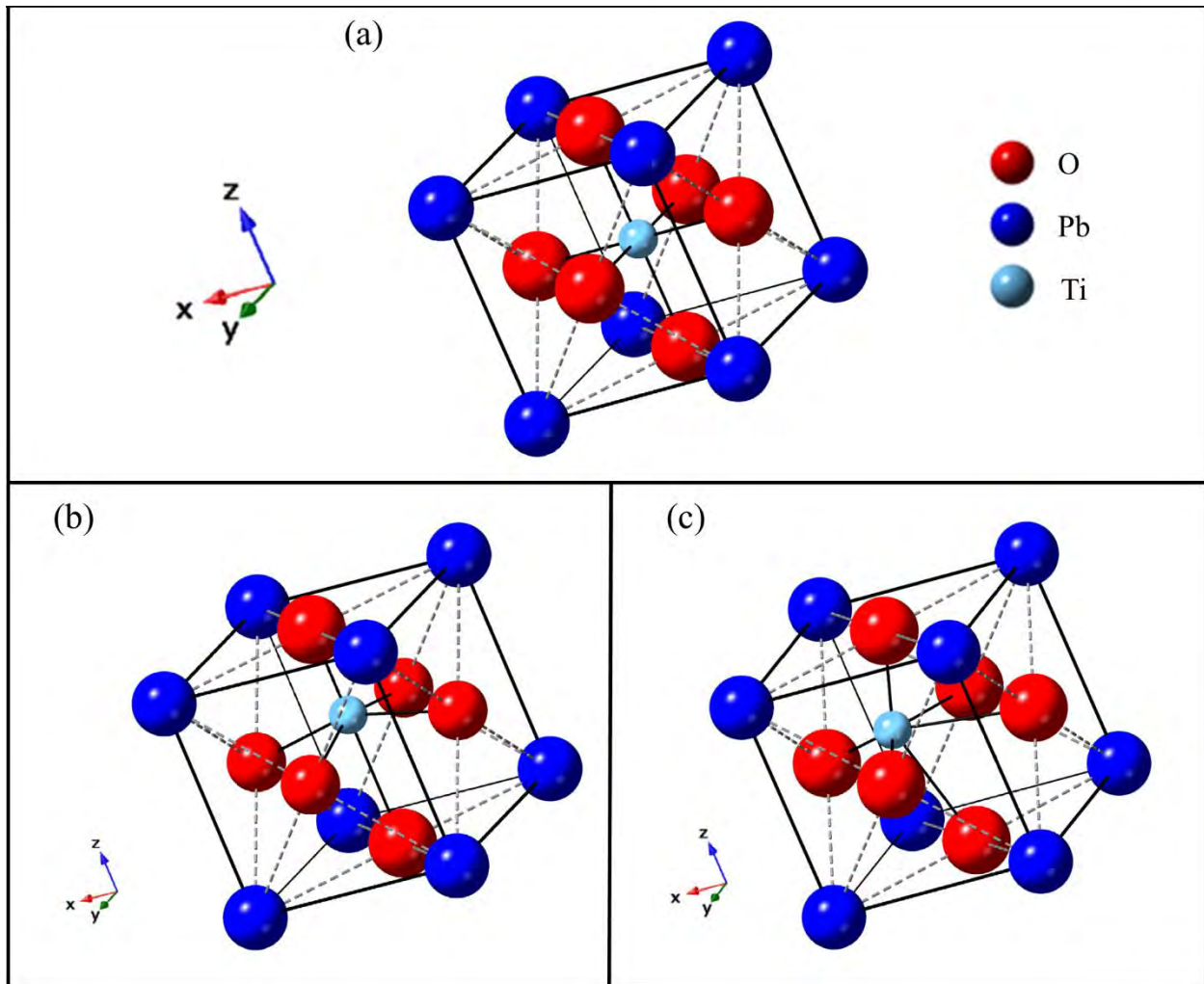
Figure 2-5. Crystal structure schematics of the cubic perovskites phase (a) Where the A site atoms site on the corners (in this case dark bue atom), the B site sites in the center of the unit cell (light blue) and the X site on the center of the faces (red). (b) shows the derivative ferroelectric tetragonal phase where the B ion moves towards one of the X site atoms, elongating the cell in this polar direction. (c) shows the rhombohedral phase derivative where the center Ti atom moves along the body diagonal towards three of the X atoms.

There are several well-known perovskites-based ferroelectrics, including $BaTiO_3$, $Pb(Zr,Ti)O_3$, $BiFeO_3$, and $(K,Na)NbO_3$ [33]. $Pb(Zr,Ti)O_3$ is used in many commercial applications because of its high piezoelectric coefficients that are retained over a broad temperature range [1,2,14,59]. The phase diagram of $Pb(Zr, Ti)O_3$ is shown in **Figure 2-6.** The end member $PbZrO_3$ is an orthorhombic antiferroelectric. The other end member, $PbTiO_3$, is a tetragonal ferroelectric. The PZT phase diagram is characterized by a morphotropic phase boundary between a ferroelectric

tetragonal phase and a ferroelectric rhombohedral phase. The rhombohedral phase is broken into a high temperature rhombohedral phase with untilted oxygen octahedra (R3m) and a low temperature phase that has tilted oxygen octahedra (R3c). At higher temperatures, the system is in the paraelectric phase cubic phase, and T_c depends on the composition.
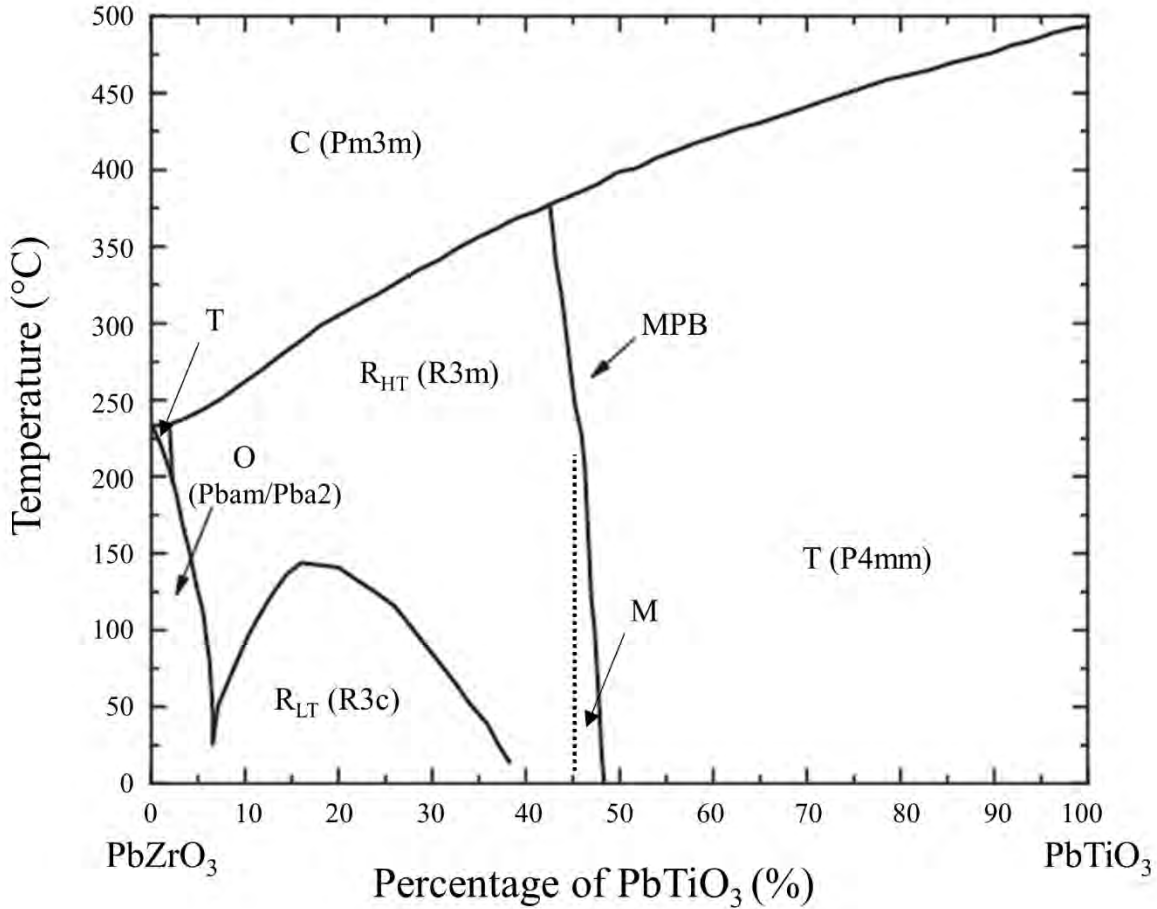
Figure 2-6. Phase diagram of $PbZrO_3$-$PbTiO_3$. C denotes the paraelectric cubic phase, O denotes Orthorhombic, R denotes rhombohedral, T denote tetragonal, M denotes monoclinic, and MPB is for the morphotropic phase boundary. Figure is adopted from: [33,60–62]

The morphotropic phase boundary (MPB) composition of PZT is used in a variety of applications because of its high piezoelectric response. At the MPB there are a total of 14 possible polarization directions due to the rhombohedral (8 along the pseudo cubic <111>) and tetragonal

(6 along the pseudo cubic <001>) polar directions. There may be additional polarization directions with the reported presence of a monoclinic phase at this composition as well [61–63]. It has been reported that the MPB composition allows for easier poling, and that furthermore the polarizabilities peak at this composition [33,64]. Because of its wide commercial interest, the MPB composition is investigated in this study.

While the phase diagram shows the importance of the composition on the PZT system, there are additional factors that can enhance the observed properties of PZT. The grain size and domain size can be optimized for larger responses [65], as was shown in $BaTiO_3$ [66]. Additionally, various dopants can alter the defect chemistry. Some donor defects such as Nb^{5+} and Ta^{5+} on the B site can create V_{Pb}'' [33]. These dopants act to improve domain wall motion and create a softer ferroelectric. In contrast, acceptor dopants such as Mg^{2+} and Fe^{3+} on the B site will create $V_o^{\cdot\cdot}$ and may create a harder ferroelectric as a result [33]. In this work, the composition and dopant used is $Pb_{0.99}(Zr_{0.52}Ti_{0.48})_{0.98}Nb_{0.02}O_3$.

2.5.1 PZT thin films

In this work, PZT films are used; these films are different from their bulk counterparts in a number of ways [67]. First, PZT films are grown on substrates, which causes them to be under significant amounts of residual stress [18,67–69] and are also clamped to the substrate. Clamping limits the domain wall motion [43], in response to an external force. As a result, the measured properties are typically suppressed when compared to bulk ceramics or released films [70–72]. Consequently, they are harder to pole. Additionally, PZT films typically have finer grain sizes and domain sizes, which can reduce the dielectric constant, and polarization and increase the coercive field [65,71]. Finer grains can have reduction in both extrinsic and intrinsic contributions to the properties [65]. Additionally, scaling affects as a function of film's thickness have been reported

for the dielectric, piezoelectric and ferroelectric properties of PZT thin films[71]. All of these structural differences have been shown to contribute to suppression of properties for films [71]. To overcome some of the reduced properties, films are typically oriented through epitaxial growth or the use of a seed layer in the substrate stack. In this thesis, the influence of residual and applied stresses on the observed mechanical and electrical properties of PZT thin films is of particular interest.

Chapter 3. Effect of Stresses on the Dielectric and Piezoelectric Properties of Pb(Zr$_{0.52}$Ti$_{0.48}$)O$_3$ Thin Films

This chapter discusses the influences of stresses on the dielectric and piezoelectric properties of PZT thin films. The total stresses in the film include residual, applied, and electrically induced stresses. To understand the influence of residual stresses, the permittivity and P-E loops of PZT films on Si and Ni foil were measured with varying uniaxial applied stresses. In addition, the piezoelectric and dielectric properties were also measured as a function of applied uniaxial strain. PZT on Ni foil was bent around a mandrel of a known radius to apply uniaxial strains. Compressive strains of up to -0.3% and tensile strains up to 0.47% were applied. Beyond -0.3% compressive strain, delamination was observed, and above 0.5% tensile strain, cracking was observed. PZT on Si was strained from 0.06% compressive strain to 0.06% tensile strain using the beam bending method, since the Si substrate is brittle. The changes in properties as a function of the total stress suggest differences in intrinsic and extrinsic contributions between the films on Ni and Si substrates including differences in domain structure, local stresses, and mechanical limits, which will be explored in later chapters.

3.1 Introduction

The stress state can influence both the dielectric and piezoelectric response of ferroelectric films [19,73,74]. Residual stresses influence the domain structure; in clamped films the remanent and saturation polarizations depend strongly on the residual stresses as a consequence of limitations on ferroelastic domain switching [15,18,19,68,73–77]. It is notable that applied stresses can also strongly affect the dielectric and piezoelectric properties of piezoelectric ceramics

[31,59,72,78–80]. For both hard and soft PZT ceramics, applied stresses either parallel or perpendicular to the polarization direction dramatically change the dielectric constants due to ferroelastic domain reorientation [81–85]. Brown showed that PZT ceramics under an uniaxial pressure of 250-300 MPa can have up to 50% reduction in the dielectric constants [81,82]. However, these stress-induced changes tend to be smaller in magnitude for thin films than bulk ceramics exposed to the same applied stress levels [31,59,72,78,79,85,86]. This was shown in studies by Shepard *et al*, where PZT films on Si have a 3-5% change in dielectric constant with similar applied stresses [85,86].

There have been many studies on the effect of either residual stress [15,18,75,77], or applied stresses [31,72,87] on PZT films. However, the role of a combination of residual and applied stresses on dielectric and piezoelectric properties has not been reported over wide stress ranges. Therefore, this study aims to quantify the effects of the total stress state on the piezoelectric, ferroelectric, and dielectric response of PZT thin films over wide stress ranges.

3.1.1 Types of Stresses

Thin films experience stresses from various sources including residual stress (σ_r) associated with the processing, applied stress induced by bending (σ_a), and electrically induced stress (σ_e) due to piezoelectric or electrostrictive responses. The total stress (σ_{Tot}) experienced by the films is the summation of these (**Equation 3-1**).

$$\sigma_{Tot} = \sigma_r + \sigma_e + \sigma_a \tag{3-1}$$

3.1.1.1 Residual Stress

In this section, the residual stress (σ_r) is distinguished from the stress from thermal expansion coefficient mismatch (σ_t) and the calculated residual stress from Stoney's equation (σ_f). σ_r in the film depends on several factors including the thickness and thermal expansion coefficients

(α_{CTE}) of various layers in the multilayer stack as well as the growth method. Coherent epitaxial films will experience stress due to the lattice strain; this contribution to the total stress is lost when the film nucleates enough dislocations to relax the epitaxial stress. In addition, if a film is grown through most physical vapor deposition (PVD) processes, such as pulsed laser deposition (PLD) and sputtering, there will be additional bombardment stresses [88–90]. For oriented thick films grown through chemical solution deposition (CSD), bombardment and epitaxial stresses are not present.

In CSD of PZT films $\gtrsim 100$ nm thick, the residual stress is due primarily to the thermal expansion coefficient mismatch between the film and the substrate [18,67,68,75,91,92]. The thermal expansion coefficient mismatch stress σ_t of the film and the substrate [18,68,75] is described in **Equation 3-2**.

$$\sigma_t = \frac{\int_{T_o}^{T_{max}}(\alpha_{CTE,f}-\alpha_{CTE,s})dT}{\left\{\frac{1-v_f}{Y_f}+\left(\frac{1-v_s}{Y_s}\right)\left(4\frac{t_f}{t_s}\right)\right\}} \tag{3-2}$$

where v is the Poisson's ratio of the film (*f*) or substrate (*s*), Y is the Young's modulus (90 GPa for {001} PZT) [93], T_{max} is the crystallization temperature, and T_o is the operating temperature. While σ_t is the predominant cause for stress in CSD films, below the Curie temperature (T_c) the nucleation of ferroelectric domains with specific orientations reduces the stress arising from the α_{CTE} mismatch [18], and σ_t will then overestimate the residual stress. Additionally, in CSD, the removal of solvents and densification during pyrolysis strongly influences the residual porosity. This porosity may reduce the film's elastic moduli, thereby modifying the residual stress [78,94]. The CSD film's residual stress is then a function of the domain structure and porosity.

If the substrate is rigid and the film's thickness is significantly smaller than the substrate [95], **Equation 3-2** can be simplified to the form shown in **Equation 3-3**.

$$\sigma_t = \frac{Y_f}{\nu_f - 1} \int_{T_o}^{T_{max}} \left(\alpha_{CTE,film} - \alpha_{CTE,substrate} \right) dT \qquad (3\text{-}3)$$

The film's global residual stress can be estimated by measuring the wafer curvature method for rigid substrates. Stoney's equation for a <001> Si wafer [67,69,96–98] is given in **Equation 3-4** [96,99].

$$\sigma_f = \frac{h^2}{6 t_f (S_{11}^{Si} + S_{12}^{Si}) R} \qquad (3\text{-}4)$$

where σ_f is the film stress, t_f is the film thickness, h is the substrate thickness, $S_{11}^{Si} + S_{12}^{Si}$ are components of the elastic compliance tensor of the Si, and R is the radius of curvature [96]. Stoney's equation assumes biaxial stress conditions, a uniform stress distribution, and that the film thickness is a few orders of magnitude thinner than the substrate [96]. As a result, Stoney's formula is not valid for PZT on many metallic foils owing to the foil's lack of rigidity and its thickness. Moreover, σ_t does not consider alleviation of stress either from the domain structure or curvature of the film/substrate system. Thus, the average σ_t should be treated as an estimate of the σ_r. In this work, a polycrystalline average for the α_{CTE} was used to approximate the residual stress, and the values for σ_t were compared to σ_r for PZT on Si.

3.1.1.2 *Applied Stress*

During application, films may experience additional uniaxial or biaxial mechanical stresses due to mechanical or electrical loads; these in turn may induce ferroelastic domain switching in PZT films [72,87]. In applications such as many kinetic energy harvesters, uniaxial stresses are applied along the length of the cantilever [16,17]; in some transducers, biaxial stresses are applied to diaphragms.

The electrically-induced stresses (σ_e), governed by the effective transverse piezoelectric coefficient ($e_{31,f}$) and the applied electric field (E) [31], are shown in **Equation 3-5**.

$$\sigma_e = -e_{31,f} E \tag{3-5}$$

It is important to note that $e_{31,f}$ will itself be a function of both the electric field and the stress state of the film [44,100]. Thus, **Equation 3-5** is not expected to be truly linear. An additional electrostrictive (*M*) component cannot always be neglected, such that the expanded form would be [8]:

$$\sigma_e = -e_{31,f} E + \frac{1}{2}McE^2 \tag{3-6}$$

where c is the material's stiffness. When fields are low, (below 80 kV/cm) the bulk electrostrictive term [101] will be on the order of 0.1 to 5 MPa, where 5 MPa is about an order of magnitude less than the piezoelectric response. Thus, in this thesis for the small fields applied, this second term is ignored.

In this study, uniaxial strains were applied by the radius of curvature (ROC) method in which a film is wrapped around a mandrel to induce a predetermined applied strain ($\varepsilon = \delta/R$), based on the distance of the film to the neutral axis (δ) (see **Figure 3-1a**). Using this method on flexible Ni foil samples allowed for a large strain range (0.5% to -0.32%) beyond which failure of the PZT/Ni stack would occur. In addition to the ROC method, uniaxial strains were also applied by bending a cantilever beam; this was used for lower magnitudes of strains for films grown on brittle substrates such as Si (see **Figure 3-1b**). To biaxially load samples, the ball on three ball (B3B) method was used (see **Section 5.2.2**).
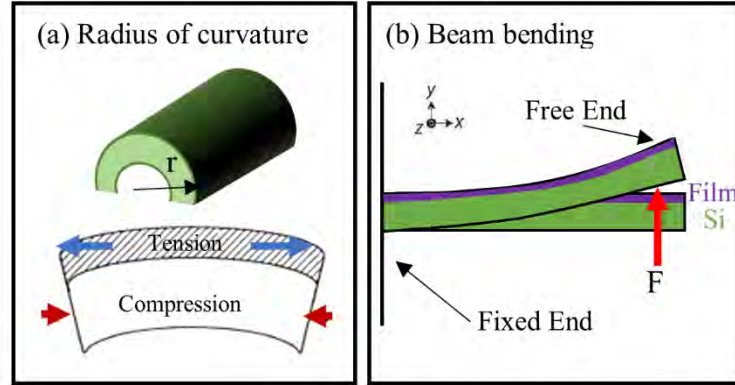
Figure 3-1. Method for applying uniaxial strains on PZT films. The radius of curvature method (a) was used for higher strains and more flexible substrates, and the beam bending method (b) was used for lower strains for the Si case.

3.1.2 Overview

{001} oriented PZT (Pb$_{0.99}\square_{0.01}$(Zr$_{0.52}$Ti$_{0.48}$)$_{0.98}$Nb$_{0.02}$O$_3$) films on Ni and Si substrates were fabricated through CSD to investigate the influence of substrates with different thermal and mechanical properties on the properties of PZT films. Electrical characterization methods were used to explore changes in the properties and domain structure as a function of σ_{Tot}. The ε_r and piezoelectric coefficient, ($e_{31,f}$) were measured as a function of the total stress to understand the relationship between stress, domain state, and stress limits in piezoelectric thin films [18,31,59,64,102].

3.2 *Experimental Procedure*

3.2.1 PZT Chemical Solution Deposition

PZT films were grown by chemical solution deposition (CSD) on either 50 μm thick Ni foil or 500 μm thick Si <001> wafers. Ni foil of 99.98% purity was used from Sigma Aldrich [15]. The Ni foils were first polished using Al$_2$O$_3$ powders from 5 μm down to 30 nm particle size [15]. Then the NiO was removed by annealing in a reducing environment (P$_{o_2}$ ~10^{-17} atm) at 900°C for 1 hour. Following this, a 30 nm HfO$_2$ buffer layer was deposited by Atomic Layer Deposition (ALD) to reduce nickel oxidation during subsequent processing steps [15,103].

To achieve the desired {001} orientation, a LaNiO$_3$ (LNO) bottom electrode was deposited by CSD using an acetic acid-based solution on both the prepared Ni foil substrates and Si wafers with a 1 μm thermal oxide (NOVA Electronic materials). To make 120 mL of 0.2 M LNO solution, 10.397 g of lanthanum nitrate hexahydrate and 5.973 g of nickel acetate trihydrate were added to 90 mL of acetic acid and refluxed at 80°C for an hour. Then, 23 mL of acetic acid was added and refluxed for an additional 3 hrs. The solution was cooled to room temperature and 6 mL of deionized (DI) water was added and stirred for 30 minutes. The solution was bottled and allowed to chelate overnight prior to use [15,104]. Then the LNO solution was spun at 3000 RPM, pyrolyzed sequentially at 150°C and 370°C for 2 minutes each, and crystallized at 700°C for one minute in a rapid thermal annealing furnace. This process was repeated five times to achieve a bottom electrode of 130 nm thickness.

PZT with 2% Nb was deposited on the bottom electrode using CSD with a 0.4 Molar 2-methoxyethanol based solution with 10% Pb excess [105]. To make 60 mL of this solution, 9.923 g of lead acetate trihydrate was added to 60 mL of 2-methoxyethanol (2MOE) and refluxed at 120°C for a minimum of 30 minutes under Ar flow. This solution was then distilled at 120°C to remove bound water. At the same time in a glove box, the zirconium, titanium, niobium precursors were prepared. 5.72 g of zirconium (IV) propoxide, 0.153 g of niobium (V) ethoxide, and 3.31 g of titanium (IV) isopropoxide were added to 30 mL of 2MOE and refluxed for a half hour. Once the Pb precursor was distilled and the Ti/Zr/Nb solution was well mixed, the two solutions were combined with an additional 90 mL of 2MOE and refluxed for a minimum of two hours at 120°C under Ar gas. Then the solution was distilled to 46.5 mL at 120°C to remove any remaining water. The solution was cooled to room temperature and 13.5 mL of acetylacetone was added as a

stabilizer. The solution was refluxed for a minimum of 20 minutes, bottled, and left in a dry box for 12 hours to chelate prior to use.

From this solution, films were spun at 1500 RPM, pyrolyzed at 225°C and 400°C for two minutes each, and then crystallized at 700°C for one minute in a Pb-rich rapid thermal annealing furnace. This process was repeated seven times to achieve a thickness of ~0.6 μm; additional details on the deposition are provided elsewhere [15]. A PbO capping layer was added after the 7th layer to remove the pyrochlore secondary phase on the surface of the film, which formed due to Pb volatilization during crystallization [105]. For films grown to larger thicknesses, approximately every 5th - 7th layer, a PbO layer was utilized due to the continued volatization of Pb during each crystallization step. When the PbO was added depended on the Pb furnace condition and the presence of pyrochlore. To assess when the PbO layer was needed, the film surface was checked intermittently using a field emission scanning electron microscope (FeSEM) (see **Figure 3-2**); pyrochlore was manifested as very fine grained material, with higher concentrations at the perovskite grain boundaries. If pyrochlore coated too much of the film surface, newly deposited solution could not nucleate from the pre-existing perovskite grains, and crystallographic orientation was progressively degraded. The PbO solution (0.08 M from lead acetate trihydrate dissolved and distilled into 2MOE in a similar manner as the PZT solution) was spun at 3000 RPM, pyrolyzed at 110°C for one minute, 225°C for two minutes, 410°C for two minutes, and then crystalized at 700°C for one minute with a ramp rate of ~10°/s.
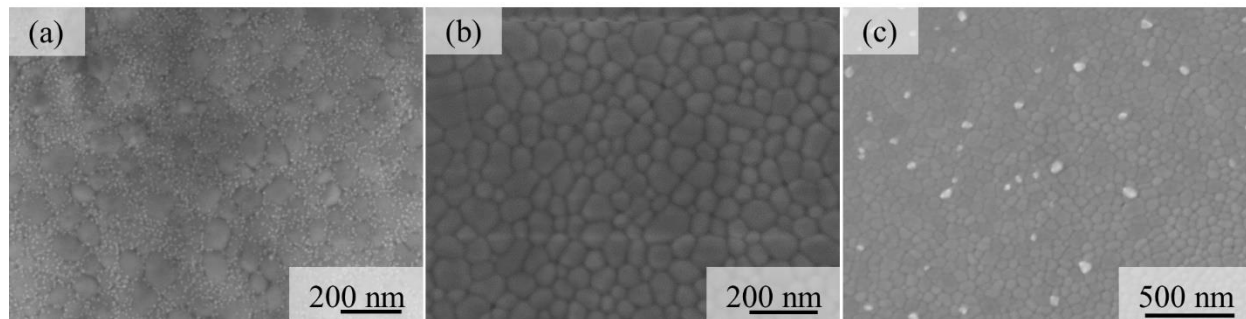
Figure 3-2. Various microstructures that may form depending on the lead environment of the Pb furnace and PbO added to the film. (a) lead deficient film with a fine-grained surface pyrochlore phase which nucleated at the grain boundaries of PZT. This film requires a PbO layer. (b) pure PZT phase, after deposition of a PbO capping layer (c) PZT phase with a Pb-rich secondary phase on top that can be removed in acetic acid.

3.2.2   Film Structural Characterization

The orientation and phase purity of the films were characterized by a combination of X-Ray Diffraction (XRD) using a PANalytical Empyrean diffractometer with a Cu K_α X-Ray source and by Leo 1530 FeSEM. For XRD, first the peaks of the underlying layers were identified, as shown in **Figure 3-3.** These peaks were visible due to strong orientation, the existence of low intensity wavelengths including Cu K Beta, and so-called ghost peaks. Some peaks from nickel oxidation and from the HfO_2 buffer layer were also detected. For XRD, the following powder diffraction files (pdf) were used: Si (00-027-1402) [106], $LaNiO_3$ (LNO) (00-033-0710) [107], Ni (00-004-0850) [108], NiO (00-004-0835) [109], HfO_2 (00-053-0550)[110], PZT (52/48) (00-033-0784) [111]. The numbers in parentheses correspond to the pdf file for each of the given material from the ICDD inorganics database.
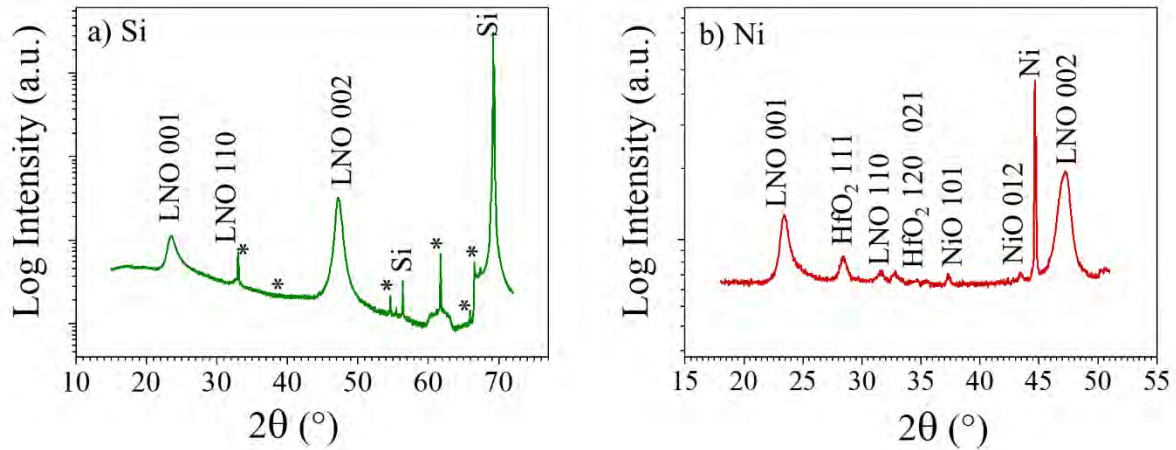
Figure 3-3. XRD patterns of the substrate and subsequent layers prior to the addition of the PZT layer. Peaks for the Si and LNO for the Si substrate (a) and peaks for the Ni, HfO_2 buffer and LNO for the flexible Ni substrate (b) are labeled.

For the FeSEM, low voltages and currents were used (3.0-5.0 kV and 100 µA) since PZT is a good insulator. For these fine grain microstructures, short working distances (2.4-3.5 mm) are recommended. From these images, lateral grain sizes were determined using the average intercept method with a minimum of six lines in varying directions. Unless otherwise noted, all PZT films have a preferred {100} orientation.

3.2.3   Film Electrical Characterization

To electrically characterize these films, DC magnetron sputtered Pt top electrodes were patterned by photolithography in diameters of 1 mm, 0.6 mm, and 0.4 mm. First, LOR 5A was spun at 4000 RPM for 45 s and then baked at 180-190°C for two minutes. Then, SPR 3012 was spun on at 4000 RPM for 45 s and baked at 95°C for two minutes. The photoresist was then exposed (6.0 MJ for 7 s) and then developed in CD-26 for 70 s. The quality and sizes of the features were checked with the optical microscope. A descum plasma etch was performed using O_2 and He gas in the M4L oxygen plasma chamber with 200 W power for two minutes prior to sputtering. Pt was sputtered using the Kurt Lesker CMS-18 sputter tool with a power of 200 W. The Pt was

31

deposited for 417 s to achieve a thickness of 100 nm. For lift off, the sample was submerged in acetone for a minimum of 30 minutes. This allowed the photoresist to dissolve and the Pt to lift off the surface. Wafers were not scrubbed to prevent damage to the features. Samples were then rinsed with DI water. To remove any remaining photoresist, samples were submerged in CD-26 and then rinsed in DI water.

The samples were then cut into cantilever beams with an aspect ratio of 1:4 or into a desired shape. Access to the bottom electrode was made through either a wet etch or mechanical scratch. The wet etch was performed after first painting most of the film with an 1813 photoresist protective layer, and then baking at 120°C until hardened (typically 5 minutes). Then a drop of BOE (10:1 DI water to Hydrofluoric acid concentration) was placed on the exposed region, followed by a drop of HCl. These steps were repeated until the bottom Pt electrode was reached. The scratch method is performed by abrading through the PZT with a razor blade to expose the bottom electrode and then adding silver paste to the scratched region. The silver paste was dried at room temperature for a minimum of two hours, until the paint dried. The scratch method was the preferred method as HCl and HF can easily etch the lanthanum nickelate bottom electrode and Ni.

The ε_r and the polarization-electric field (P-E) hysteresis loops were measured using a Hewlett Packard 4284A precision LCR meter and a Radiant Multiferroic tester, respectively, where the applied electric field was out-of-plane, perpendicular to the in-plane applied and residual stresses. The P-E loops were measured using a single triangular wave form with no pre-pulse and a frequency of 100 Hz.

3.2.4 Methods for Applying Uniaxial Strains

Two different methods were used to apply uniaxial stresses for the two different substrates due to their different mechanical properties and strain limitations. For the samples on Ni, the radius of curvature (ROC) method was used, where the foil was bent around a mandrel of a known radius and the distance of the film to the neutral axis was calculated to determine the applied strain and stress (**Figure 3-4** and **Figure 3-1**). The calculated applied strain was experimentally confirmed through strain gauges within 0.02% strain. To apply a compressive stress, the Ni foil was curved around the inner radius of a hollow mandrel with the PZT film facing inward, and for tensile stress the Ni foil was curved around the outer radius with the PZT film facing outward. Compressive strains of up to -0.3% were applied, as were tensile strains up to 0.47%. Above -0.3% compressive strain, delamination between layers was observed and above 0.5% tensile strain, cracking was observed in the PZT. For the samples on Si substrates, stress was applied by a beam bending method (**Figure 3-1**) where a fixed - free beam of the sample had an applied force at the end of the cantilever. Since the Si substrate is brittle, the range used in this study was from 0.06% compressive strain to 0.06% tensile strain. This strain range is roughly an order of magnitude smaller compared with films on Ni foils.
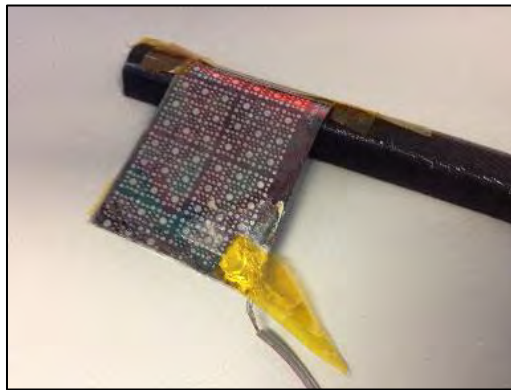
Figure 3-4 Photo taken of the Ni foil sample being wrapped around a mandrel with a radius of 4.8 mm.

3.2.5 Piezoelectric Coefficient ($e_{31,f}$) Measurement

The effective transverse piezoelectric coefficient ($e_{31,f}$) was measured by poling individual electrodes on the film at 250 kV/cm, 150°C for 15 minutes and waiting a minimum of 12 hours to allow the domain state to stabilize. The $e_{31,f}$ was measured by clamping the film at one end and actuating it with a sinusoidal strain at the opposite end, using a piezoelectric actuator stack [102]. For the $e_{31,f}$ measurement, the static and dynamic strain were measured using an Omega strain gauge (KFH-1.5-120-D16-11L1M2S) with a gauge factor of 1.95 ± 1.5%. This was adhered to the surface of the cantilever using *Loctite*® superglue near the electrodes being tested. The strain and charge signal from the electrodes were measured during dynamic actuation of the cantilever using a quarter Wheatstone bridge and a lock-in amplifier. Tungsten probes were used to contact the top and bottom electrodes and the charge signal was amplified using a charge to voltage amplifier of 100 pA to 1 mV and detected using a second lock-in amplifier. Both charge and strain signals were referenced against the sinusoidal wave signal driving the piezoelectric stack actuator, in order to determine the phase angle of each signal.

To measure the $e_{31,f}$ as a function of stress, the samples were strained using the beam bending method. The stack actuator was raised and lowered using a micrometer to change the static strain applied to the cantilevers via bending. Raising the height of the actuator puts the PZT film into more compression. Samples were flipped upside down to put the film in tension when raising the actuator. On flexible Ni foils, part of the Ni foil cantilever was sandwiched between two rigid glass slides. This cantilever hinge design effectively concentrates the sinusoidal bending strain induced by the piezoelectric actuator on the tested electrodes on the PZT/Ni foil device, as shown in **Figure 3-5.**
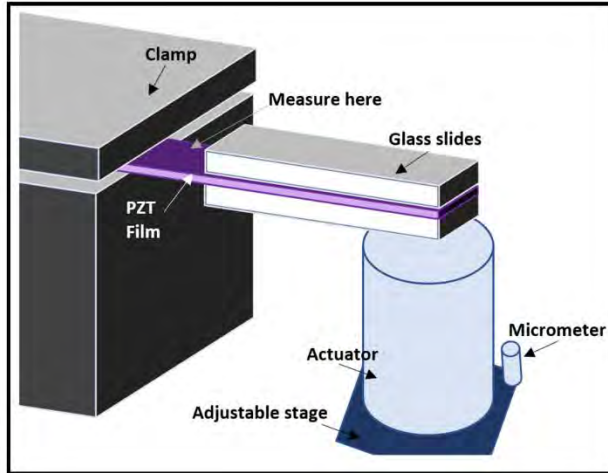
Figure 3-5. Schematic set up for measuring $e_{31,f}$ on Ni foil; the glass slides are adhered to the cantilever to allow the sinusoidal strain to reach the measured area.

3.3   Results

The XRD pattern and FeSEM images for the PZT films on Si (**Figure 3-6a, c, e**) and Ni foils (**Figure 3-6 b, d, f**) are shown in **Figure 3-6.** The grains were columnar and the average lateral grain size for these films was 81 ± 13 and 65 ± 4 nm for the sample on Si and Ni foil, respectively.
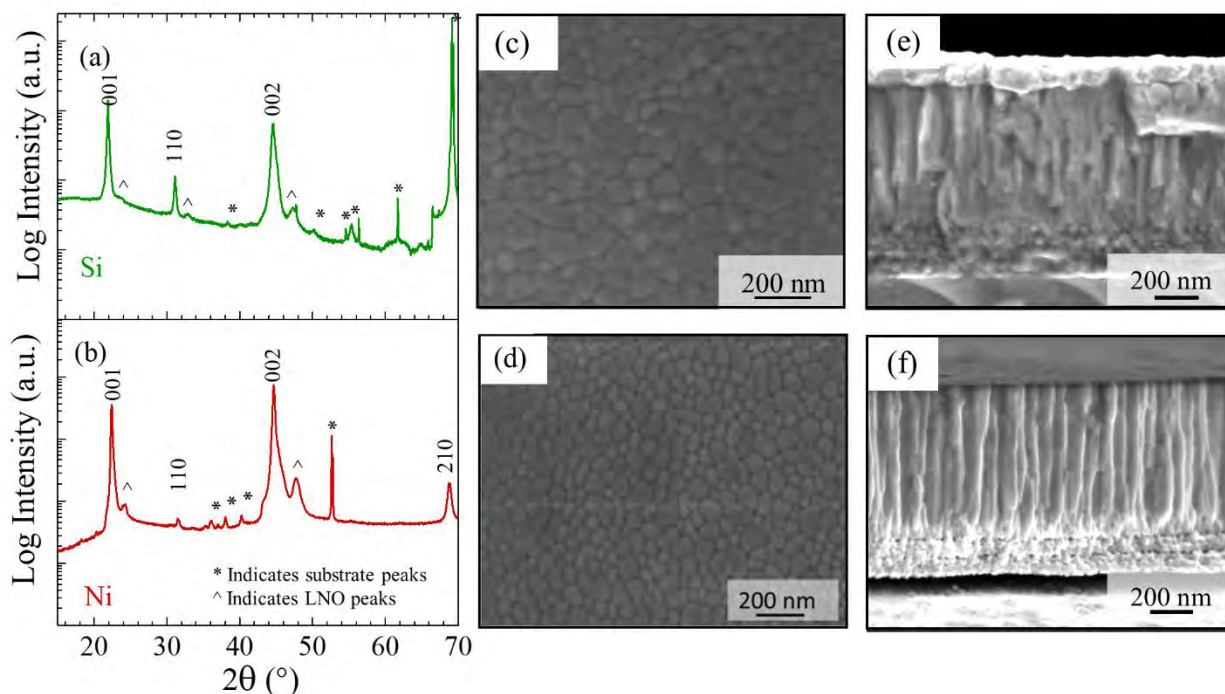
Figure 3-6 XRD patterns for 0.6 μm thick PZT films on Si (a) and Ni (b), and top surface FeSEM images of the grain structures on Si (c) and Ni (d), and FeSEM cross section for the 500 μm thick Si wafer (e) and 50 μm thick Ni foil (f). The Lotgering factors were 98% for the sample on the Ni foil and 92% for the sample on Si.

The PZT residual stress was estimated from σ_t calculated using **Equations 3-2 & 3-3**. The thermal expansion coefficients of Si and Ni have been reported as 2.3-4.5 x 10^{-6}/K [112], and 13.3-17.1 x 10^{-6}/K [113] (in the temperature range from 25-700°C), respectively. For PZT, the thermal expansion coefficient is dependent on temperature and ranges from 8 x 10^{-6}/K down to 0 /K in the paraelectric phase, and between 0 and 2 x 10^{-6}/K in the ferroelectric phase, with a discontinuity at T_c [18,114]. The T_c for these PZT samples was 336 ± 8°C for samples on Si and 325 ± 6°C for samples on Ni, as shown in Error! Reference source not found..
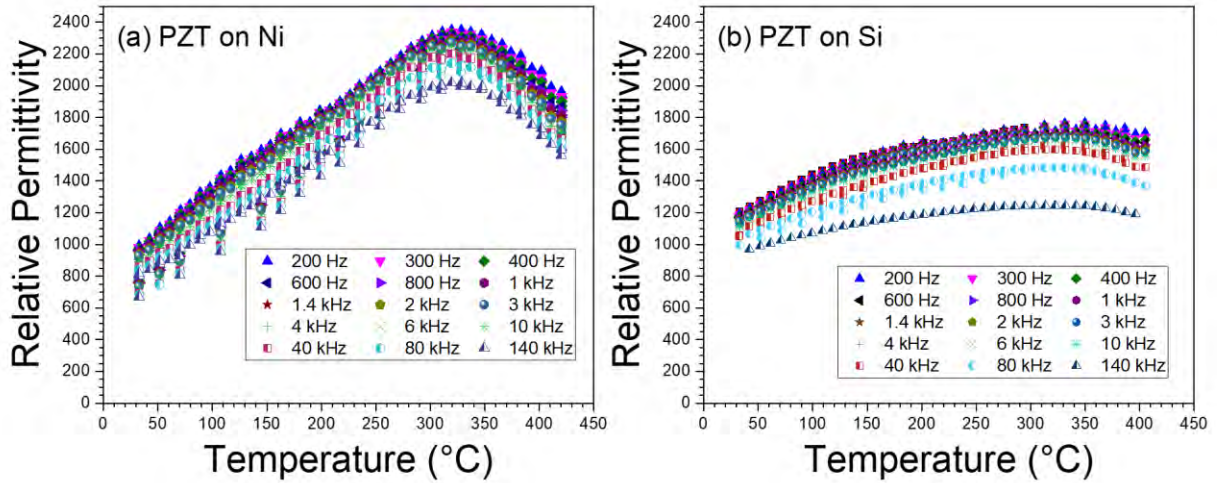
Figure 3-7. The relative permittivity vs temperature measured at various frequencies (from 200 Hz up to 140 kHz) for PZT on Ni (a) and PZT on Si (b). The temperature when the derivative equals zero was assigned to be T_c for the two films. T_c for PZT on Ni and Si were around 320°C for both films.

Using **Equation 3-2**, the PZT films on Ni foil were under a compressive stress of approximately 530 ± 30 MPa, and PZT films on Si were under a tensile stress of approximately 130 ± 30 MPa. **Equation 3-3** overestimates the compressive σ_t of the PZT on Ni since it does not consider bowing of the substrate or the resulting domain structure. However, for PZT on Si, the tensile σ_t is in agreement with σ_f, which was confirmed through wafer curvature measurements (150 ± 40 MPa). Moreover, the calculated values are consistent with what has been reported in the literature [18,19,67,69,86]. Since σ_f and σ_t do not consider the formation of domains, which will alleviate stress, they will somewhat overestimate the magnitude of σ_r.

Recognizing the difference in the residual stress, **Figure 3-8** compares the P-E loops of PZT on Ni and Si at 100 Hz. At the same electrical field of 900 kV/cm, P_r was 21 ± 0.2 µC/cm^2 on Si and 39.5 ± 2.3 µC/cm^2 on Ni. This difference is consistent with prior reports for films under tensile stress having more in-plane polarization and lower remanent polarizations [15,18]. It is

notable that the PZT film on Si could be driven to a higher electric field (1400 kV/cm) for which the P_r improved to 26.0 ± 0.2 $\mu C/cm^2$. This increase was not observed for the Ni foil samples. At lower electrical fields (400 kV/cm) the P_r drops to 13.2 ± 0.12 $\mu C/cm^2$ and 32 ± 1.6 $\mu C/cm^2$ for PZT films on Si and Ni, respectively. At a driving signal of $V_{ac}= 30$ mV and 1 kHz, the ε_r was 1040 ± 20 and 600 ± 80 for the virgin films on Si and Ni foil, respectively with loss tangents of less than 5.0% for all of the films. These differences in ε_r suggests differences in the percentage of in-plane polarization, where the PZT on Si would have more in-plane polarization, and a higher ε_r.
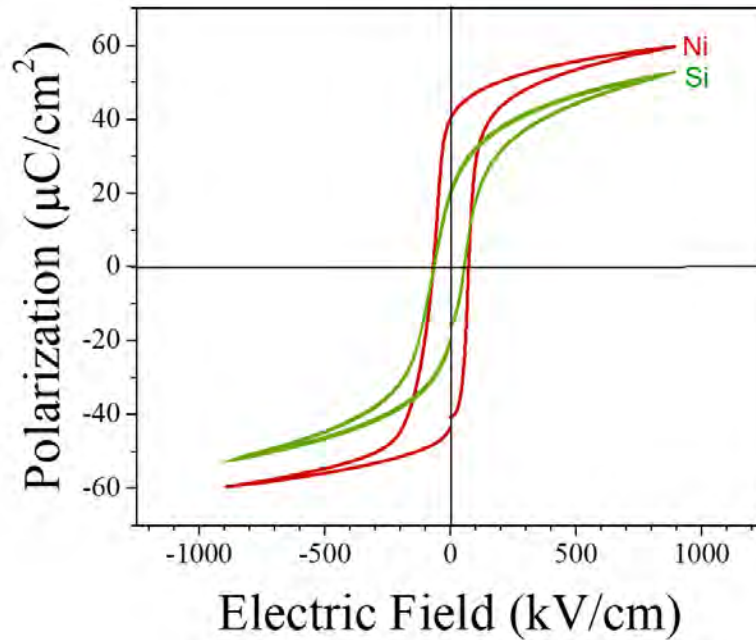
Figure 3-8. P-E hysteresis loops for PZT on Ni (red), and PZT on Si (green). The P_r for films on Si was 21 ± 0.2 $\mu C/cm^2$, while films on Ni had P_r of 39.5 ± 2.3 $\mu C/cm^2$. This was due to the compressive thermal expansion stresses for PZT films on Ni, causing a larger percentage of "c" (out-of-plane) domain orientation [18].

Figure 3-9 shows the changes in the P-E loop and P_r for PZT films on Si and Ni foils at different applied strain levels. The P-E loops of films on both Si (**Figure 3-9 Ia**) and Ni foils (**Figure 3-9 IIa**) experienced a clockwise rotation under tension and a counterclockwise rotation

under compression, as has been reported previously [86]. For the films on Si, the P_r varied from

11.7 ± 0.16 $\mu C/cm^2$ at 0.06% strain to 14.1 ± 0.14 $\mu C/cm^2$ at -0.06% strain at 400 kV/cm. For the

films on Ni foils, P_r varied from 33 ± 1 $\mu C/cm^2$ at -0.2% strain to 27.1 ± 0.7 $\mu C/cm^2$ at 0.4% strain.

Upon removing the applied strains from each sample, the P_r partially recovered to the initial value

at zero applied strain. These same samples were cycled through the entire strain range again; little

hysteresis of the P_r was observed between the first and second strain cycles for films on Si (**Figure**

3-9 Ib). The hysteresis was more pronounced for PZT films on Ni substrates. However, it was still

<6% and a trend as a function of cycles was not distinguishable (**Figure 3-9 IIb**). The normalized

polarization changed approximately linearly as a function of applied strain for both films on Si

(**Figure 3-9 Ic)** and Ni foils (**Figure 3-9 IIc**). At 0.04% compressive strain the P_r increased by

roughly 5% for the PZT on Si, while on Ni a large compressive strain of 0.2% was required for

this magnitude of a change. This difference in the strain required for a 5% change in the P_r may

be due to differences in the domain structure and residual stress.
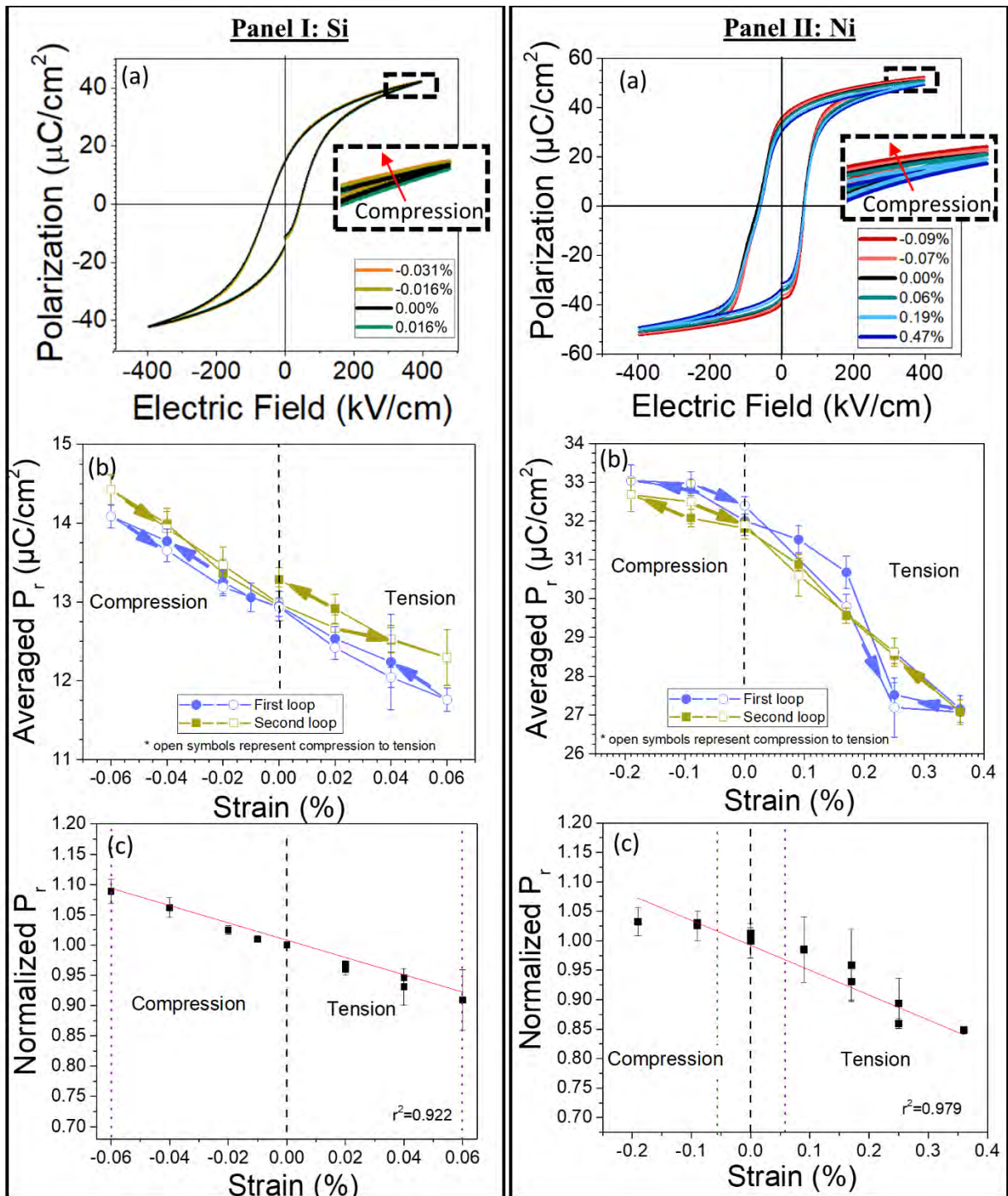
Figure 3-9 Polarization hysteresis loops for PZT films on Si (Panel Ia) and Ni (Panel IIa). Changes in P_r as a function of applied compressive and tensile strain on Si (Panel Ib) and Ni (Panel IIb) as well as the linear trend of the normalized change in P_r [e.g. $P_r(strain)/P_r$ (zero strain)] as a function of both applied compressive and tensile strain on Si (Panel Ic) and Ni (Panel IIc). The strain range for samples on Ni was -0.2% strain to 0.4% strain; for Si it was from -0.06% to 0.06%. The purple dotted lines (Panel Ic & Panel IIc) indicate the smaller strain range over which films on Si were tested. Negative strains represent in-plane compressive strains, and positive represent in-plane tensile strain.

To investigate how the applied strain alone influenced the domain state, dielectric Rayleigh measurements were made at 1 kHz as a function of applied strain (**Figure 3-10**). The PZT on Ni samples were strained from -0.2% to 0.5% strain, and at 1 kHz and 0 V DC bias, the AC field was increased up to 20 kV/cm, which is less than half the coercive field. For all AC fields, the ε_r increased under applied tensile strain and decreased under compressive applied strain. At an AC driving field of 5 kV/cm (30 mV), the ε_r for a PZT film on Ni was 620 ± 40 at 0.5% applied tensile strain and 460 ± 50 at 0.2% compressive strain (**Figure 3-10b**). The permittivity was normalized to the value at zero applied strain and increased approximately linearly with the applied strain (**Figure 3-10b**). The slope of the normalized ε_r change was opposite that of P_r. These changes are consistent with changes in the domain state under high stress levels. That is, a higher "c" domain population induced under compression should decrease the ε_r value, while a higher "a" domain population in films under tensile stress is expected to increase the ε_r [64,115].

The permittivity in the Rayleigh regime was fitted (with an R^2 of greater than 0.999) for all strains tested and is denoted by the dashed lines in **Figure 3-10a**. ε_{init} is determined from the zero-field intercept, and α_{Ray} from the slope of the line. Both ε_{init} and α_{Ray} increase with the applied tensile stress. The increase in ε_{init} may be due to an increase in reversible domain wall contributions, a change in the intrinsic response (i.e. the percentage of "a" increases with tension), or the combination of the two. Comparable trends in the ε_r as a function of applied strain were observed for films on Si, however, the small strain range meant that the changes in permittivity were not as pronounced. Clearer changes in properties with strain were seen for PZT on Si in higher field measurements (i.e. P-E loops). This is consistent with previous studies of changes in permittivity for PZT on Si substrates [86].
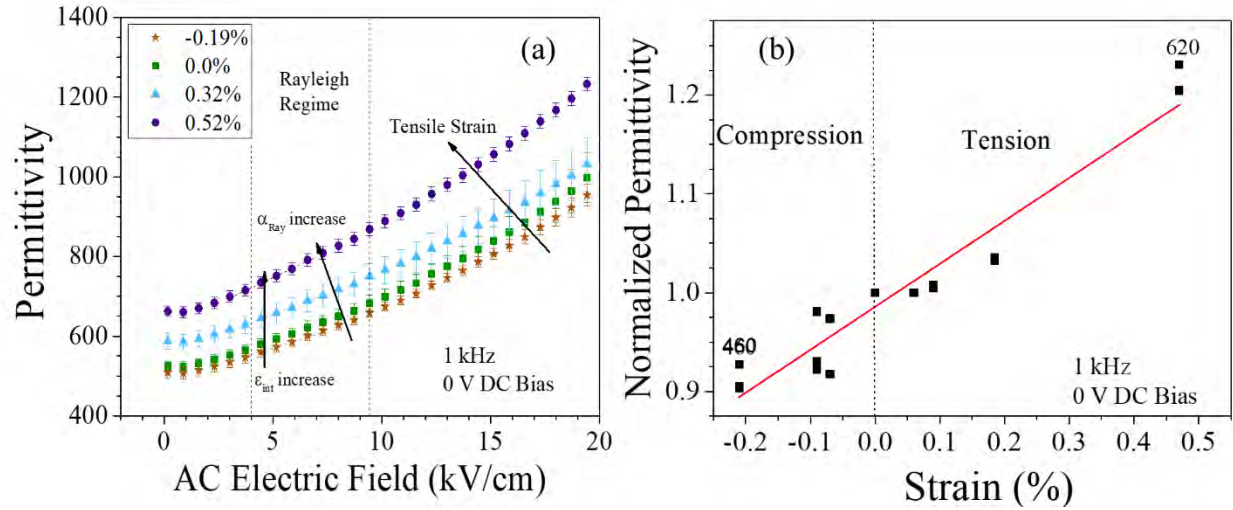
Figure 3-10 Permittivity as a function of strain and AC field for the PZT on Ni foil (a) and the normalized permittivity as function of strain at 5 kV/cm AC field (b). Both ε_{init} and α_{Ray} increased as a function of tensile strain. These measurements were at 0 V DC bias.

The linear increase in the low field permittivity (**Figure 3-10**) and linear decrease in the P_r (**Figure 3-9**) as a function of applied tensile strain suggest that tensile strain induces more in-plane domains, which have high permittivity and lower P_r. Thus, the mechanical state likely causes changes in the domain population of the PZT films. These effects of applied strain are also seen on the effective transverse piezoelectric coefficient ($e_{31,f}$). A lower P_r indicates that fewer domains are aligned parallel to the electric field direction after the field has been removed; the remanent piezoelectric response scales with P_r. Measurements at zero applied strain yielded an $e_{31,f}$ of -9.7 $\pm$ 0.45 C/m^2 for films on Ni foil and -7 ± 0.35 C/m^2 for the films on Si. The difference in these values at zero applied strain is related to the different residual stress states and domain populations of the films. **Figure 3-11** shows the changes of $e_{31,f}$ normalized to the zero applied strain value, as a function of applied compressive strain for films on Si. As the compressive stress increased, the magnitude of $e_{31,f}$ increased. The magnitude of this increase depends on whether the film was only

poled before or again after the applied static loading to the new strain level, allowing for alignment of more "c" domains.
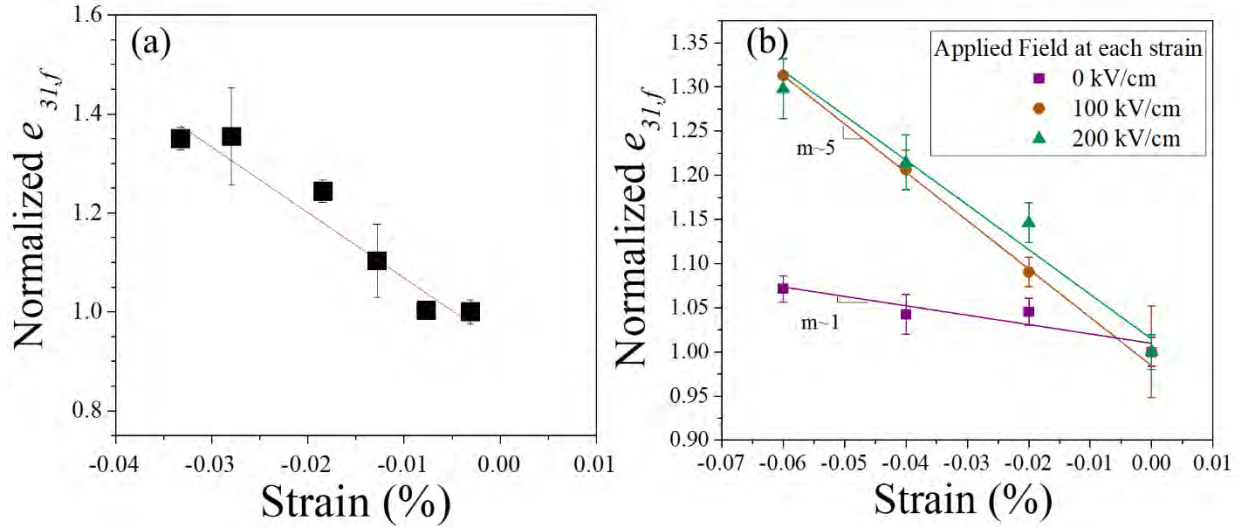
Figure 3-11 (a) Normalized $e_{31,f}$ as a function of applied strain for PZT on Si. The magnitude of the $e_{31,f}$ increases linearly under compression. (b) Normalized $e_{31,f}$ with various applied DC biases as a function of compressive strain. m indicates the slope of the linear fit of the normalized $e_{31,f}$ as a function of strain (%); the stain dependence was larger when samples were repolled while under strain.

3.4   Discussion

The difference in the P_r and permittivity between the two sets of samples corresponds with the residual thermal stresses in the films [15,18,91]. While the PZT composition is close to the morphotropic phase boundary and likely consists of both tetragonal and rhombohedral phases, only the tetragonal domain configurations are considered here, due to the larger difference in P_r and permittivity between in-plane and out-of-plane domains. Samples on Ni foil were found to have a larger volume fraction of domains with out-of-plane polarization, referred to as the tetragonal "c" domains, which have a lower permittivity and a higher P_r than in-plane domains or "a" domains. As a result, PZT films on Ni foil have a lower permittivity and higher P_r. The samples

on Si tend to have a lower P_r and higher permittivity because the tensile stress results in a smaller volume fraction of "c" domains [15,18,91,116].

As seen in **Figure 3-9** and **Figure 3-10**, an increase in the applied compressive stress also increases the P_r and decreases the permittivity, while applied tensile stress decreases the P_r and increases the permittivity. These changes suggest the possibility of ferroelastic domain reorientation, as shown in the schematic in **Figure 3-12**. Ideally, the majority of the non-180° domain walls could move and all domains could undergo ferroelastic switching as suggested by row 2 of **Figure 3-12**. However, the permittivity and P_r on the Ni foil under the highest applied tension did not overlap any of the values of films on Si. This suggests that many of these domains cannot reorient. It is possible that the local strains induced from one domain switching may prevent others from switching, as shown by row 3 of **Figure 3-12** [72]. Thus, the reorientation of domains induced by applied tensile stresses at room temperature is insufficient for the films on Ni foils to reach a similar domain state as the samples on Si before mechanical failure ensues. Also, the approximately linear change of both electrical properties as a function of applied strain on Ni foils indicates that domain reorientation as a function of applied strain may be approximately constant over the strain ranges tested. The linear trend may indicate a wide distribution in the energy potential required for ferroelastic switching. This has been indicated by previous studies [72], but is shown here to persist over much wider strain ranges and a larger total stress magnitude.
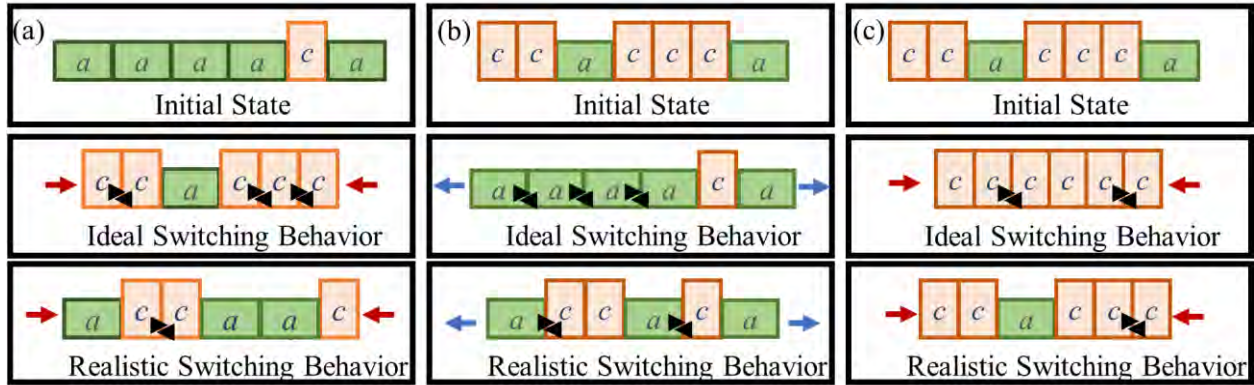
Figure 3-12. Schematic of the domain state for the films on Si substrates (a) and Ni foil (b, c). Also shown is how an applied compressive stress could affect the domain state on Si (a) and Ni (c), as well as how tensile stress might change the domain state for the samples on Ni (b) [72]. Red arrows facing in (→ ←) represent compression. Blue arrows facing outwards (← →) represent tension. Black triangles (▸◂) in between domains represent local stresses induced from non-180º domain switching.

In addition, the magnitude of the piezoelectric coefficient increased linearly with applied compressive stress. This also suggests some ferroelastic reorientation of domains [73]. However, the reorientation of ferroelastic domains by stress allows for two ferroelastically equivalent (180°) polarization direction possibilities. That is, when "a" domains switch to "c" domains under compression, it is likely that some of these domains will have antiparallel polarization directions (up and down), and thus their charge contributions with cancel out. Therefore, the net piezoelectric response may not be significantly enhanced. However, a DC electric field would help align the majority of these reoriented "c" domains with the field direction, causing them to contribute to the net piezoelectric response and thus produce a significant increase in the piezoelectric coefficient.

The linear trends in the permittivity, remanent polarization and piezoelectric coefficient are the result of the total stress state of the PZT films. Thus, the applied stresses were added to the residual stresses to provide an estimate of the total stress state for the films on different substrates. As shown in **Figure 3-13** and supported by **Figure 3-9 Ic & IIc,** the slope of the normalized P_r is steeper for the films on Si than the films on Ni. As suggested by Wang et al., the films on Si have

45

residual stress states closer to zero stress, which in turn is likely to result in a more complex domain structure, with more non-180° domain walls [117]. This is also supported by estimations from phenomenological values of the polarization and permittivity that suggest PZT on Si has roughly 60% "c" domains, resulting in a mixture of "a" and "c" [115]. Assuming a random distribution of domains, this would suggest a high concentration of non-180° domain walls. For PZT on Ni, the phenomenological values of permittivity and polarization suggest predominately "c" domains (~70-85%) and so these samples would have fewer non-180° domain walls present [115]. Although the Si substrate cannot sustain wider applied strain ranges, the motion of non-180° domain walls affects the electrical properties more significantly since "a" and "c" domains have different properties. This may result in a larger change in the electrical properties for the films on Si for the same applied stress. Conversely, PZT on Ni has a high percentage of "c" domains and therefore a limited number of "a" domains that would be able to ferroelastically switch with applied strains. This may also contribute to the smaller stress dependence of the permittivity, which for both films on Ni and Si is much smaller than hard PZT ceramics [81–83]. **Figure 3-13** also emphasizes that while the properties of PZT can be tuned by applied stresses, due to the mechanical limits imposed by failure, the PZT properties on one substrate do not overlap with the properties of the film on the other substrate. In fact, these stress ranges reported for PZT films do not overlap the stresses that maximum changes in the dielectric constants (e.g. the coercive stresses) have been reported for PZT ceramics (~70 MPa) [83]. As a result, the initial stress state of a film after fabrication largely determines the achievable stress range and magnitudes of electrical properties.
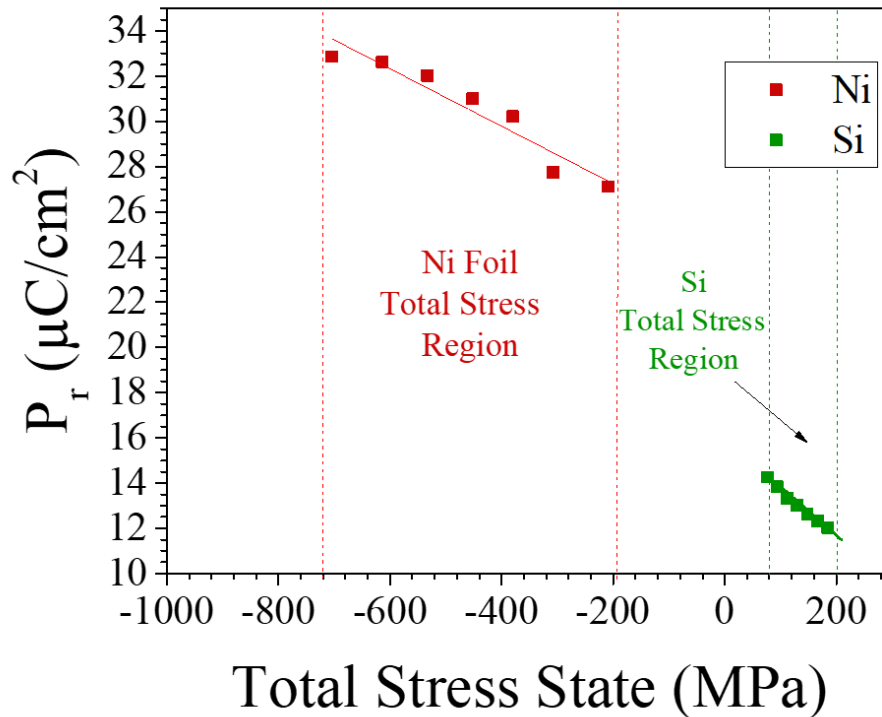
Figure 3-13. Working total stress ranges for the films on the two substrates. The difference of these working ranges slightly affects the slope of the properties changes as a function of stress, as well as the complexity of the domain structure in these films on different substrates. Data for this plot comes from the experiments shown in **Figure 3-9**.

3.5   Conclusions

The permittivity, remanent polarization, and piezoelectric properties all depend approximately linearly on the stresses in the PZT film. It was shown that the magnitude of the $e_{31,f}$ of PZT can be improved by applying a DC bias under compressive in-plane stress. Ferroelastic domain switching is possible on PZT films, however significant improvements in piezoelectric coefficients require alignment of these ferroelastically switched domains. Also, although larger strain could be achieved on Ni, the values for the permittivity and remanent polarization did not reach those of PZT on Si, indicating the importance of the thermal residual stress in the film on the domain structure and properties.

Chapter 4.   Extrinsic Contributions to the Dielectric and Pyroelectric Properties of Pb₀.₉₉[(Zr₀.₅₂Ti₀.₄₈)₀.₉₈Nb₀.₀₂]O₃ Thin Films on Si and Ni Substrates

This chapter investigates the differences in the extrinsic contributions to the dielectric and pyroelectric properties of Pb₀.₉₉[(Zr₀.₅₂Ti₀.₄₈)₀.₉₈Nb₀.₀₂]O₃ (PZT) films on Ni foil and Si wafers by using Rayleigh analysis, third harmonic phase angle, and Preisach analysis from 15 K to 296 K. The temperature dependence of the domain structure, domain wall mobility, and domain switching influenced the intrinsic, extrinsic, and secondary contributions to the pyroelectric coefficients. This, in turn, produced markedly different room temperature pyroelectric coefficients of ~250 μC/m^{2}K and ~100 μC/m^{2}K, respectively, for films on Ni and Si. At room temperature, the dielectric irreversible Rayleigh parameter α_{ray} was 15.5 ± 0.1 and 28.4 ± 1.6 cm/kV for PZT on Si and Ni, respectively. The higher α_{ray} value for the Ni sample suggests more domain wall motion at room temperature, which was attributed to the lower stiffness on the Ni foil compared to the ~500 μm thick Si substrate. Below 200 K, α_{ray} for the PZT Si sample exceeds that of the Ni/PZT sample. This is believed to arise from differences in the energy landscape of pinning centers for domain wall motion. It is proposed that the residual stresses not only set the preferred domain structures, but also the barrier heights for domain wall motion and domain switching.

4.1   Introduction

Pyroelectric thin films are used in infrared imagers [3,4,118–121], thermal energy harvesters [4,7,122–124], and detectors of thermal infra-red radiation [8–10,119,125–128] The performance of these devices depends on the pyroelectric coefficient, Π, of the film, which is determined by the change in polarization with temperature [8]. At zero applied field, which is the

condition for this chapter, the change in polarization with temperature depends on several factors, as shown in **Equation 4-1** [6,129].

$$\Pi_{total} = \left(\frac{\partial D}{\partial T}\right)_X + \left(\frac{\partial D}{\partial X}\right)_T \left(\frac{\partial X}{\partial x}\right)_t \left(\frac{\partial x}{\partial T}\right)_X + P_s \left(\frac{\partial \varphi_c}{\partial T}\right) \qquad (4\text{-}1)$$

The primary pyroelectric response is due to the change in the magnitude of the spontaneous polarization with temperature. There is also a secondary term due to a stress induced response due to the piezoelectric response of the film, which induces a polarization due to the change in dimensions associated with a temperature change [6,124,130]. Lastly, there also can be an extrinsic contribution from motion of domain walls or phase boundaries[131]. In the case where heating is not uniform, an additional term is also possible [129], but this is typically negligible for thin films clamped to substrates with good thermal conductivity (such as Si and metallic substrates) [6], and so it is not included in **Equation 1**. The combination of the secondary and extrinsic contributions can account for up to a third of the pyroelectric coefficient [132] with tuning of strain in the film. Studies show that changing the epitaxial stain and the thermal expansion mismatch between the film and substrate can increase the pyroelectric coefficient significantly [122,124,132,133].

It is important to recognize, however, that thermal stresses will also modulate other contributions to the net pyroelectric effect. In particular, the thermal expansion mismatch stress between the film and the substrate influences the percentage of out-of-plane "c" and in-plane "a" domains in {001} oriented perovskite films with a significant tetragonal phase fraction [18,19,75]. This changes the intrinsic pyroelectric coefficient. Additionally, changes in temperature and stress also influence the domain populations and types of domain walls present in the films, and hence the extrinsic contributions to pyroelectricity [44,117,124,132]. Finally, local stresses in the film

may pin certain types of domain walls, [72] and determine the domain wall density [117] and domain structure [132].

In PZT films, the extrinsic contribution to the pyroelectric coefficient is hard to predict due to the complex domain structure and various degrees of clamping. For example, a substrate's stiffness and thickness influence the degree of in-plane clamping experienced by the film [15,20,77] and thereby alter the extrinsic contributions to properties. Changes in the film's stress state can significantly alter the amount of domain wall motion; this has been demonstrated by reduction of stress through releasing the films from the underlying substrate [20,43,134], as well as by varying epitaxial strains [132]. However, to date, the relationship between stresses and domain wall pinning sites is not fully understood. This complicates prediction of the functional pyroelectric, dielectric, and piezoelectric responses of ferroelectric thin films, and reduces the accuracy of calculations on the high field response of sensors and actuators.

For example, stresses may affect the extent of domain wall motion at low fields, and domain nucleation and growth at higher fields. Therefore, the influence of stresses should be explored using both low and high field methods. At lower fields, the dielectric non-linearities of many ferroelectrics can be described through the Rayleigh law (**Section2.4.1**) [40,42], as in **Equation 4-2**.

$$\varepsilon_r = \varepsilon_{init} + \alpha_{Ray} E_{ac} \qquad (4\text{-}2)$$

where ε_{init} captures the response due to reversible domain wall motion and intrinsic contributions and α_{Ray} quantifies the irreversible domain wall motion (α_{Ray}) to the permittivity. Analysis of the Rayleigh response for films on various substrates [15,44] suggests that films with flexible substrates exhibit higher domain wall contributions to the properties than more fully clamped films on rigid substrates. Because domain wall motion is thermally activated, temperature dependent

Rayleigh measurements can provide one means of semi-quantifying the depth of the potential wells pinning domain walls, since at low temperatures, mobile interfaces can be frozen out of the response [36].

To confirm Rayleigh behavior at lower temperatures, the phase angles (δ_i) of the higher harmonics of the dielectric response can be used to determine the Rayleigh regime [36,54]. In particular, δ_3 should be at -90° (note a change in sign convention between references [135,136] and reference [54]). It has been shown that the phase angle may require a threshold field to reach the Rayleigh regime at some temperatures, which can give insight into the energy barrier ranges for domain wall motion.

Additionally, Preisach distributions (or more generally first order reversal curve (FORC) distributions) [55,57,58] describe the switching distributions over a much wider range of fields than is captured by Rayleigh behavior [58]. These models describe switching in terms of a distribution of hysterons, where each hysteron has a characteristic positive switching field (α) and negative switching field (β) [58]. It is assumed that α is greater than ß. See **Section 2.4.2** for more detail. While this model does not illuminate the detailed mechanisms for switching, it does allow the temperature dependence of the switching distributions to be described. This is useful as the local coercive fields depends on the pinning of domains through imprinting [35,45] and the variation in stresses [47,52] and clamping [47,48] of the films. Since the FORC distribution covers a higher field range, it may suggest some differences in pinning centers which may lead to different ideal poling conditions of films under different stress states. Determining these differences in energy barrier height for low field and high field conditions is necessary to fully quantify and exploit the extrinsic response of the film to optimize various properties.

In this chapter, the link between extrinsic contributions to the dielectric and pyroelectric properties based on stresses in 0.6 µm thick $Pb_{0.99}\square_{0.01}[(Zr_{0.52}Ti_{0.48})_{0.98}Nb_{0.02}]O_3$ (PZT) films on Ni and Si substrates was explored. PZT was used since it has good piezoelectric and pyroelectric coefficients and is used in many commercial applications [1,2]. Rayleigh and Preisach analysis as well as δ_3 values were used to compared domain wall motion at low fields and switching behavior at high fields from 10 K up to room temperature (296 K). From these results, working models of the potential energy landscapes and domain structure were developed to convey the differences in extrinsic contributions from one PZT thin film to another, based on residual stresses.

4.2   Experimental Procedure

The 0.6 μm PZT films used in this study were the same series of films grown in **Chapter 3**. Details of the chemical solution deposition (CSD) process using a 2-methoxyethanol based solution [15,44,105] are described in **Section 3.2.1**. The X-Ray diffraction patterns and FeSEM images of these films are shown in **Figure 3-6**.

The pyroelectric coefficient of PZT on Ni and Si were measured by heating the substrates using a cartridge heater powered by a 50% duty cycle square wave while monitoring the temperature and sample current. **Equation 4-3** relates the pyroelectric coefficient, Π, to heating/cooling and sample properties

$$\Pi = \frac{I_\Pi}{A\,{dT}/{dt}} \tag{4-3}$$

where A is the current collection area, I_Π is the pyroelectric current, T is temperature and t is time. For the temperature measurement, a co-located, surrogate thin film platinum resistive thermal device (RTD) was used estimate the pyroelectric thin film temperature. The thermal properties of the Ni and Si substrates were modeled to ensure the accuracy of the surrogate RTD chip [133]. Additional electrical characterization of the films was performed using a Lakeshore Cryotronics

8400 series temperature-controlled probe station from 10 K to 296 K. Samples were adhered to the stage using a thin layer of GE Varnish to ensure good thermal contact. A Cernox thin film RTD cryogenic temperature sensor on a glass substrate was adhered on the stage using a thin layer of GE varnish near the samples to monitor the temperature. Measurements as a function of temperature were made on heating from 10 K.

First, P-E hysteresis loops were measured using a custom built electric field loop system using a AC voltage amplifier (790 series power amplifier Piezotronics Inc.) described elsewhere [45,137]. One set of loops was measured up to 400 kV/cm at 100 Hz and the coercive field (E_c) and remanent polarization (P_r) were recorded. Since the E_c drastically increases with decreasing temperature, polarization hysteresis loops were repeated at 4x E_c to obtain fully saturated loops.

Low field measurements of permittivity of PZT on Ni and Si were acquired using a Hewlett Packard LCR meter at 1 kHz and 30 mV AC signal [136]. The first, second, and third harmonics of the permittivity and their respective phase angles at 1 kHz were determined using a lock-in amplifier as an AC voltage source, which was swept up to half the coercive field at each temperature. Rayleigh measurements of the permittivity were taken at 1 kHz using the LCR meter and an AC signal up to 25 kV/cm. The Rayleigh parameters were determined by a linear best fit in the Rayleigh regime [43].

To probe the dielectric response at higher fields, FORC were measured using 40 loops that increased linearly in field up to 4 times the coercive field, as described elsewhere [45,137]. The field range probed was from -4E_c to +4E_c at each temperature. The Preisach distribution was determined from these loops, as described elsewhere [45,137].

4.3   Results and Discussion:

At room temperature, the pyroelectric coefficients of PZT films on Ni and Si substrates were found to be -251 and -106 $\mu C/(m^2K)$ respectively, with $\pm25\%$ standard deviation. The higher value for the film on Ni is function of the fact that this PZT film is under compressive stress, and so has a higher remanent polarization [18,122,138]. The Curie temperatures, T_c, were measured in to be ~320°C for both films (see **Figure 3-7)** [44]. This suggests domain structure may alleviate some of the residual stresses, which is plausible given the complex domain states [40,51].

There are several important points to note from the temperature dependence of the P-E hysteresis loops of PZT on Ni (**Figure 4-1a**) and PZT on Si (**Figure 4-1b**). As expected, both films showed a decrease in the P_r and E_c with an increase in temperature as shown in **Figure 4-1c** and **Figure 4-1d,** respectively. At $4E_c$, the P-E loops of PZT on Si above 150 K are not well saturated and at these higher temperatures. For temperatures above 150 K, saturated loops of PZT on Si at higher fields were used for P_r and E_c values in **Figure 1c** and **1d**, respectively. The E_c at 15 K was -257 kV/cm and 221 kV/cm for PZT on Ni, and -117 kV/cm and 104 kV/cm for PZT on Si, and at room temperature dropped to 43 kV/cm for PZT on Ni and 36 kV/cm for PZT on Si. Over the temperature range, E_c for PZT on Ni was roughly twice that of PZT on Si, as indicated by the dashed line.

At 15 K, the P_r for PZT on Ni and Si was 47.5 ± 1.4 $\mu C/cm^2$ and 19 ± 2 $\mu C/cm^2$, respectively. From phenomenology, it is estimated that "c" domains for this composition at 15 K would have a spontaneous polarization, P_s, of ~61 $\mu C/cm^2$ and "a" domains would have no contribution to the out-of-plane polarization [64]. Assuming, as a first approximation, that these films have only "a" or "c" domains and that ferroelastic domain switching is absent at 10 K; since P_r will scale with P_s, the percentage of "c" domains can be estimated. (**Figure 4-2)**. At 15 K, PZT

on Ni has ~80 vol% of "c" domains at 15 K, and PZT on Si has ~30 vol% of "c" domains. This is

lower than room temperature reports for the percentage of "c" domains of PZT on Si [19,44]. At

room temperature, the P_r is 26 µC/cm^2 (at $4*E_c$) for PZT film on Ni suggesting only ~50 vol% of

"c" domains [19,44,64]. However higher maximum electric fields (900 kV/cm) the P_r further

increases to 34.5 µC/cm^2, which would suggest ~65% "c" domains, which is lower than previous

reports [44].
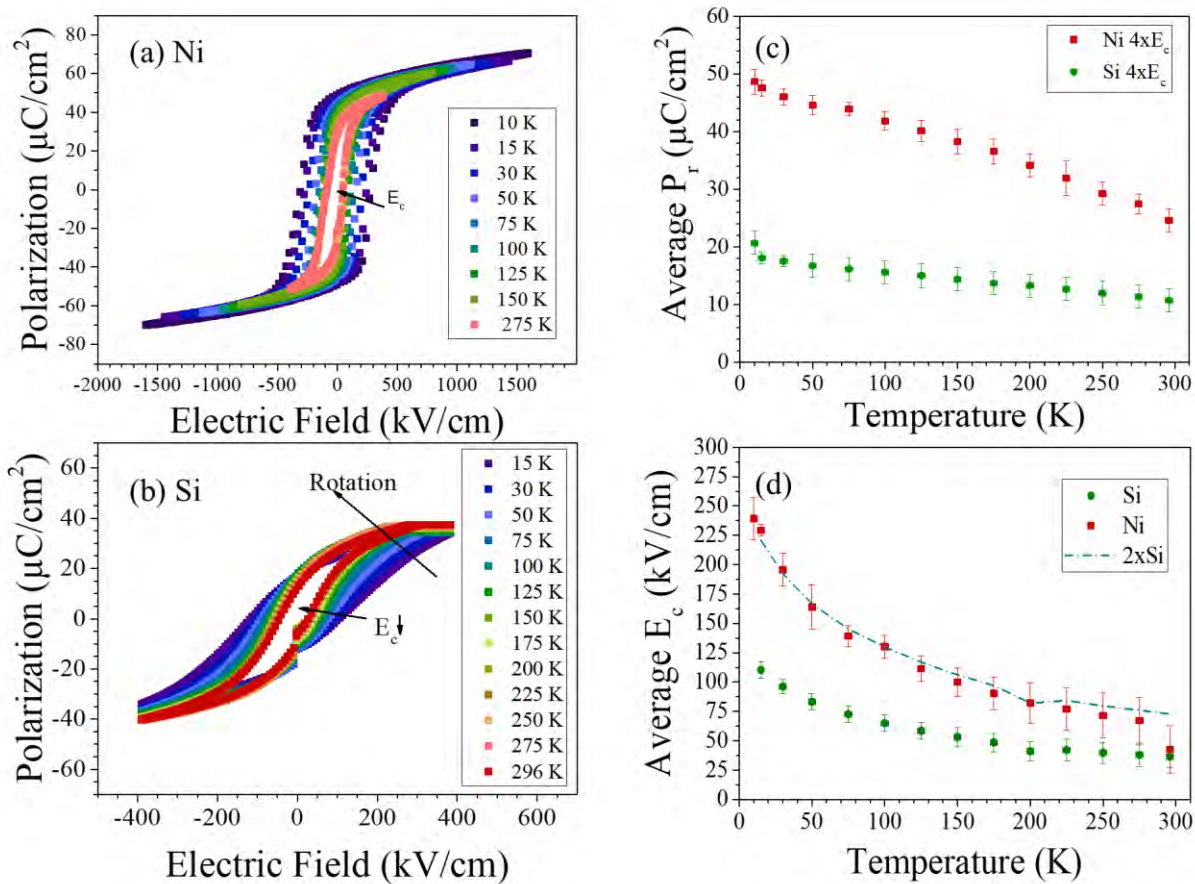
Figure 4-1. P-E hysteresis loops for PZT on Ni (a) and Si (b). The remanent polarization (c) and coercive field (d) as a function of temperature for PZT on Ni (red squares) and on Si (green circles). The E_c for PZT on Ni was roughly twice that of PZT on Si for all temperatures measured.
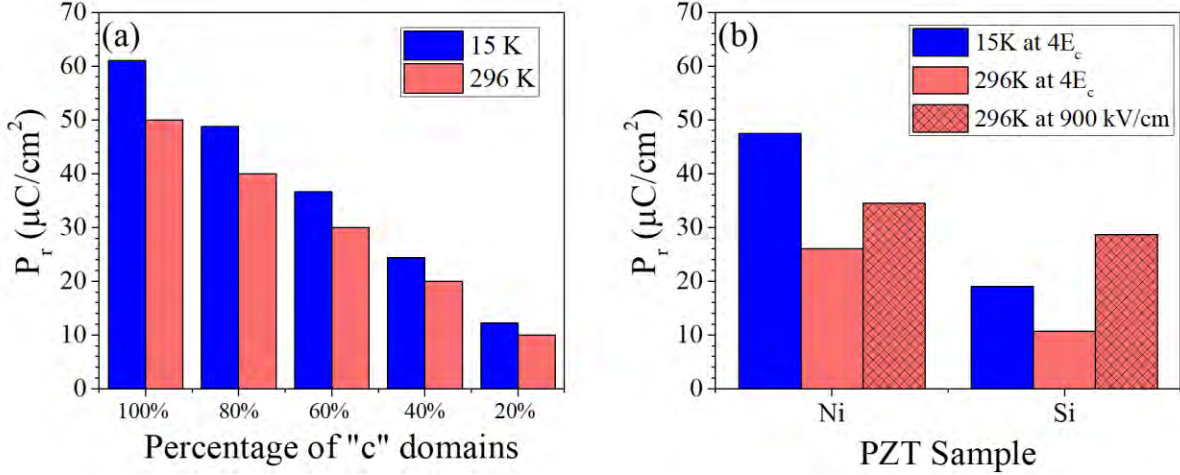
Figure 4-2. Estimated P_r values from phenomenology at 15 K (blue) and 296 K (pink) based on the percentage of "c" domains (a), and the observed P_r for PZT samples on Ni and Si.

The difference in the volume fraction of "c" domains at 15 K and room temperature can be attributed to extrinsic contributions to the property changes or to domain reorientation with changes in stress with temperature, or a combination of these. The stress changes in the film due to thermal expansion mismatch stress (σ_t) is defined by **Equation 4-4**. α_{CTE} is the coefficient of thermal expansion, v is the Poisson's ratio, Y is the Young's modulus and t is the thickness for the film (f) and substrate (s).

$$\sigma_t = \frac{\int_{T_c}^{T max}(\alpha_{CTE,f}-\alpha_{CTE,s})dT}{\left\{\frac{1-v_f}{Y_f}+\left(\frac{1-v_s}{Y_s}\right)\left(4\frac{t_f}{t_s}\right)\right\}} \tag{4-4}$$

For the temperature range used here (15 K to 296 K) the α_{CTE} for Ni varies from 0.02 to 13.3 ppm/K [113,139] and Si from -0.5 to 2.6 ppm/K [112,140]. The α_{CTE} for PZT below 273 K has not been reported, but in the ferroelectric regime α_{CTE} has been reported to be roughly 2 ppm/K [18,114,141]. The volumetric thermal expansion coefficient was estimated from the results in [142–144] and below 60 K it is assumed that the α_{CTE} for PZT decreases linearly to 0 ppm/K as 0 K is approached for the calculation. Therefore, approximately -200 MPa and -5 MPa more stress is added to PZT on Ni and Si, respectively, when it is cooled from room temperature down to 15

56

K. The small change in stress for the sample on Si produces little ferroelastic switching, such that the volume fraction of "c" domains is approximately constant at cryogenic temperatures. As shown in **Figure 3-13**, the P_r of PZT films on Ni would increase by 2.5 µC/cm^2 under -200 MPa [44], which suggests an increase in "c" domains as the temperature is reduced [64], but additional contributions must be considered since there are limitations to these phenomenological assumptions [51].

Rayleigh behavior and higher harmonics of the dielectric constant were investigated down to 10 K to determine the extent of domain wall motion at lower temperatures. At the onset of the Rayleigh regime, the phase angle of the third harmonic switches from -180° to -90° as domain walls begin to contribute to the permittivity [54] (note that the sign of the phase angle has been changed to be consistent with recent reports [135]). The first, second, and third harmonics are reported in **Appendix.** For perfect Rayleigh behavior in an unpoled sample, only the odd harmonics should be present [145]. However, small values for the second harmonic were seen and attributed to slight poling of the samples with the applied field, which is consistent with previous studies on PZT films [145].

Figure 4-3 shows that the third harmonic phase angle for PZT on Ni and Si shifts from -180° to -90° on increasing magnitude of the electric field. Consistent with previous reports [54], there is a threshold field required to reach -90°, suggesting that the entire energy landscape distribution for domain wall motion is greater than 0 eV. As the temperature decreases, the AC field required to reach the Rayleigh-like regime rises. The field where the third harmonic phase angle first reaches $-90 \pm 5°$ is denoted as $E_{\delta3}$. It is notable that there is a larger deviation from the 90° phase angle for films on Si, relative to films on Ni. The results were reproducible, but the origin of this behavior is not known, but may indicate an additional conduction mechanism. This

may cause additional error with determining $E_{\delta 3}$. PZT on Ni shows a greater temperature dependence, where at 296 K $E_{\delta 3}$ is 5.8 ± 0.8 kV/cm and at 75 K, $E_{\delta 3}$ is 19 ± 0.8 kV/cm. For PZT on Si, $E_{\delta 3}$ is ~ 5.8 ± 0.8 kV/cm at room temperature and increased to ~ 9.2 ± 0.8 kV/cm at 75 K.
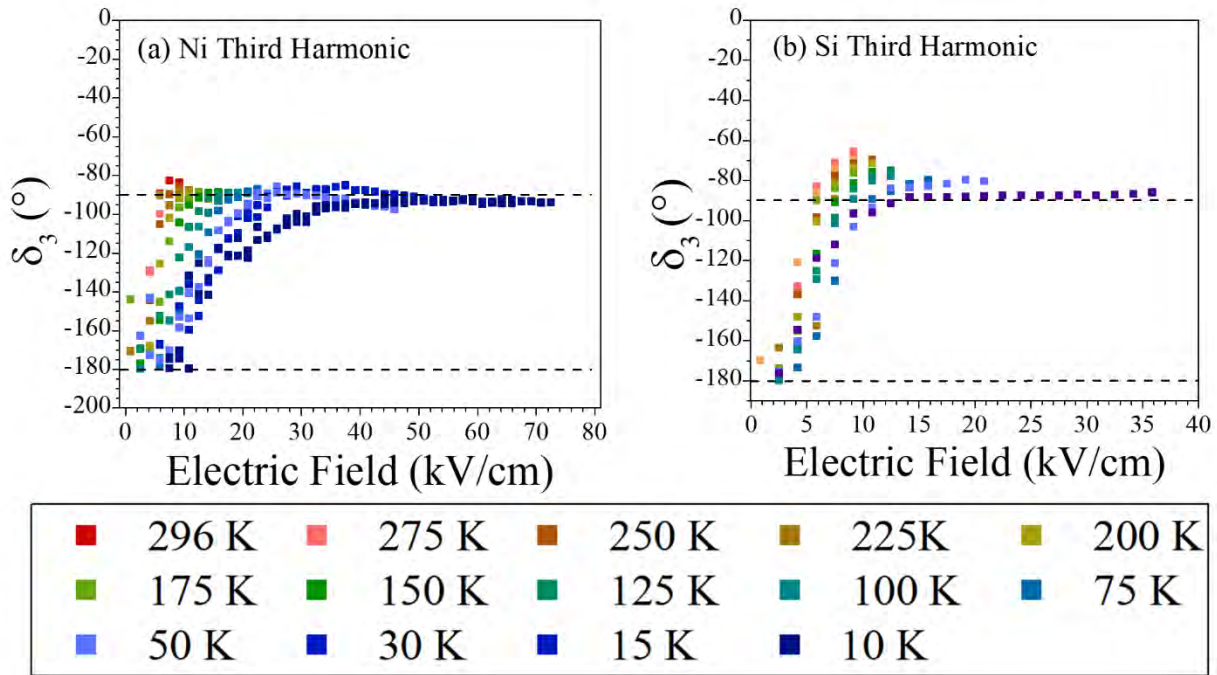
Figure 4-3. Third harmonic phase angle, δ_3, for PZT on Ni (a) and on Si (b) from room temperature down to 10 K. The field (E_{δ_3}), where the phase angle reached -90 ±5° is used as a proxy for defining when Rayleigh-like behavior was present. As the temperature decreases, $E_{\delta 3}$ increases. This temperature dependence is shown to be greater for PZT on Ni as seen by the larger electric field required to reach a -90° phase angle.

Figure 4-4 plots the $E_{\delta 3}$ vs. E_c. For all temperatures investigated, the Rayleigh like behavior begins at consistent percentage of E_c. For PZT on Ni. $E_{\delta 3}$ ranges from 7-15% of the E_c, for both films at the various temperatures. This slight differences at each temperature may suggests there may be some differences in the magnitudes and distribution of pinning centers. However, it is possible that multiple mechanisms can affect the onset of the Rayleigh regime, and the percentage of E_c that corresponds to the onset of the Rayleigh regime may differ with temperature.

58
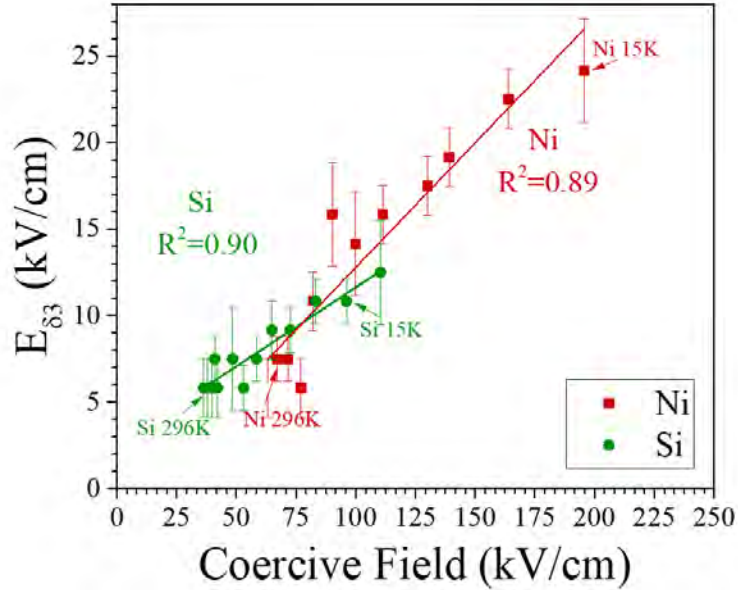
Figure 4-4. The E_{δ_3} vs. coercive field for PZT on Ni (red square) and Si (green circle). From the slope (m) of these lines, it is estimated the Rayleigh regime begins around 9-14% of the coercive field for both PZT on Si and for PZT on Ni.

These results were combined with Rayleigh analysis to understand the differences in the contributions to the dielectric response. Rayleigh analysis was performed as a function of temperature from 10 K up to 296 K for PZT films on Ni and Si substrates, as shown in **Figure 4-5**. The Rayleigh coefficients were determined using a linear fit of the permittivity data vs electric field. The linear fits were taken for a minimum of five points above the corresponding E_{δ_3} for that temperature and sample. The Rayleigh coefficients of $\varepsilon_{\text{init}}$ (**Figure 4-5c**) and α_{ray} (**Figure 4-5d**) are plotted as a function of temperature for PZT on Ni (red squares) and Si (green circles). As thermal energy was added to the films, $\varepsilon_{\text{init}}$ increased for both sample sets. However, changes in these coefficients with temperature occurred at slightly different rates for PZT on Si and Ni. PZT on Ni had ε_{init} of 188 ± 0.3 at 10 K and 690 ± 8 at 296 K, and PZT on Si had a ε_{init} of 326 ± 0.3 at 10 K and 1065 ± 3 at 296 K.
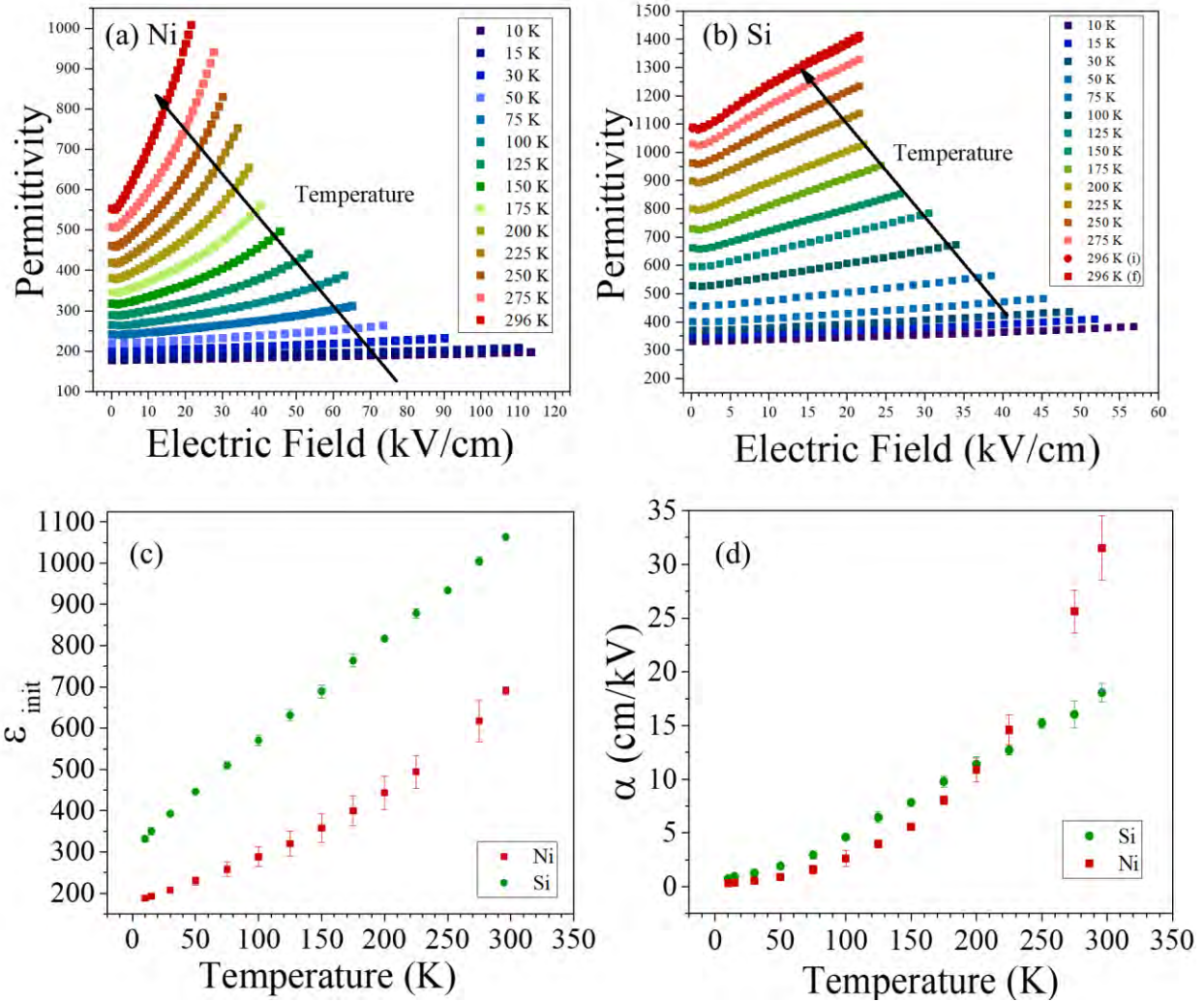
Figure 4-5. Permittivity as a function of electric field within the Rayleigh regime for (a) Ni and (b) Si samples. Rayleigh parameters of ε_{init} (c) and α_{ray} (d) were plotted as a function of temperature for PZT films on both Ni (red squares) and Si substrates (green circles). Note: 296K (i) indicates the permittivity values at room temperature at the start of the experiment and 296 K (f) indicates the values at room temperature after the experiment. The lack of clear differences indicates that the sample had minimal aging through the experiment.

At room temperature, α_{ray} is larger for PZT on Ni than Si, which may be due to the flexibility of the Ni foil. The Ni foil substrate produces less clamped films compared to PZT on Si; leading to more mobile domain walls [20,43]. As the temperature decreases, α_{ray} converges to zero near 10 K. The rate at which α_{ray} decreases is different for PZT on Ni and PZT on Si, suggesting that irreversible domain wall motion "freezes out" differently for these two types of

samples. At 10 K, α_{ray} is 0.33 ± 0.01 cm/kV for PZT on Ni and 0.56 ± 0.03 cm/kV for PZT on Si. For temperatures below 200 K, α_{ray} is higher for PZT films on Si relative to Ni, but this order reverses near room temperature.

To investigate the differences in the irreversible contribution, the $\alpha_{Ray}/\varepsilon_{init}$ ratio was determined for the two samples in **Figure 4-7**. These differences in α_{ray} and $\alpha_{Ray}/\varepsilon_{init}$ as a function of temperature could be due to either differences in the domain structure or differences in the energy barrier height distribution. It is estimated that PZT on Si has roughly 40-60% "c" domains, and PZT on Ni has a higher percentage of "c" domains (around 80-95%) [44,64,115]. Thus, it is likely that PZT films on Si have more non-180° domain walls. Since any motion of non-180° domain walls produce a large change in permittivity (as "a" and "c" domains have very different permittivity values), this could account for the higher α_{ray} at lower temperatures. However, this theory would be inconsistent with reports of limited amount of ferroelastic domain wall motion in films [46,72]. Therefore, it is more likely that there are lower energy barrier heights for PZT on Si, allowing for a slightly greater α_{ray} at lower temperatures. This is also supported by the increase in the magnitude of stress on the PZT film on Ni (calculated by **Equation 4-4).** This may cause increases in pinning centers energies of the PZT on Ni and lead to the larger decay of α_{ray} with temperature.
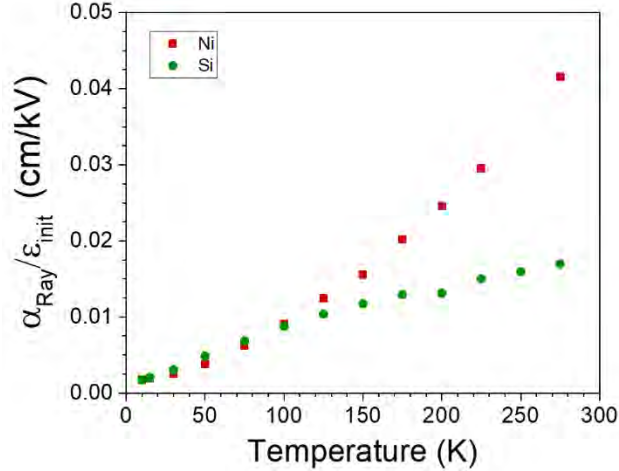
Figure 4-6. $\alpha_{Ray}/\varepsilon_{init}$ ratio for PZT on Ni (red squares), and on Si, (green circles).

Rayleigh behavior is observed when there is a Gaussian distribution of the restoring forces for domain walls. Presumably, as the temperature decreases, a smaller fraction of the distribution can be sampled for a given electric field. As a semi-quantitative approach to describing this, an Arrhenius-type plot was made for α_{ray}, to approximate some average value for a pseudo-activation energy for domain wall motion at each temperature (**Figure 4-7**). Above 250 K, the pseudo-activation energies for PZT films on Ni and Si as 32.4 ± 3.2 meV and 16.9 ± 1.1 meV, respectively. At room temperature there is ~25 meV available, suggesting without the presence of an electric fields some domain walls are mobile. This observation is consistent with the common observation of aging of properties that depend on domain wall motion. Comparing the two activation energies, PZT on Ni has the higher pseudo-activation energies, which is consistent with the larger E_c and $E_{\delta3.}$ As the temperature decreased, the pseudo activation energies decreased. That is, when the thermal energy is low, irreversible domain wall motion from deeper wells may be frozen out in these systems; since only the shallower wells can be sampled, the pseudo activation energies drop with decreasing temperature. As the temperature increases, deeper wells can be overcome with the

increase in thermal energy; a rise in activation energies and α_{ray} value follows. This occurs at a steeper rate for PZT films on Ni.
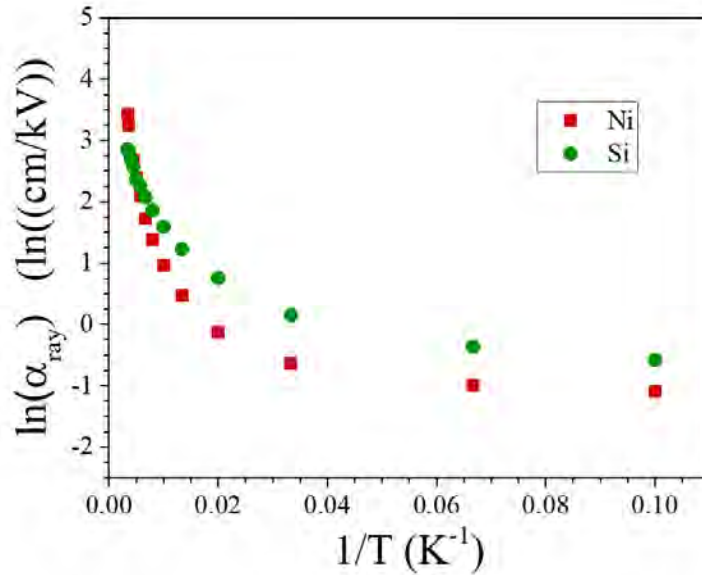
Figure 4-7. Arrhenius plot of the natural log of α_{ray} vs 1/T to determine the ranges of activation energies for irreversible domain wall motion for PZT on Ni (red circle) and PZT on Si (green square). From the slope the calculated activation energy at higher temperatures (from a linear fit form 225K to 296K) PZT on Ni and Si was 32.4 ± 3.2 meV and 16.9 ± 1.1 meV, respectively.

The Rayleigh behavior and the phase angles of the dielectric constant indicate significant differences in the domain wall motion at modest electrical fields. To investigate higher fields, FORC loops were measured for PZT films on Ni (**Figure 4-8**) and on Si (**Figure 4-9**) substrates, from 15 K to 296 K. At lower temperatures, the FORC loops are squarer. As the temperature increased for both films, the polarization of the loops decreased and the loops becomes tilted. PZT films on Si had lower P_r, which is consistent with the hysteresis loops in **Figure 4-1.** This is believed to be due to differences in the residual stresses and the percentage of in-plane and out-of-plane domains in the two films [18]. The films on Ni are consistently under compressive stresses

and therefore will have more out-of-plane domains and the higher P_r for all temperatures measured.
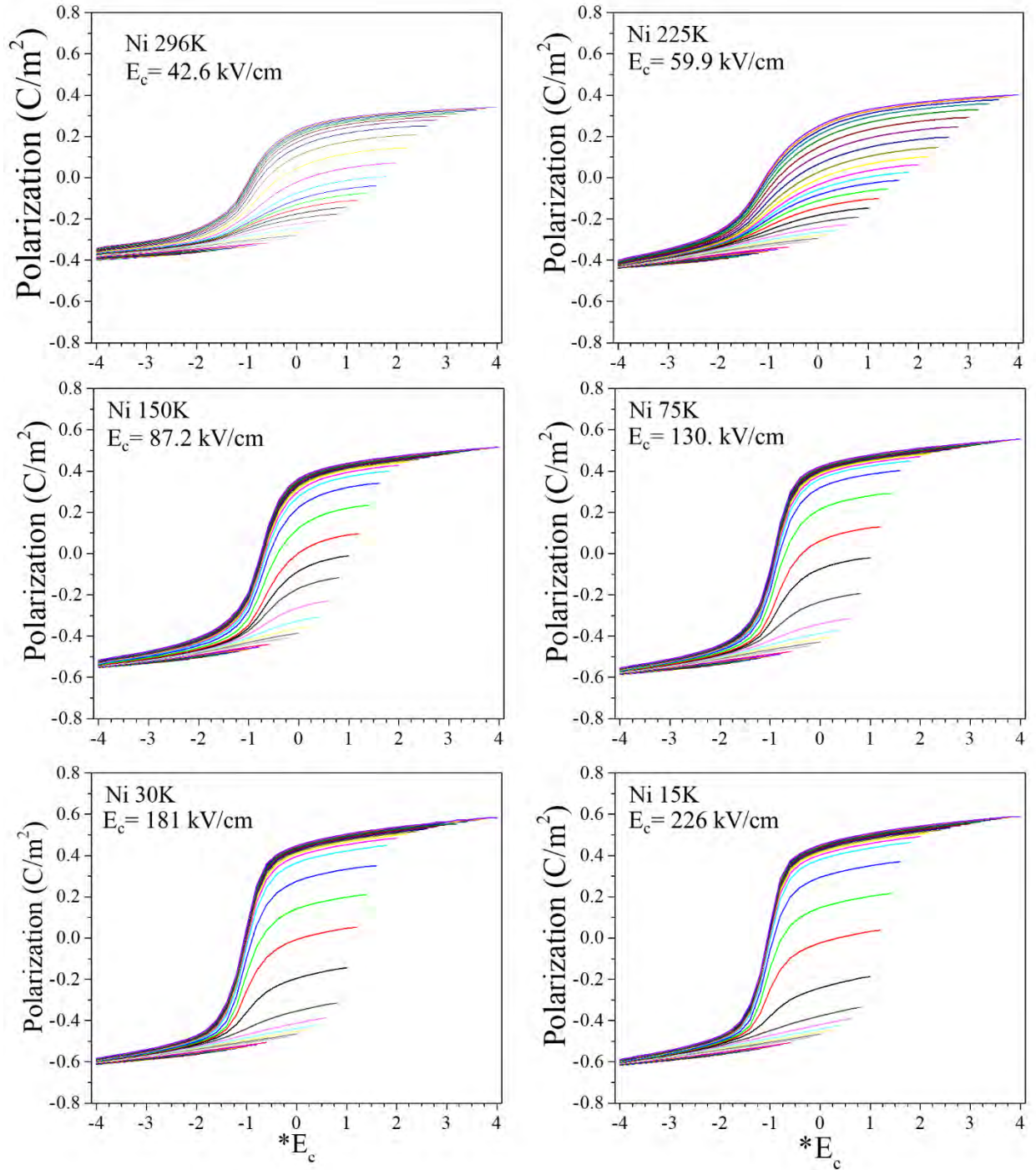
Figure 4-8. FORC loops for PZT films on Ni at 296 K, 225 K, 150 K, 75 K, and 15 K. The field range was from -4E_c to +4E_c for each temperature.
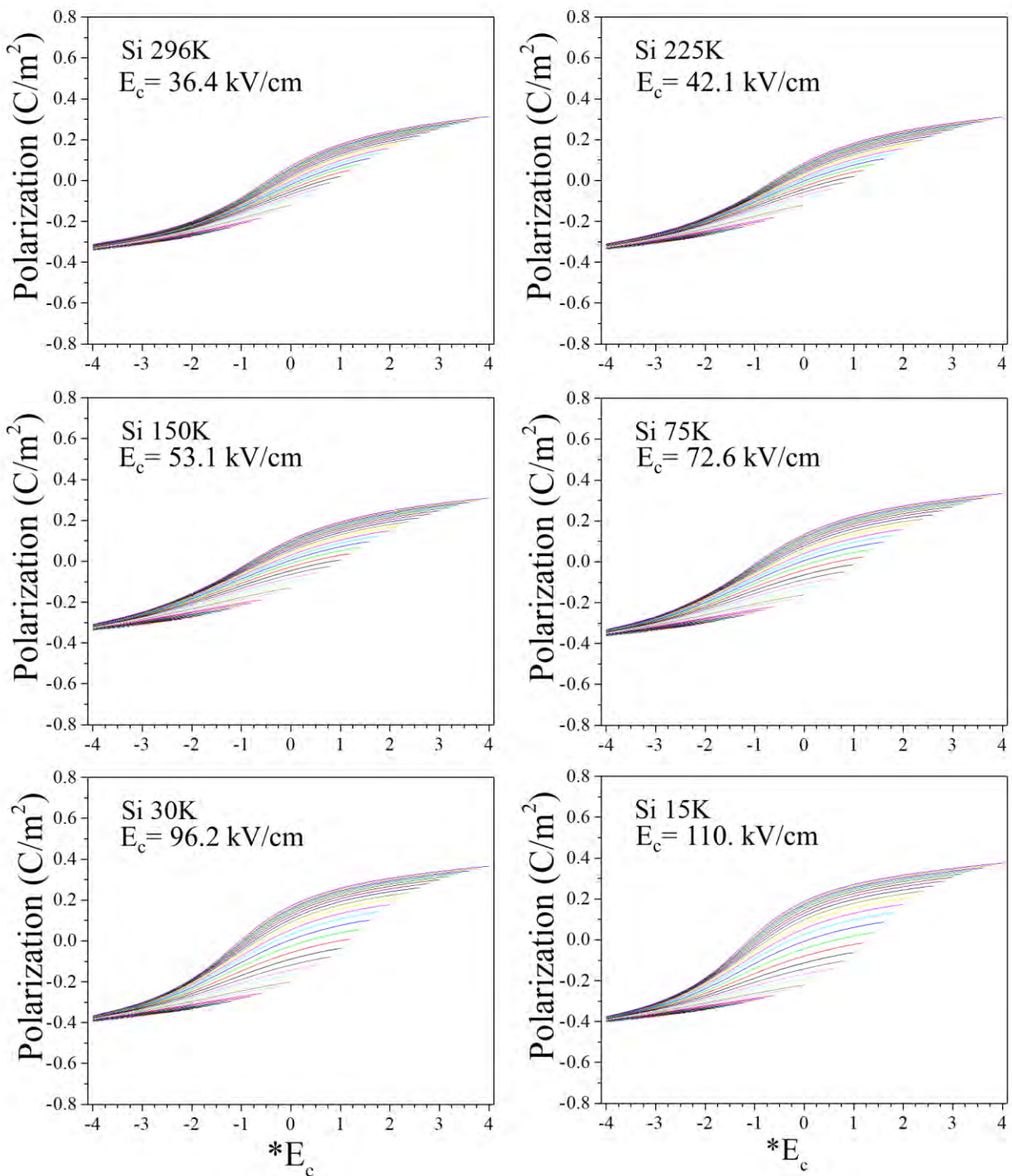
Figure 4-9. FORC loops for PZT films on Si at 296 K, 225 K, 150 K, 75 K, and 15 K. The field range was from -4E$_c$ to +4E$_c$ for each temperature.

The reversible (P_{rev}) and irreversible (P_{irr}) FORC distributions were determined. **Figure 4-10** shows the reversible Preisach distribution. P_{rev} is the part of the hysteron distribution that corresponds to the up (α) and down (β) switching fields being equivalent. P_{rev} for PZT on Si was symmetrical around 0 kV/cm; however, this was not the case for PZT on Ni for all electrodes measured. As the temperature increased, the peak magnitude increased for both PZT on Ni and Si. The reversible peak was much larger for PZT on Si than PZT on Ni. The typical shape of the hysteresis loops confirms this (**Figure 4-1, Figure 4-8** and **Figure 4-9**), as PZT on Si has a tilted hysteresis loop compared to PZT on Ni. The differences in shape of the loop would suggest some differences in the Preisach distributions for the two films.
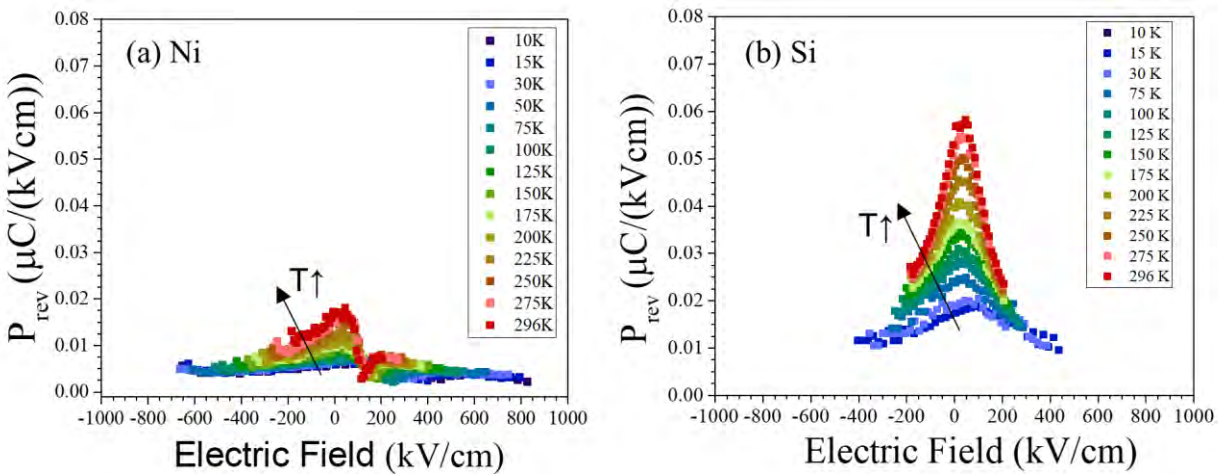
Figure 4-10. Reversible FORC data, P_{rev} for PZT films on Ni (a) and PZT films on Si (b). The P_{rev} for PZT on Si was 2-3 times larger than PZT on Ni.

The P_{irr} distribution (where $\alpha \neq \beta$) is shown in **Figure 4-11** and **Figure 4-12** for PZT on Ni and Si, respectively. PZT on Ni had a clear peak around $\alpha = 2*E_c$, $\beta = -E_c$ for each respective temperature. The location of this peak may be due to imprint on the sample from poling prior to the FORC loop. As the temperature increased, this peak broadens and the intensity increased. This

suggests that as the temperature increases, more hysterons can switch. This is consistent with the increase in the P_{rev} distribution. It is not clear how individual pinning center's barrier heights change with temperature. However, the decrease in residual stress at higher temperatures for PZT on Ni may change individual barrier heights.
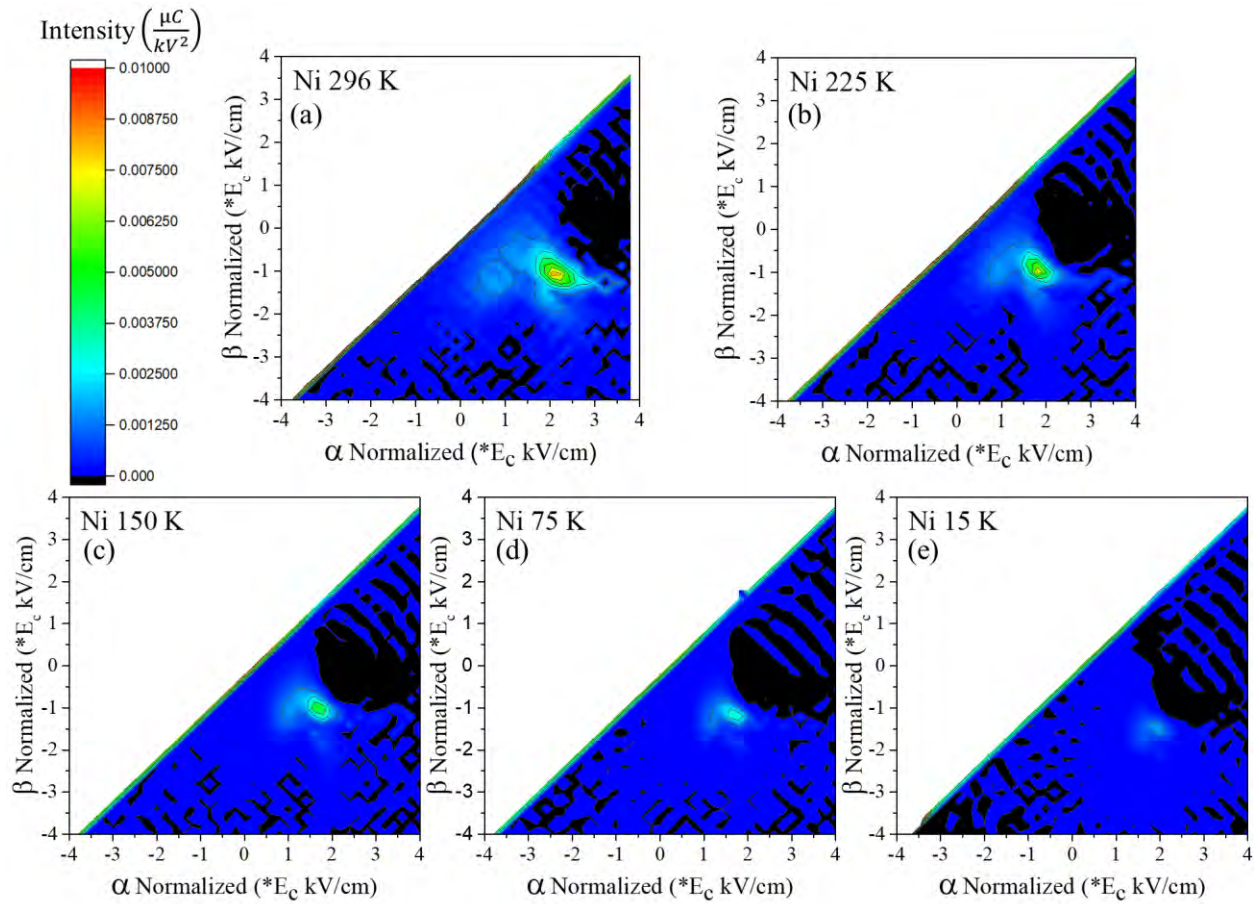
Figure 4-11. P_{irrev} for PZT on Ni at 296 K (a), 225 K (b), 150 K (c), 75 K (d), 15 K (e). Alpha and Beta are normalized to 4 times E_c at the reported temperature.

PZT on Si (**Figure 4-12**) does not show a clear peak but does show a wide distribution of hysterons (note the scale difference between **Figure 4-11** and **Figure 4-12**). This may suggest differences in the distribution of barrier heights between PZT on Ni and on Si. The center of P_{irr}

on Si gradually moves closer to the $\alpha=\beta$ line as the temperature increases, producing a more reversible response, and a more tilted hysteresis loop.
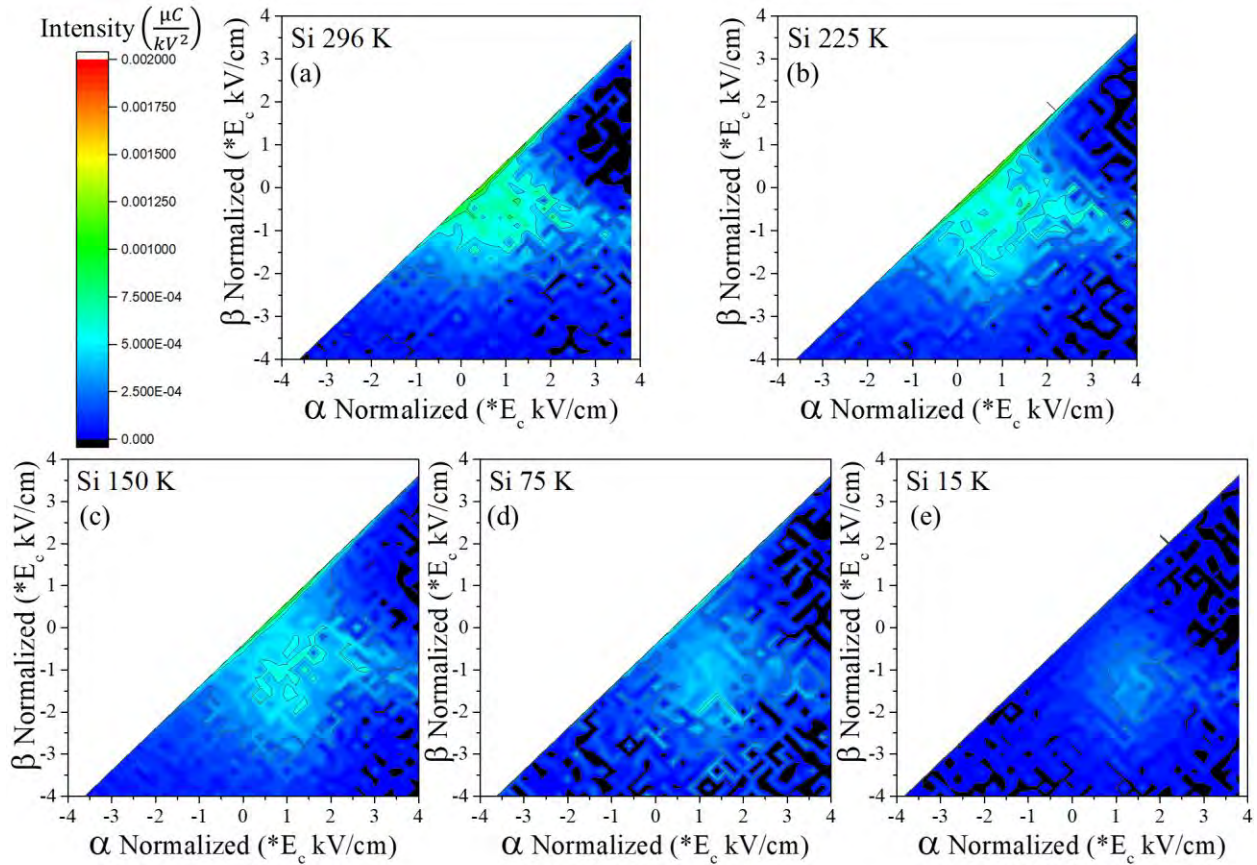
Figure 4-12. P_{irrev} for PZT on Si at 296 K (a), 225 K (b), 150K (c), 75 K (d), 15 K (e). Alpha and Beta are normalized to $4E_c$ at the reported temperature.

These electrical characterization techniques show some variations in the distributions and barrier heights for domain wall motion and domain reorientation in films on Ni and Si. **Figure 4-13** illustrates the differences in this barrier distribution schematically. PZT on Ni and Si exhibit Rayleigh behavior and Gaussian-like pinning center distributions. However, as indicated by the δ_3, this distribution does not continue to 0 eV, but down to 10-15% of E_c. It is unlikely that the tail of the Gaussian distribution reaches 0 as shown in **Figure 4-13**.

PZT on Si has lower pseudo activation energies, E_c and $E_{\delta3}$ at each temperature. If it is assumed that the same number of hysterons is present in each sample, then the PZT on Si would be expected to have more hysterons with lower energies. As a result, the center of the distribution is shifted to the left for PZT on Si compared to PZT on Ni. As indicated by the larger pseudo activation energies, coercive fields, and larger irreversible Preisach density for PZT on Ni, the center of the barrier height distribution is expected to be at a higher energy than PZT on Si. The lower energy barrier heights for PZT on Si allows for a slightly greater α_{ray} at lower temperatures.

Because of the sharp Preisach peak and the large increase in α_{ray} with temperature, it is anticipated that the PZT on Ni has a narrow distribution. Small increases in thermal energy will increase the number of switchable hysterons, noted by the increase in the area under the curve with higher temperatures (**Figure 4-13)**. Higher temperatures in turn increase the total energy in the system, allowing for more barriers to be overcome at the same exciting electric field. In the schematic **Figure 4-13**, this increase would be represented by the area under the curve up to the dashed line, where the dashed line represents the energy available at each temperature. As the temperature increases, the dashed line would move further to the right, and more barriers could be overcome with the available energy. For the same temperature change (right shift of the dashed line) and same number of total hysterons, the sample with the narrow distribution would see larger changes in the total number of hysterons that can be switched and thus more domain wall motion. This is consistent with the experimental observation of PZT on Ni. Assuming the same number of hysterons, the intensity of the Gaussian peak would be then larger for PZT on Ni.

Additionally, there is a temperature-induced stress change for PZT films on Ni. With decreasing temperature, the magnitude of the residual stress in the PZT layer increases. This increase in stress in the film may increase the depth of the potential wells for domain wall motion

and lead to the rapid decrease in α_{ray} with decreasing temperature. Exactly how each individual pinning center changes with stress is unknown. To schematically represent this, the Ni pinning distribution could shift to the right with increasing temperature and reduction in the thermal expansion stress. This shift in the pinning distribution, the narrower distribution, or a combination of both would cause α_{ray} to increase more rapidly for PZT on Ni.
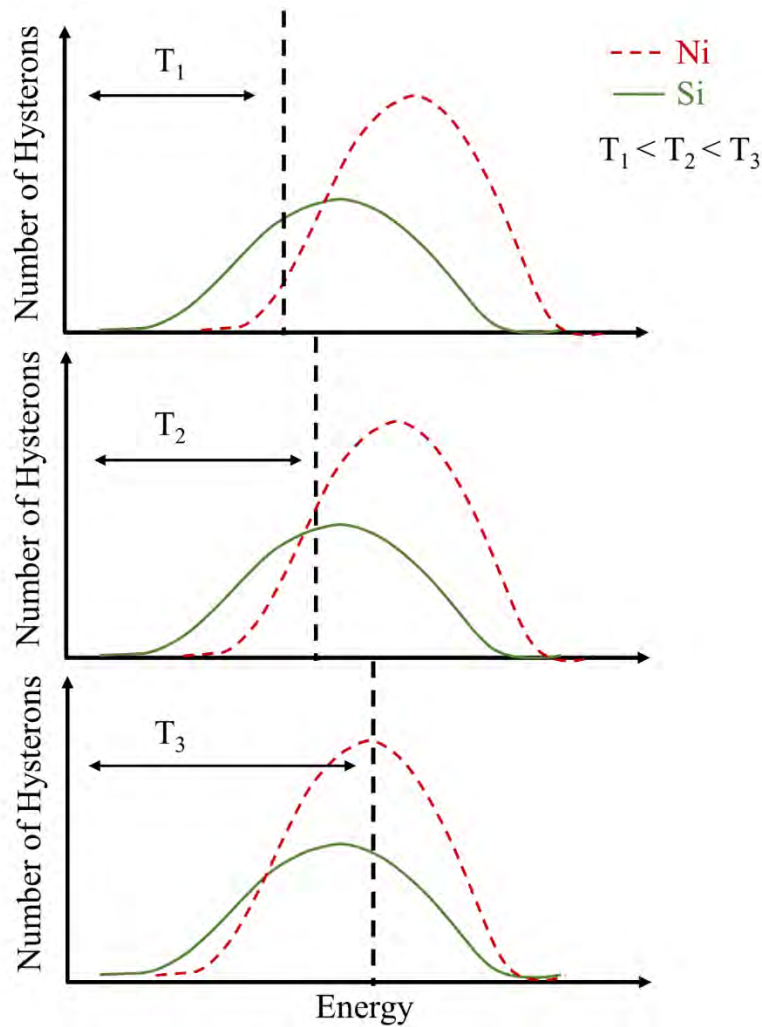
Figure 4-13. Schematic of distribution of the population of hysterons with certain pinning energies for PZT on Ni (dashed red curve) and Si (solid green curve). The vertical dashed black line represents the available energy at a given temperature. Any pinning center with lower energy levels is anticipated to be overcome at that temperature.

With the various differences in extrinsic contributions of these films in mind, the pyroelectric coefficients at room temperature were further probed. Recalling **Equation 1**, and the

large differences in π, the different terms of the measured π were determined. The secondary contribution, which combines stress and piezoelectric contributions, manifests in clamped thin films as **Equation 4-5** from the work of Zook, *et al.*[130].

$$\pi_{secondary} = \frac{2d_{31}(\alpha_f - \alpha_s)}{s_{11} + s_{12}} \qquad (4\text{-}5)$$

For PZT on Ni $\pi_{secondary}$ was calculated to be approximately -147 $\mu C/m^2K$, and for PZT on Si, $\pi_{secondary}$ is 45 $\mu C/m^2K$. The observed pyroelectric coefficient is the sum of the primary, extrinsic, and secondary term. Therefore, the primary plus extrinsic piece for PZT on Ni would be around -100 $\mu C/m^2K$ and for PZT on Si would be around -150 $\mu C/m^2K$. As shown by the larger P_r, PZT on Ni has more out of plane "c" domains and a larger primary piece. Therefore, for this sum to be smaller, the film on Ni must have significantly smaller extrinsic piece. This smaller extrinsic term may be due to higher pinning energies, which is suggested by the various electrical characterization techniques used in this study and schematically shown in **Figure 4-13**.

Overall, this study suggests that the distribution of pinning centers for PZT films on Ni and Si are different; this induces different reversible and irreversible Rayleigh and Preisach distributions as a function of temperature. Given that the grain sizes are very similar for these two sets of films, it is believed that the residual stress accounts for at least some of the differences in the two families of films. Large differences in residual stresses will affect the film's domain structure, including the percentage of in-plane and out-of-plane domains and the energy landscape of various pinning sites for domain wall motion and domain switching. While these extrinsic contributions are typically considered to account for a small percentage of the total pyroelectric response, the combined influence of fabrication, stress, temperature on the domain structure and

71

substrate mechanical properties can result in a much more significant impact than one would expect.

4.4 Conclusions

PZT on Ni has a larger pyroelectric coefficient compared to PZT grown on Si, which is due to a large secondary contribution. However, the extrinsic contribution may be significantly reduced due to the residual stresses. PZT on Si and Ni have very different reversible and irreversible Rayleigh and Preisach coefficients. It is proposed that larger differences in residual stresses drastically change the film's domain structure. Stress may allow for differences in the energy landscape of various pinning sites for domain wall motion and domain switching. These differences will lead to significant changes in the film's properties at various temperatures. With different energy barriers distributions, these films may have different optimal poling and driving conditions for high device performance. Further study should include defect chemistry, composition, and thickness on the distributions of pinning sites as well as designing films/substrate stack with lower energy barrier for domain wall motion to further improve the pyroelectric coefficient.

Chapter 5. __Thickness Dependence of Crack Initiation and Propagation in PZT/Si Stacks__

This chapter focuses on determining the relationship between PZT film's thickness and the mechanical limits of the PZT film and the stack. PZT/LaNiO$_3$/SiO$_2$/Si stacks with different PZT thicknesses (from 0.6 to 1.8 µm) were tested using the ball on three ball (B3B) biaxial test method. Strength distributions of the stacks were evaluated using Weibull statistics and compared to the reference SiO$_2$/Si samples. The characteristic strength and Weibull modulus were σ_0 ~1110 MPa and m ~28, σ_0 ~1060 MPa and m ~26, and σ_0 ~880 MPa and m ~10 for the 0.7 µm, 1.3 µm, and 1.8 µm film stack, respectively and σ_0 ~ 1820 MPa and m ~3 for the substrate as reference. The effect of PZT thickness on crack initiation was investigated in samples pre-loaded below the stack failure strength. The crack initiation stress of PZT films depends on the thickness of the PZT layer as supported by a finite fracture mechanics model. Both experimental data and a linear elastic fracture mechanics model demonstrate that additional stress is required for the initial crack in the PZT layer to propagate through the entire stack. These results help predict stress limits for PZT thin films under pure mechanical loading and provide insight into operational limits for PZT films under both electrical and mechanical loading, which will be discussed in **Chapter 6**.

5.1 Introduction

Piezoelectric microelectromechanical systems (piezoMEMS) used in sensors, transducers, actuators, and energy harvesting devices [1,2] contain multilayer stacks composed of active piezoelectric layers and their electrodes, with additional layers for adhesion and support. Materials with high piezoelectric coefficients, such as lead zirconate titanate with a morphotropic phase

boundary composition of $Pb(Zr_{0.52}Ti_{0.48})O_3$ (PZT) [1,2,14] are typically used in order to provide high sensitivity sensors or large displacement actuators. Additionally, thin piezoelectric layers (typically between 0.3 and 3 μm in thickness) [16,43,146], are used to significantly reduce the voltage required to reach target electrical fields, relative to bulk ceramics or single crystals. The thickness of the piezoelectric layer is optimized to enhance the piezoelectric response and functionality of the device. For example, thinner films are used for lower voltage applications, while increasing the thickness of the piezoelectric layer can yield a higher power density for energy harvesting devices, due to the increase in the active volume [16]. In addition, thicker films tend to be less clamped to the substrate, which allows for more domain wall motion and may enhance the piezoelectric response [43,146].

Piezoelectric thin films are typically under significant stress, as discussed in **Chapter 3**. The stresses (residual, mechanical, electrical) affect the film's domain structure and piezoelectric response [15,18,19], and may also affect the loads (electrical [21] or mechanical [44,72,147]) the films can withstand. Failure of piezoMEMS stacks typically results from the electromechanical loading conditions [21,148–150], and has been observed to result in a series of thermal breakdown events connected through cracks [21,147,148,150,151]. Determining the mechanical limits of these films is therefore of interest.

Many studies have investigated the mechanical limits of thin films and suggest that the thickness of the piezoelectric layer may affect the structural integrity of the entire stack; stacks with thicker layers are more prone to cracking than stacks with thinner films [21]. Previous studies postulate that the stress required for crack initiation can be a function of thickness either due to a volume effect in Weibullian materials [152,153] or differences in the residual stress as a function of thickness [68,154]. To date, the underlying mechanism for crack initiation in piezoMEMS is

not well understood. Finite fracture mechanics suggest that the thickness affects the conditions for crack initiation in the films. Because crack initiation is contingent on the strain energy accumulated in the film during mechanical loading, it is harder to initiate cracks when the layers are thin [155]. In this work, experimental evidence using Weibull statistics as well as fracture mechanics models assesses the influence of the piezoelectric layer thickness on the stresses for crack initiation in the layer and crack propagation through the entire stack.

5.1.1 Weibull Statistics for Failure

Cracking is difficult to predict as microstructure, domain structure [31,84,86,147], orientation, grain size, and surface quality may influence the mechanical response of the brittle film [86,156–159]. Additionally, failure may be due to adhesion between layers, interface properties, and surface condition (e.g. polish, etch, etc.) [157]. Because there may be a large distribution of flaws, a few measurements may not accurately describe the flaw distributions nor determine the failure stress.

To experimentally determine a statistically significant strength of a material, Weibull analysis should be used; this approach is based on the probability $P_f(\sigma)$ that a given stress (σ) is sufficient for failure, as shown in **Equation 5-1** [154,160]

$$P_f(\sigma) = 1 - exp\left(-\left(\frac{\sigma}{\sigma_o}\right)^m\right) \qquad \text{5-1}$$

where m is the Weibull modulus and σ_o is the Weibull strength; the probability of failing at or below this stress is 63%. When a ceramic has a large distribution of flaw sizes, m will be small and the confidence interval for the Weibull strength will be large. Weibull analysis can take a three parameter form: m, σ_o, and σ_u, where below σ_u there is a zero probability of failure [160]. However,

for brittle ceramics, **Equation 5-1** with two Weibull parameters should be used, since there is a finite probability that at an infinitesimally small stress could cause failure [160].

5.1.2   Fracture Mechanics

Fracture mechanics models can predict mechanical failure in a material based on the flaws, geometries, and materials present. Linear elastic fracture mechanics (LEFM) and finite fracture mechanics (FFM) were used in this study; specifically, mode I failure, where the crack propagates perpendicular to the tensile stress direction, was employed.

LEFM models treat a crack as a continuous body that propagates continuously [161–164]. Griffith initially modeled the energy balance in the system by considering changes in the internal energy (elastic stored energy and surface energy) and the work done to the system [162,163,165]. Irwin expanded this to the form in **Equation 5-2**, which describes the critical stress for cracking, σ_c, as being related to the stress intensity factor, K_{Ic} of the material, knowing the geometry factor, Y [164]. In LEFM, only the *elastic energy* of the system is considered; it is presumed that there is a pre-existing crack of radius a.

$$K_{Ic} = Y\sigma_c\sqrt{\pi a}$$ *5-2*

Because of this assumption, LEFM can only be used to describe conditions for crack propagation in samples where an initial microcrack already exists [161,166].

To predict crack initiation, the Griffith-Irwin [162,164] criterion for crack propagation is insufficient; a different approach such as FFM must be considered. FFM states that under applied mechanical stress, a crack initiates having a "finite" length (which in many cases is on the order of some characteristic feature in the microstructure) when certain stress and energy conditions are satisfied [166–169]. FFM utilizes a stress-energy coupled criterion, where a crack originates if two conditions (i.e. stress and energy conditions) are simultaneously fulfilled.

76

The first condition states that the normal tensile stress ($\sigma(a)$) should be larger than the material tensile strength (σ_c) along the entire potential crack path ($\sigma(a) \geq \sigma_c$). This condition cannot be the only condition for crack initiation in a material as the stress field at the edge of a notched flaw would approach infinite and hence would always exceed the strength, causing failure to occur instantaneously [166]. This extreme case does not occur, so this condition alone is insufficient.

The energy condition, similar to Griffith's approach, considers the change in the system's energy, accounting for the work done to the material and the change in the surface energy due to creation of a crack as shown in **Equation 5-3** [166].

$$\frac{-\delta W_p}{\delta S} = G_{inc}(a) \geq G_c \qquad \qquad 5\text{-}3$$

where G_{inc} is the increment of the potential energy for finite crack length increments. The energy condition for crack initiation is satisfied when G_{inc} exceeds G_c, the material's toughness. In the extreme case of $\frac{-\delta W_p}{\delta S} \to 0$ (which corresponds to the case of slow continuous crack growth), G_{inc} would never reach the material's toughness [166]. Therefore, both conditions must be met for cracks to initiate. When both are met, a crack of defined length will initiate. Additionally, since the energy criterion depends on the material's ability to store energy prior to cracking, as the material's thickness decreases, a larger amount of energy is required to create new surfaces.

At some thicknesses, the energy criteria will be larger than the strength criteria. As a result, at small thicknesses the energy criterion determines the crack initiation stress; the magnitude of this stress depends on the film's thickness. This criterion has been used to explain the onset of cracks in thin polymer films on substrates [155,166] or the generation of surface edge cracks in layered ceramics [170]. In both cases, the potential energy during loading increases with the thickness of the layer containing the prospective crack. As a result, for the same loading conditions

and properties, cracks can initiate in thicker layers under smaller applied loads. Both the FFM and LEFM models are used in this thesis to predict crack initiation and the subsequent propagation in PZT thin films.

5.1.3   Overview

This chapter investigates the relationship between PZT film's thickness and the fracture response of the stack under mechanical loading. PZT/LaNiO$_3$/SiO$_2$/Si stacks with different PZT thicknesses were tested in biaxial loading conditions. Strength distributions of the stacks were evaluated using Weibull statistics and compared to SiO$_2$/Si samples as a reference. The effect of PZT thickness on crack initiation was investigated in samples pre-loaded below the stack's failure strength. Models for crack initiation and for crack propagation are derived based on fracture mechanics considerations. This study can be used to set structural limits on achievable strains in piezoMEMS.

5.2   Experimental Procedure:

5.2.1   Sample Preparation and Structural Characterization

Double-side polished 4" Si wafers with a 1 μm thick thermal SiO$_2$ layer on both surfaces were obtained from Nova Electronic Materials. A 150 nm layer of LaNiO$_3$ (LNO) was deposited on one surface using an acetic acid based solution, as described in **Section 3.2.1** [15,103]. This layer acts both as a template for {001} orientation of the perovskite structure and as a bottom electrode. Then, {001} oriented Pb$_{0.99}\square_{0.01}$(Zr$_{0.52}$Ti$_{0.48}$)$_{0.98}$Nb$_{0.02}$O$_3$ films of 0.7 μm, 1.3 μm, and 1.8 μm were grown by chemical solution deposition (CSD) using a 2-methoxyethanol based solution, see **Section 3.2.1** for more details [15,44,105]. **Figure 5-1** shows a schematic of the stack layers. The orientation and phase purity of the films were characterized by a Merlin FeSEM and by XRD using a PANalytical Empyrean with a Cu K$_\alpha$ X-Ray source to calculate the Lotgering

factor. PZT/LaNiO$_3$/SiO$_2$/Si stacks with different PZT thicknesses, i.e. 0.7 μm, 1.3 μm and 1.8 μm, were diced into 12 x 12 mm squares. Reference samples of the Si substrate with a 1 μm SiO$_2$ layer were also tested for comparison.
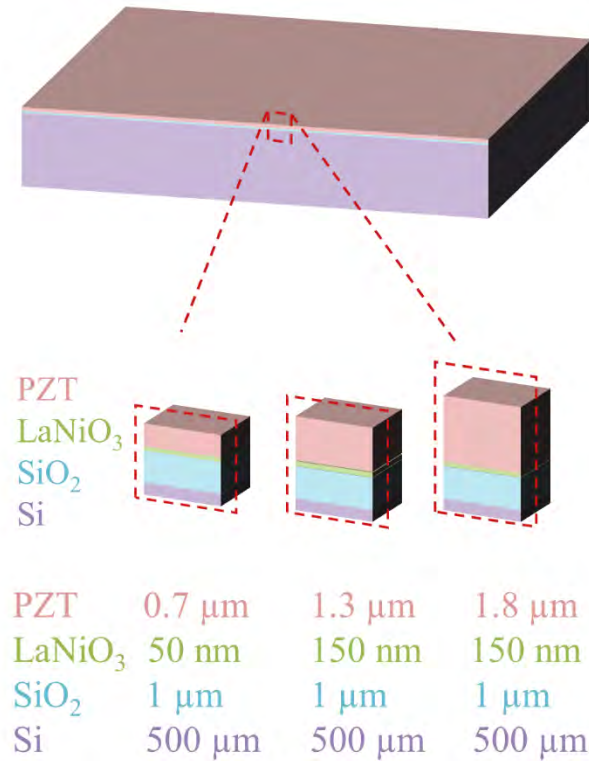
Figure 5-1. Schematic of the samples where PZT of varying thicknesses is grown on top of Si wafer.

5.2.2 Ball on Three Ball Biaxial Test Method

The ball on three balls (B3B) biaxial test method was used to determine (i) the strength distribution of the different samples and (ii) the conditions for crack initiation in the PZT films [171,172]. In this loading configuration, the rectangular plates are symmetrically supported by three balls on one face and loaded by a fourth ball in the center of the opposite face (see **Figure 5-2**); this guarantees well-defined contacts. The four balls had a diameter of 7.5 mm, giving a support diameter of 8.65 mm. At the midpoint of the plate surface, opposite to the loading ball, a biaxial tensile stress is generated. One of the main advantages of this method is that the maximal

stress developed during the test is located far from the edges (corners) of the sample, i.e. away from edge defects [171,173–175]. A total of 20 specimens per sample were tested to failure using a universal tester (Instron, Ma). A pre-load of ~10 N was employed to hold the specimen between the four balls. Tests were conducted under displacement control of 0.1 mm/min in ambient conditions (~22°C and ~40% RH). A Weibull statistical analysis was performed according to ASTM standards [154,160,176].
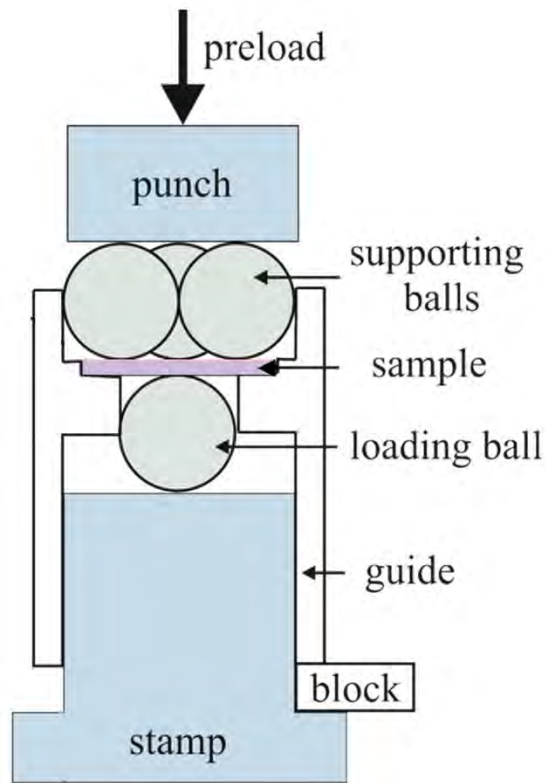
Figure 5-2. Schematic of the Ball on three Ball (B3B) setup.

The stress at the surface under tension was calculated according to **Equation 5-4** [171]:

$$\sigma_f = f * \frac{F}{t^2} \qquad\qquad 5\text{-}4$$

where F is the applied force, t is the thickness of the stack, and f is a geometry factor, which depends on the diameter of the balls, thickness of the sample, and Poisson's ratio, v, of the material.

The factor f was calculated using finite element analysis, resulting in $f = 2.4$ for $t = 0.502$ mm and $v = 0.3$. The failure stress (σ_f) was calculated using **Equation 5-4**, and a homogeneous stress distribution in the sample during B3B was assumed. However, **Equation 5-4** represents the stress for a homogenous material in the ball on three ball test method. Since the stack used in this study is a multilayer stack, where over 99% of the stack is Si, it is assumed that the characteristic strength of the stack is equal to the stress in the top of the Si layer. Si and the various layers have different mechanical properties such as Young's modulus. Since the layers above the Si are very thin and have nearly the same radius of curvature, they have approximately the same strain, but not the same stress as shown in **Equation 5-5**.

$$\varepsilon_{PZT,x} = \varepsilon_{PZT,y} = \varepsilon_{Si,x} = \varepsilon_{Si,y} = \varepsilon_{LNO,x} = \varepsilon_{LNO,y} = (s_{11} + s_{12}) * f * \frac{F_{max}}{t^2} \qquad 5\text{-}5$$

Since the films are clamped to the substrate, it is assumed that the ε_z is close to zero, and so from the strain determined in **Equation 5-5**, the stress in the PZT, LNO, or SiO_2 layers can be calculated using the Poisson's ratio (v) and Young's modulus (Y) of the layer. This is given for the PZT layer in **Equation 5-6**.

$$\sigma_{PZTx,y} = \frac{E}{1-v}\left(\varepsilon_{PZT,x,y}\right) \qquad 5\text{-}6$$

The Young's modulus for {001} PZT is 90 GPa [93] and Poisson's ratio has been estimated to be 0.3.

To investigate crack initiation, selected specimens were loaded between 20% and 80% of the characteristic Weibull stress of the different stacks (loaded in increments of 5%). Each of these samples was only loaded once. The PZT side of the stack was then imaged using an oversaturated dark field optical microscope to assess the presence of cracks. The lowest load at which cracking was observed was recorded as the stress required for crack initiation in the PZT layer. In order to determine the depth of the surface pre-cracks, a FEI Scios Focused Ion Beam (FIB) system was

employed. Cross-sections were made from the top PZT surface down to the SiO$_2$ layer. From these results, crack initiation and propagation models were developed.

5.3   Results

5.3.1   Microstructure

Figure 5-3 shows the FeSEM and XRD patterns for the different samples. All PZT films had strong {100} orientation, with comparable Lotgering factors of 99%, 97% and 99% for the 0.7 μm, 1.3 μm, and 1.8 μm PZT films, respectively. The average surface grain size of the 0.7 μm, 1.3 μm, and 1.8 μm PZT film is 86 ± 7 nm, 105 ± 20 nm, and 106 ± 14 nm, respectively. All of these grain sizes fall within the first standard deviation of each other.
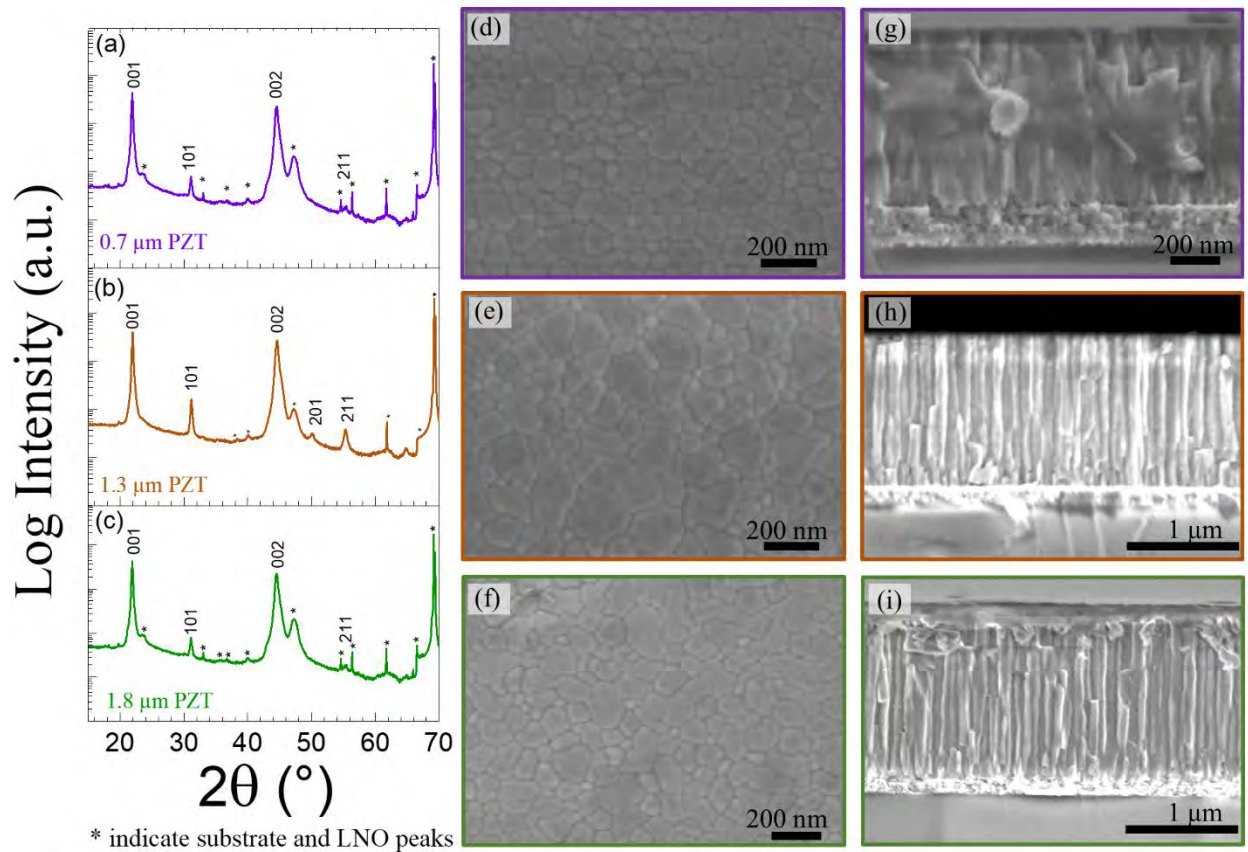
Figure 5-3. XRD pattern of the 0.7 μm PZT (a), 1.3 μm PZT (b), and 1.8 μm PZT on Si (c), where the Lotgering factor is above 0.96 for all samples. The microstructure top view and cross section of the 0.7 μm (d and g respectively), 1.3 μm (e and h respectively), and 1.8 μm PZT sample (f and i respectively). The average grain size (diameter) of the 0.7 μm, 1.3 μm, and 1.8 μm PZT film is 86 ± 7 nm, 105 ± 20 nm, and 106 ± 14 nm, respectively.

82

5.3.2 Strength distribution

Figure 5-4 shows the strength distribution of the different sample sets represented as a Weibull diagram; the corresponding characteristic strength, σ_0, and Weibull moduli, m, are also tabulated in **Table 5-1** along with the 90% confidence intervals. It is apparent that the $SiO_2/Si/SiO_2$ substrates have the highest characteristic strength ($\sigma_0 \sim 1815$ MPa) and the lowest Weibull modulus ($m \sim 3$). Si substrates tend to have a broad population of critical flaw sizes [157–159,174,177,178], which is consistent with the low Weibull modulus observed in this study. The Weibull strength decreases with the addition of the thin $PZT/LaNiO_3$ layers. That is, the PZT layer reduces the strength of the stack [173,174]. It is also apparent that stacks with thinner PZT layers have higher characteristic strength than stacks with thicker PZT layers, i.e. $\sigma_0 \sim 1114$ MPa for the 0.7 μm film, $\sigma_0 \sim 1063$ MPa for the 1.3 μm film, and $\sigma_0 \sim 875$ MPa for the 1.8 μm film. Moreover, the stacks with the PZT layers have higher Weibull moduli than the Si substrate itself, suggesting failure from a narrower distribution of critical flaw sizes in the former.
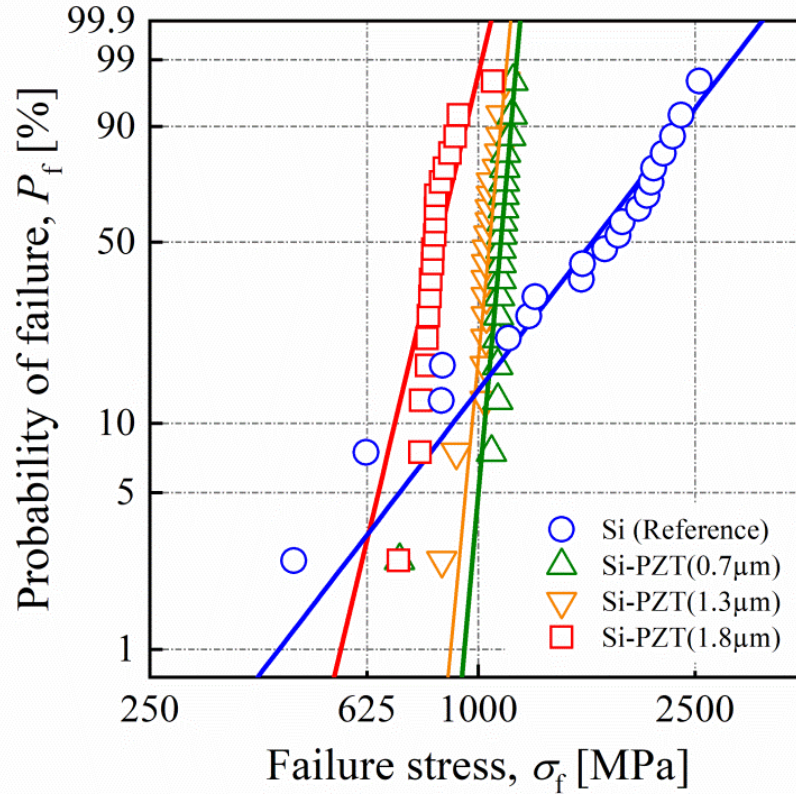
Figure 5-4. The Weibull plot for the following samples: SiO_2/Si (blue circle), 1.8 μm PZT on $LaNiO_3/SiO_2/Si$ (red square), 1.3 μm PZT on $LaNiO_3/SiO_2/Si$ (orange downward triangle), and 0.7 μm PZT on $LaNiO_3/SiO_2/Si$ (green upward triangle). The Weibull strength and Weibull modulus varied with the thickness of the PZT film on the Si wafer.

Table 5-1. Characteristic load, characteristic strength, and Weibull modulus for the PZT/Si stacks of various thicknesses and the Si substrate. All stress values are in MPa and are calculated for the stress in the Si layer upon failure. Brackets represent 90% confidence intervals.

Sample	Characteristic Load, F_0 (N)	Characteristic Strength, σ_0 (MPa)	Weibull Modulus, m (-)
Si (w/ 1 μm SiO₂)	190 [165 – 216]	1815 [1588 – 2081]	3 [2 – 4]
Si- 0.7 μm PZT	116 [114 – 117]	1114 [1097 – 1131]	28 [19 – 35]
Si-1.3 μm PZT	111 [109 – 112]	1063 [1047 – 1082]	26 [18 – 33]
Si- 1.8 μm PZT	92 [87 – 95]	875 [839 – 912]	10 [7 – 13]

5.3.3 Crack initiation

The total force required to crack the PZT layer was (i) 64 N for the 0.7 μm film, (ii) 56 N and higher for the 1.3 μm film, and (iii) 49 N and higher for the 1.8 μm films. **Figure 5-5** shows oversaturated dark field optical images from the center of selected specimens pre-loaded at lower stress levels (between 40% and 80%) than the characteristic strength of the stack. At lower loads (20-40%), cracking was not present. The stress in the stack was determined from **Equation 5-4**, and the stress in the PZT layer (labeled in **Figure 5-5**) was calculated from **Equation 5-6**, with the addition of 150 MPa of tensile residual stress in the PZT [44,93,178], which was measured by the wafer curvature method. The total stress required for crack initiation was 590 ± 29 MPa, 540 ± 29 MPa, and 490 ± 29 MPa, for the 0.7, 1.3, and 1.8 μm films, respectively. The initial cracks did not cause fracture of the entire stack, which was still intact upon unloading. These initial cracks were only visible on the PZT side and were concentrated near the center of the sample, where the maximum tensile stress was applied.
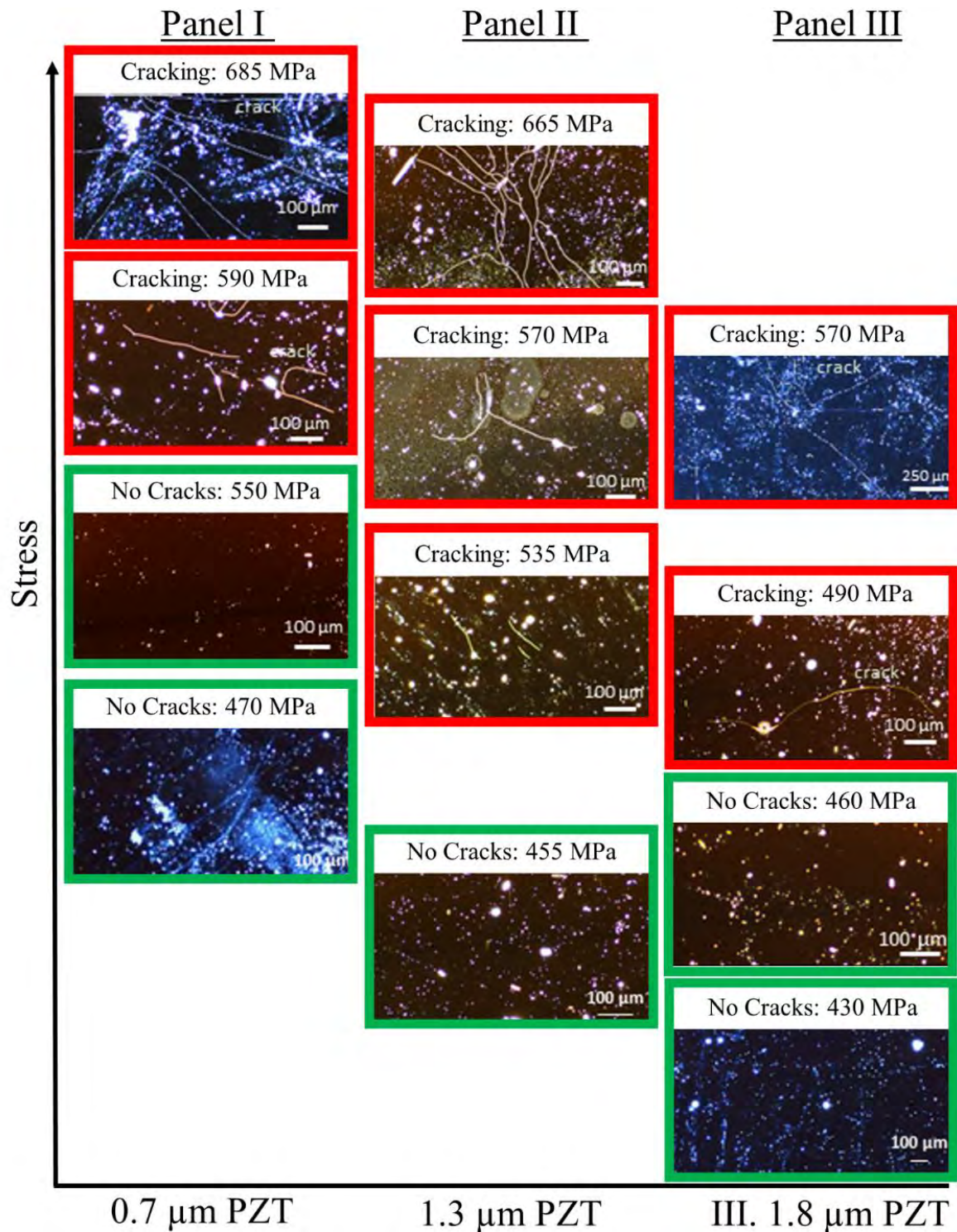
Figure 5-5. Dark field optical microscope images of 0.7 μm film (Panel I), 1.3 μm film (Panel II), and 1.8 μm film (Panel III) loaded between 40% and 80% of the characteristic strength. Initial cracking was observed at loads of 64 N and higher for the 0.7 μm film, 56 N and higher for the 1.3 μm film, 49 N and higher for the 1.8 μm films. This corresponds with approximately 590 MPa, 535 MPa, and 490 MPa of stress in the PZT layer.

5.3.4 Crack propagation

Focused ion beam (FIB) cross sections of pre-loaded samples were used to determine the crack path during the biaxial bending tests. **Figure 5-6** shows a cross section of a crack propagating through the thickness of both the PZT and the LNO layers and arresting in the SiO_2 layer. Although the exact penetration depth of the crack into the SiO_2 layer could not be discerned due to "curtain effects" during FIB cross-section preparation, it is expected that the crack enters the SiO_2 layer and stops, as has been reported in literature for ceramic-ceramic multilayer architectures designed with compressive residual stresses [179].
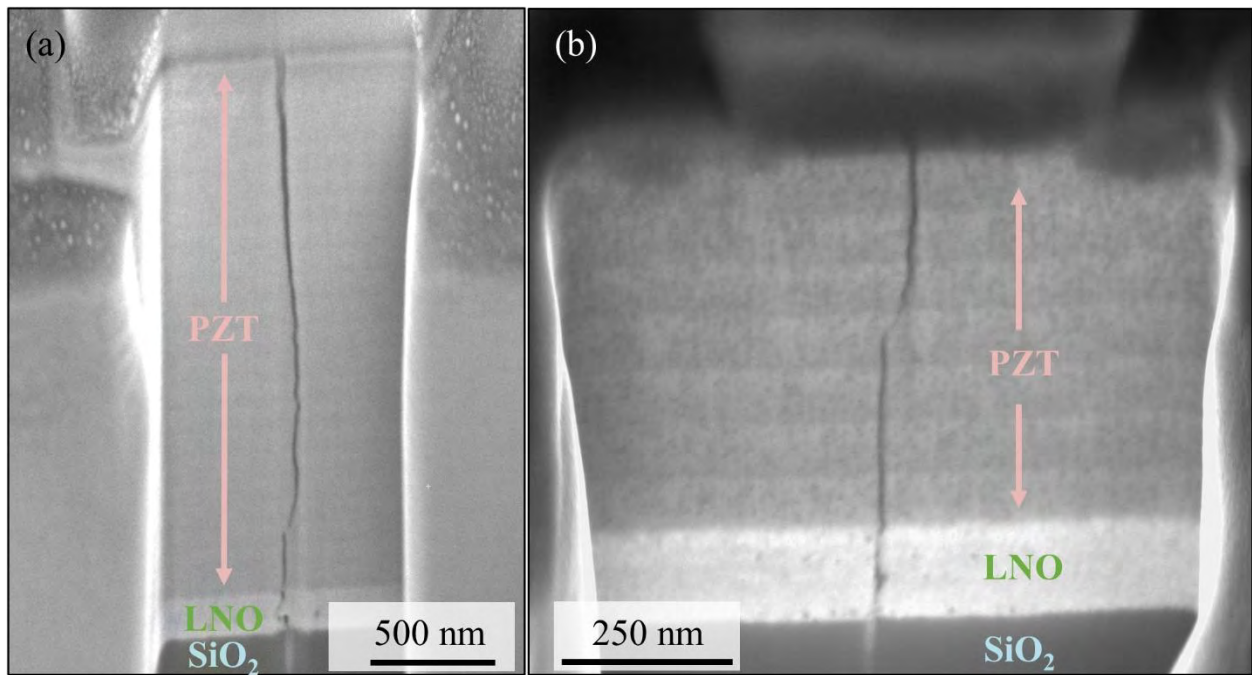
Figure 5-6. FIB cross section of the 1.8 µm PZT film's initial cracking (a) and the 0.7 µm PZT film's initial cracking (b). The crack propagates through the PZT layer and the LNO and ends at the SiO_2 layer. Initial cracks through the PZT and LNO layer were observed on multiple samples of varying stresses and PZT thicknesses. The faint line below the crack at the SiO_2 layer is an artifact of the FIB preparation.

5.4   Discussion

5.4.1   Residual stresses

The stress required to initiate a crack in the PZT/LNO layers depends on the thickness of the PZT film. Thinner films require higher total stresses for crack initiation than either thicker films or bulk PZT ceramics [180]. The experimental residual stress is reported to be constant for PZT films above 350 nm thickness [68], which is consistent with calculations shown in

Table *5-2*. Therefore, it is unlikely that the differences in crack initiation stress between samples can be accounted for by a difference in the residual stress.

Table 5-2. In-plane residual stresses calculated in each of the layers.

Sample	Residual stress in layer (MPa)			
	PZT	LNO	SiO$_2$	Si
0.7 μm	+192	+622	-265	+0.2
1.3 μm	+192	+622	-265	+0.2
1.8 μm	+192	+621	-266	-0.6

5.4.2   Weibull volume effect

Another hypothesis is related to the Weibull volume effect [154]: larger material volumes loaded under the same applied tensile stress have a higher probability of failure than smaller volumes in Weibull materials. That is, the characteristic strength, σ_i, of a sample with volume V_i, can be calculated based on the characteristic strength, σ_o, measured on a reference volume V_o, and the Weibull modulus of the material, m, according to **Equation 5-7** [153,154,160]:

$$\sigma_i = \sigma_o \left(\frac{V_o}{V_i}\right)^{\frac{1}{m}}$$

5-7

In this work, the probability of failure from a critical flaw in samples with thinner PZT films should be lower.

To assess whether the volume dependence may account for the observed thickness dependence in the strength of the PZT samples, **Equation 5-7** was evaluated for different Weibull moduli, ranging from $m=5$ to $m=30$, using the 0.7 μm PZT samples as a reference. **Figure 5-7** illustrates the volume effect on the predicted stress according to **Equation 5-7**. The characteristic strength values for the three samples, i.e. (i) 0.7 μm, (ii) 1.3 μm, and (iii) 1.8 μm PZT film thickness samples are represented in **Figure 5-7** as full symbols. The volume ratio V_0/V_i was set equal to the thickness ratio. According to the results in **Figure 5-7**, the volume effect may explain the differences in crack initiation stresses between two samples, provided that m is approximately five for PZT films. However, based on the homogeneous microstructure of the PZT films and the relatively narrow crack initiation stress values obtained in all three samples, a Weibull modulus larger than 15 is expected [175]; this higher value also corresponds with Weibull modulus for bulk PZT ceramics [181]. This suggests that the volume effect alone cannot explain the differences in crack initiation stress.
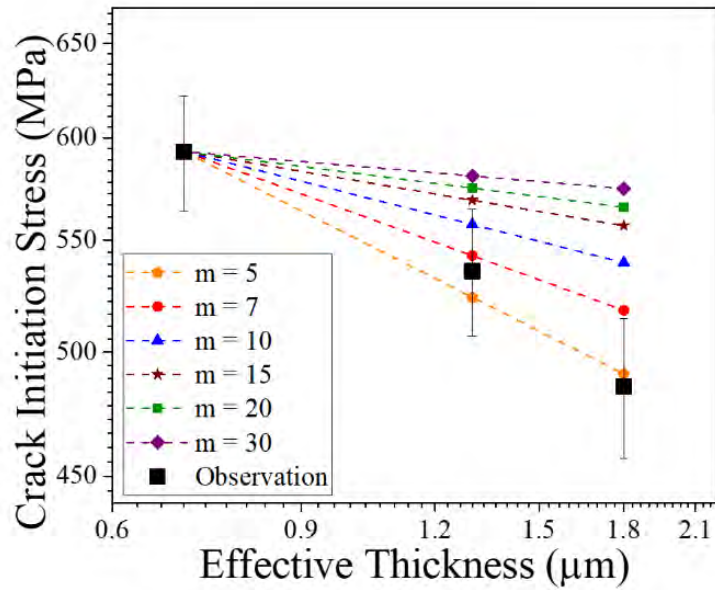
Figure 5-7. Calculated relationship between crack initiation stress and the thickness of the PZT layer using the Weibull volume effect compared to the experimental data. Black squares represent the characteristic crack initiation stress, and the dashed lines are calculated, using the crack initiation stress of the 0.7 μm thick PZT layer as a reference. The various colors represent estimations using different Weibull moduli for PZT for each calculation.

5.4.3   Model for crack initiation: Finite Fracture Mechanics

Alternatively, to model this behavior, a finite fracture mechanics (FFM) model was calculated using K_{Ic} values from 1.0 to 0.6 MPa$\sqrt{m}$. The true K_{Ic} value for PZT varies as a function of domain wall mobility, where the toughness increases with increasing levels of domain wall motion [147,182–185]. Since films are clamped to the substrate and clamping lowers domain wall mobility [183], low K_{Ic} values were used [43,146].

Figure 5-8 represents the calculated crack initiation stress for different PZT thicknesses from 0.6 μm to 2.0 μm and K_{Ic} values of 0.6, 0.8, and 1 MPa$\sqrt{m}$. The full symbols represent the crack initiation stress measured in the pre-loading B3B experiment. Samples with thinner PZT layers require higher stresses to initiate cracks. The calculations for the case of thicker PZT with $K_{Ic} = 0.6$ MPa$\sqrt{m}$ fit well the observed crack initiation stress values from the B3B experiments for thicknesses above 1 μm. However, the stress predicted for the thinner films overestimates the

90

experimental data. The errors in the calculated values are likely to be due to the use of a constant K_{Ic} value. As noted above, the value of K_{Ic} depends on domain wall motion [72,183,185]. Since thicker films generally exhibit more domain wall motion and ferroelastic switching [43,146], K_{Ic} may be a function of thickness [43,183]. As a result, the energy criteria should have a shallower slope at smaller thicknesses, which would better match the observed trend. Neither the correct K_{Ic} nor the level of domain wall motion for these samples is known. More quantitative comparisons would require direct measurements of both K_{Ic} and the ferroelastic switching as a function of the applied stress and the PZT layer thickness. It is worth mentioning that the levels of crack initiation stress (i.e. ~ 500 – 600 MPa) in this study (both predicted and measured) are much higher than the strength of bulk PZT measured in similar biaxial configurations (i.e. ~ 100 – 200 MPa) [181,186]. This shows evidence that FFM is also needed to describe the initiation of cracks in brittle ferroelectric materials, and is particularly important in multilayer systems as the one in this study.
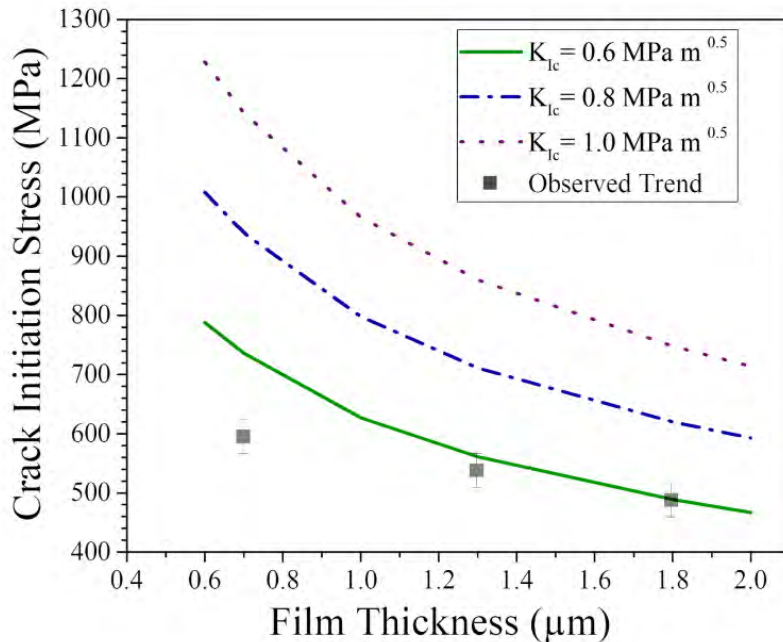
Figure 5-8. Comparison of the strength as a function of thickness for the observed trends (gray squares), and finite fracture mechanics model predictions (K_{Ic}=0.6, K_{Ic}=0.8, and K_{Ic}=1.0, are the green solid line, blue dot-dash line, and purple dotted line, respectively). The observation of this thickness dependence follows the finite fracture mechanics model for thicknesses larger than 1µm, however it fails for very thin films. This may be due to domain wall contributions, which are not taken into account in the model.

5.4.4 Model for crack propagation: Linear Fracture Mechanics

Based on the experimental observations (**Figure 5-5** and **Figure 5-6**), crack initiation in the PZT film is followed by crack propagation and arrest at the SiO_2 layer. This occurs in the 0.7 µm, 1.3 µm, and 1.8 µm PZT film samples. Crack arrest in the SiO_2 may be explained either by a significant change in the crack growth resistance of the material as the crack advances (referred to as R-curve behavior [163]) or due to shielding effects associated with compressive residual stresses in the layer. In this system the R-curve behavior does not apply, because the fracture toughness of SiO_2 does not change with the crack length, and has been reported to be ~ 0.85 MPa√m [159]. The presence of compressive residual stresses however may hinder crack propagation, depending on the magnitude of stress and layer thickness, as has been demonstrated for instance in layered ceramics [179]. The conditions for crack propagation compare the stress intensity factor at the crack tip during loading with the crack growth resistance in the layer where the tip of the crack is located. The stress intensity factor at the crack tip is a function of the crack length, $K_{tip}(a)$, and can be given as the externally applied stress intensity factor $K_{appl}(a)$ plus the contribution of the residual stresses:

$$K_{tip}(a) = K_{appl}(a) + K_{res}(a) \qquad\qquad 5\text{-}8$$

$K_{appl}(a)$ can be calculated according to the Griffith criterion based on LEFM, where [162,164]:

$$K_{appl}(a) = \sigma_{appl} Y \sqrt{a} \qquad\qquad 5\text{-}9$$

with σ_{appl} being the stress applied during loading. The term $K_{res}(a)$ represents the residual stress intensity factor as a function of the position of the crack tip within the corresponding layer in the stack. In order to account for the contribution of residual stresses through the multilayer stack, a weight function analysis was employed [179]. The weighting function is related to the crack

geometry (e.g. through-thickness crack, wedged crack, etc.) and loading condition (e.g. three-point or four-point bending) [187]. In this analysis, the residual stresses profile in each layer is "weighted" along the corresponding layer thickness. The differences in elastic constants between layers are not considered in the analysis. However, when the elastic mismatch between the layers is less than a factor of 10, the change in the stress intensity factor estimation is negligible [188]. Solving **Equation 5-8** for K_{appl}, the Griffith/Irwin criterion described in **Equation 5-9** and **Equation 5-2** becomes:

$$K_{appl(a)} \geq K_{Ic(a)} - K_{res(a)} = K_{R(a)} \qquad\qquad 5\text{-}10$$

where $K_R(a)$ is defined as the "apparent fracture toughness" of the layered ceramic.

Figure 5-9 represents K_R for the three designs as a function of the crack length parameter $Y(a)^{1/2}$ (defined to simplify the analysis), with Y being the geometric factor that accounts for the crack shape and loading configuration. The material parameters including the mechanical properties and thermal expansion coefficients of the various layers for the estimated residual stresses in each layer and the calculation of K_{res} are listed in **Table 5-3** [18,93,96,112,114,189,190]. In this case, Y can be taken as for a central penny-shaped crack at the surface (i.e. $Y = 2 / \sqrt{\pi} \approx 1.12$) [165]. The applied stress intensity factor, $K_{appl}(a)$, is represented in **Figure 5-9** as dashed line. According to **Equation 5-9,** the slope of those dashed lines represents the applied stress, σ_{appl}. This analysis has been performed for a symmetric stack, thus neglecting the slight bending due to the asymmetric architecture.

It is clear that the crack growth resistance decreases as the crack enters in the PZT layer. This is a consequence of the in-plane tensile stress in that layer; the same situation applies for the LNO layer (**Table 5-2** and **Table 5-3**). However, due to the compressive residual stress in the SiO_2 layer, a rising crack growth resistance is observed, thus shielding the propagation of the crack.

93

This "R-curve behavior" is similar in the three architectures; however, the anti-shielding effect of the first layer is related to the PZT film thickness. As a consequence, the minimum stress necessary to propagate the crack through the stack is higher for the 0.7 μm thick PZT layer than in the others. This agrees with the B3B experimental measurements.
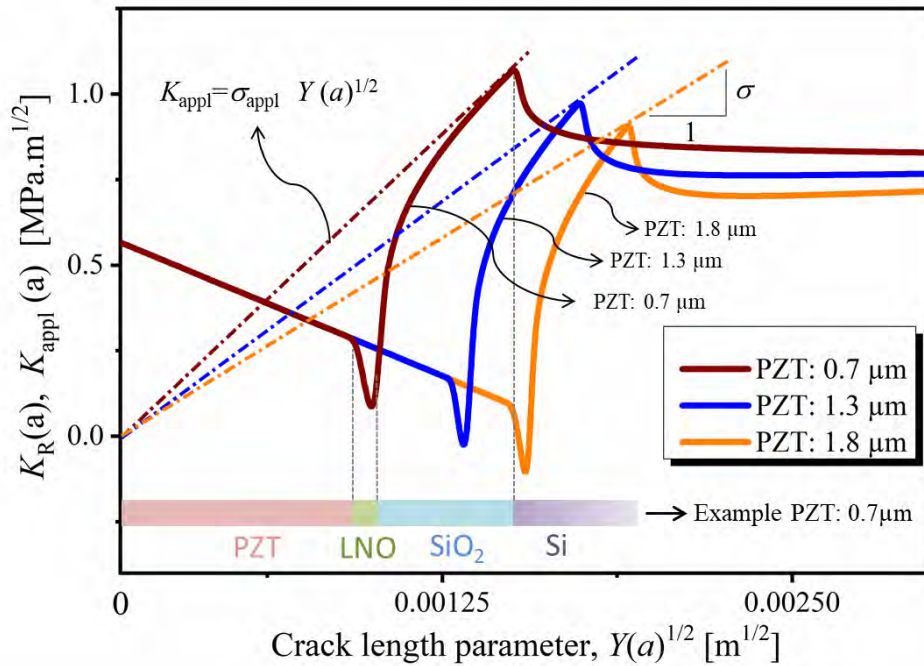
Figure 5-9. Apparent toughness of the multilayer stack as a function of the crack length, the residual stress, and thickness of the PZT layers.

Table 5-3. Reported mechanical properties and averaged thermal expansion coefficients of the various layers in the stack [18,93,96,112,114,189,190].

Material Layer	PZT (001)	LNO	SiO$_2$	Si
Young's modulus (GPa)	90	100[i]	130	180 [ii]
Poisson's ratio (-)	0.3	0.3	0.3	0.3
Averaged Coefficient Thermal Expansion (1/K x10^{-6})	4.8	9.0	0.5	2.6

[i]Due to the porosity of the LNO layer the Young's modulus is lower than the theoretical value [190]
[ii]The biaxial modulus (M) for a single crystal of (001) Si is used.

This investigation demonstrates that stack failure occurs in two stages. A relatively modest stress (~500 – 600 MPa) cracks the PZT and LNO layers [147]. The initial crack acts as a critical

flaw for the failure of the SiO$_2$/Si substrate. As the initial cracks are of consistent length (the sum of the PZT and LNO thicknesses) and the fracture toughness of SiO$_2$ is constant, the stack fails at a consistent stress level for a given PZT thickness. This, in turn, produces the higher Weibull modulus of the PZT stack relative to the SiO$_2$/Si substrate itself. This model also accounts for the observation that the Weibull characteristic strength drops as the PZT thickness increases. That is, thinner PZT layers display shorter initial crack lengths and require higher stresses to propagate the crack through the SiO$_2$ layer.

5.5   *Conclusions*

The thickness of PZT films employed in piezoMEMS has a significant influence on the crack onset and fracture resistance of the entire stack. Biaxial strength measurements on stacks containing different PZT layers grown on ~500 µm Si substrates showed a decrease in the characteristic strength, σ_0, with the PZT layer thickness, ranging from $\sigma_0 \sim 1110$ MPa for 0.7 µm thin film stacks, to $\sigma_0 \sim 1060$ MPa for the 1.3 µm thin film stack, and $\sigma_0 \sim 880$ MPa for the 1.8 µm film stack. These values were significantly lower than the strength of the Si substrate, i.e. $\sigma_0 \sim 1820$ MPa. The higher Weibull modulus obtained in the PZT/Si stacks (i.e. $m \sim 28$ for the 0.7 µm thin film stack, $m \sim 26$ for the 1.3 µm thin film stack, and $m \sim 10$ for the 1.8 µm film stack) compared to Si substrate (i.e. $m \sim 3$) suggests that the PZT/LNO layer thickness becomes the critical flaw size for failure of the entire stack. A stress-energy criterion based on FFM was employed to explain the higher applied load necessary to initiate cracks in the stack containing a thinner PZT layer. Biaxial tests to pre-crack the stacks showed the same trend as the model. This coupled criterion for crack initiation may be extended to complex ferroic materials, if the domain responses are taken into account. Indeed, this could ultimately become a method to quantitatively understand domain wall mobility in ferroic structures under stress. In addition, observation of

crack arrest within the multilayer structure prior to the fracture of the entire stack suggests the possibility of tailoring the internal architecture of piezoMEMS to enhance mechanical integrity and thus performance.

Chapter 6.   <u>**Effect of Electromechanical Loads on Failure Limits of PZT thin Films**</u>

Portions of this chapter have been reproduced from:

K. Coleman, J. Walker, W. Zhu, S.W. Ko, P. Mardilovich, and S. Trolier-McKinstry "Failure mechanisms of lead zirconate titanate thin films during electromechanical loading" in prep

M. Ritter, K. Coleman, R. Bermejo, and S. Trolier-McKinstry "Mechanical Failure Dependence on the Electrical History of Lead Zirconate Titanate Thin Films" submitted (2020)

This chapter evaluates the effects of electromechanical loading and electrical history of a lead zirconate titanate (PZT) layer on the failure behavior. First, 0.6 µm PZT films with different in-plane stress states were failed electromechanically, and the failure patterns revealed that thermal breakdown events and cracks were connected, suggesting coupling between electrical and mechanical failure. Additionally, cracking was observed at 480 ± 50 MPa, which is lower than the reported crack initiation stress for films with similar thickness (590 ± 29 MPa) in **Chapter 5**. To understand the reduction in crack initiation stress, Ball-on-three Balls (B3B) testing of PZT films with variations in electric history (virgin, poled, and under DC bias samples) was employed. The crack initiation stress depended on the electrical history of the sample and was highest for the virgin samples ($\sigma_0 \sim 485 \pm 30$ MPa). The films under DC bias had their relative permittivity and loss tangent measured *in situ* in the B3B set up. Changes in the permittivity suggests electromechanical loading conditions can destabilize the domain structure.

6.1   Introduction

In many piezoMEMS applications, PZT thin films are subjected to severe electromechanical loading conditions to achieve high power outputs, signal strengths, and device efficiencies. In sensors and energy harvesters, the mechanical strains applied can be large, and for thin film actuators, the applied electric fields are usually much larger than those experienced by

their bulk counterparts [16,191,192]. Electromechanical failure of piezoelectric thin films is thus a common topic of considerable technological and commercial significance.

In order to guarantee high performance of the stack, the structural integrity of the film must also be preserved during electromechanical service conditions. Due to the inherent brittleness of PZT, cracking of the film layers is a common problem, leading to a degradation of the electrical properties of the stack or complete failure [147–149]. Recent studies have shown that failure of the stack *under electrical load* begins with cracking in the PZT films [21,148–150]. Electric field induced cracking is believed to be a result of electrically induced stress (σ_e) in the film, which depends on the piezoelectric response ($e_{31,f}$) and the electrostrictive response shown in **Equation 3-6**. For PZT thin films, it is assumed that since $e_{31,f}$ is much greater than M, the electrostrictive term can be ignored, as shown in **Equation 6-1**.

$$\sigma_p = -e_{31,f} \, E \qquad\qquad (6\text{-}1)$$

Equation 6-1 points out a fundamental dilemma for piezoMEMS engineers; while a larger $e_{31,f}$ is desirable for increased device output and efficiency, a larger $e_{31,f}$ also results in larger σ_p at a given electric field (*E*).

Many initial studies have attempted to quantify the total stresses required for crack initiation and propagation [21,147,150]. For PZT thin films, cracks will initiate between approximately 0.5 and 1 GPa [147], which is considerably larger than for bulk PZT, in which both tensile and bending strength is reach around 50-100 MPa [193,194]. **Chapter 5** explores the crack initiation stresses for PZT films under pure mechanical load and suggests that the crack initiation stress in PZT films depends on the film thickness [138,147]. Thicker films need less stress for failure [138,166] due to an energy criterion, which states the required energy in the system

(potential energy and work on the system) needs to exceed the surface energy required for creating a crack [166].

Missing in the literature is work that quantifies the onset of cracking in either poled or electromechanically loaded PZT thin films. It is well known that under applied electric fields, the domain structure will change, which in turn causes reorientation of the spontaneous strain. Although this effect is more pronounced for piezoelectric ceramics [183–185], small changes in the ferroelastic domain structure have been reported in piezoelectric thin films [44,72]. This chapter investigates how in-plane stresses and electrical history affect the fracture behavior of PZT films, and also explores how mechanical loads can affect the PZT film's permittivity.

6.2 Influence of Uniaxial Strains on Electromechanical Failure

In this section, the failure pattern of electromechanically loaded PZT films under different was explored. The anisotropy in the in-plane stress was created by using the beam bending method (**Section 3.2.4**). The films used in this study were also used in **Chapter 3**. The 0.6 μm thick $Pb_{0.99}(Zr_{0.52}Ti_{0.48})_{0.98}Nb_{0.02}O_3$ films were made through chemical solution deposition on $LaNiO_3/SiO_2/Si$ wafers (Nova Electronics materials, <001> 500 μm Si with 1 μm thermal oxide). The films had a preferred {001} orientation due to the blanket $LaNiO_3$ bottom electrode and seed layers. Further details are given in **Section 3.2.1**.

To drive the films to electromechanical failure, DC electric fields of 500 kV/cm (30 V) were applied while monitoring the leakage current using a Hewlett Packet pA meter. The top electrodes were electrically grounded and the voltage was applied through the bottom electrode. Between 100 and 300 s after the field was applied, the film would fail. The failure was marked by the appearance of black features produced by localized thermal breakdown, accompanied by spikes

in the leakage current and audible electrical arcing between the top and bottom electrodes. Additional films were subjected to both 500 kV/cm fields and applied uniaxial strains (-0.05% to 0.05%). The magnitude of the applied strain was measured using a strain gauge and was varied by changing the force applied to the free end of PZT cantilevers, as described in **Section 3.2.4** [44]. The uniaxial strains were applied down the length of the cantilever (y direction), and the stresses in the x and y direction were calculated.

The observed failure patterns seen on the electrodes of the films changed significantly as a function of this applied uniaxial strain (**Figure 6-1**). The thermal breakdown events were visible as small black dots decorating cracks.
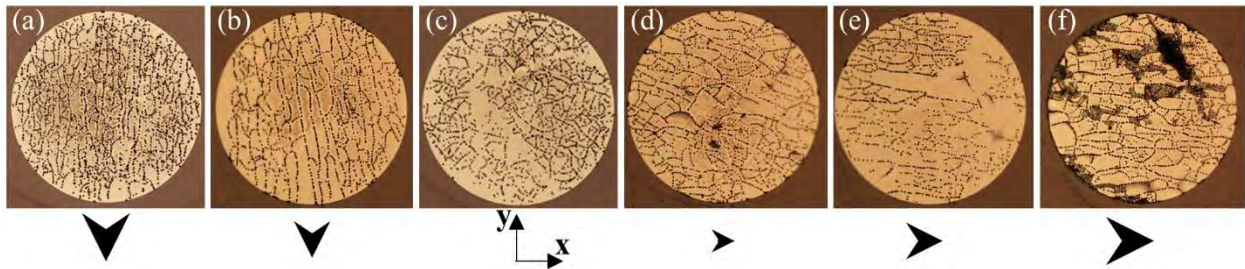
Figure 6-1. Optical images of the failure behavior of 600 μm diameter Pt electrodes on 0.6 μm PZT thin films. The electrodes were under -0.051% (a), -0.036% (b), 0.00% (c), 0.02% (d), 0.03% (e), and 0.051% (f) uniaxial strain in the y direction. The arrows represent the direction perpendicular to the maximum tensile stress direction, which also indicates the cracking direction. The larger arrows represent a larger magnitude of the tensile stress. Thermal breakdown events (black dots) decorate the cracks, giving distinct failure patterns based on the applied uniaxial strains.

The failure pattern of cracks and thermal breakdown events changed with the direction of the uniaxial applied strain. The cracks propagated predominantly perpendicular to the maximum tensile stress direction, as expected. For example, the electrode in **Figure 6-1a** was under a uniaxial compressive strain in the y direction and the maximum tensile stress of 510 ± 50 MPa occurred in the x direction. Therefore, cracks propagate in the y direction. As the uniaxial strain in the y direction was reduced and switched to tensile strains, the crack pattern becomes random (**Figure**

6-1c) and then cracks align with the x direction (**Figure 6-1 d, e, f**). The percentage of cracks that aligned within 45° degrees of the maximum tensile strains' direction were above 80% for all the samples under a uniaxial strain. Thus, even the smaller applied strains induced significant orientation of the cracks.

Inspection of the failed films using scanning electron microscopy (SEM) revealed that the electrical and mechanical failures were correlated in time and space (**Figure 6-2**). Both cracks, indicated by arrows, and thermal breakdown events, seen as oval and circular dark features with lighter outer regions of melted material, are clearly present. The debris on the film surfaces is the residue from thermal breakdown events: molten and solid material expelled violently during breakdown. Thermal breakdown events are connected through cracks and it is likely that cracks appear both before and after thermal breakdown. Some of the cracks propagate through the thermal breakdown events, suggesting that the thermal breakdown events occurred first (yellow dashed arrows). In other regions, the thermal breakdown events and the melt region appear on top of the crack, suggesting that the crack occurred first, as indicated by the orange arrow. The order should depend on when the criteria for each event is met [138,166,195,196]. However, since these two-failure mechanisms are consistently present and the order of events can vary within a single film, it is reasonable to suggest that a single event can cause the other to occur. That is, a thermal breakdown event can initiate cracks by creating sufficient stress and cracks can initiate thermal breakdown events by creating conductive pathways through the film [197].
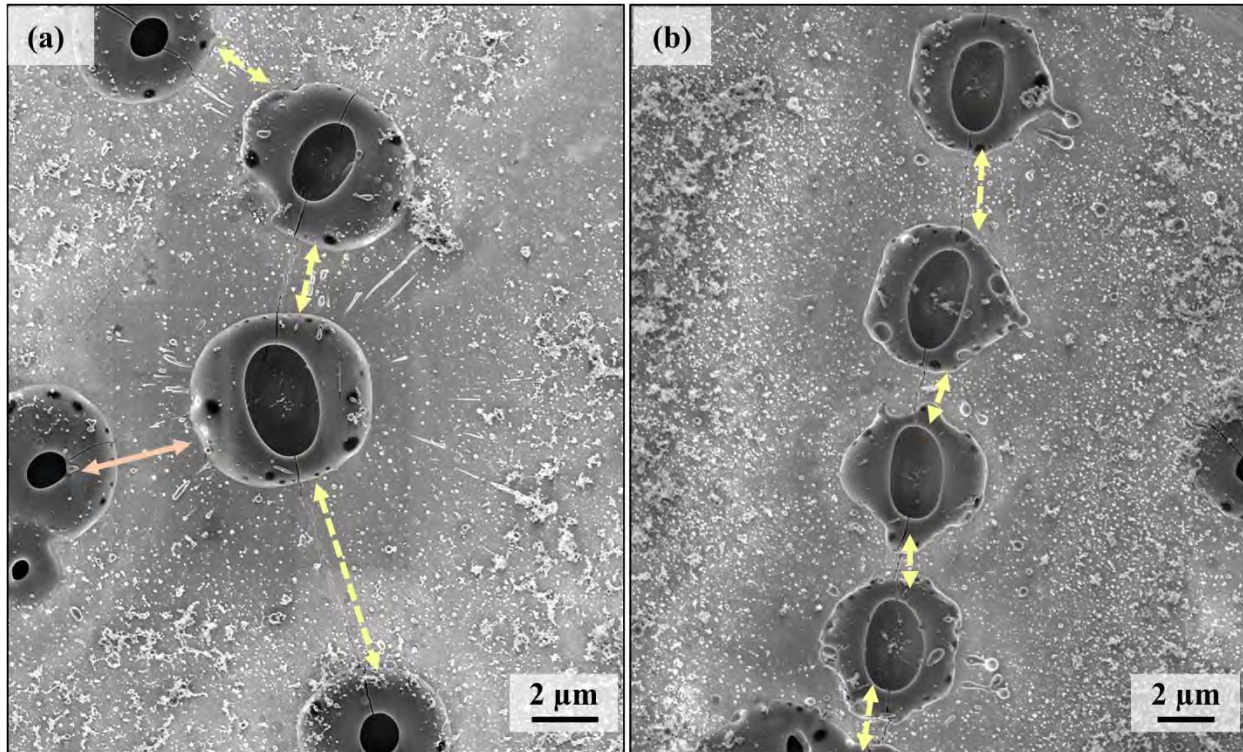
Figure 6-2. SEM of the top surface a failed capacitor, showing both crack and thermal breakdown events for a PZT film under 0% applied strain (a), and -0.05% uniaxial strain (b). Cracks connect the thermal breakdown events as shown by the arrows. The yellow dashed arrows represent cracks that would have occurred after the thermal breakdown events as the crack cuts through the thermal breakdown event. The solid orange arrow represents a crack that occurred before the breakdown events it connects. The crack propagates perpendicular to the maximum tensile stress direction as shown in (b).

To determine the crack initiation criteria for these films, the total stress in the sample was calculated in the in-plane x and y directions, as shown in **Table 6-1**. The total stress included the residual stress σ_r [44], applied stress σ_a, and the piezoelectric stress, σ_p, where $e_{31,f}$ was -7.1 C/m^2 for these PZT films on Si (**Section 3.3)** [44]. With no applied strain and an applied electric field, the PZT samples cracked under a total stress of approximately 480 MPa. **Chapter 5 s**hows crack initiate in 0.7 μm thick PZT film at 590 ± 29 MPa stress when under pure mechanical loads. While the stress to initiate a crack in this film is lower than PZT thin films with similar thickness under pure mechanical loading described in [138], it is similar to values for films under electromechanical loads [198].

Table 6-1. Calculated stresses in the x and y direction for films represented in **Figure 6-2 a-f**. For σ_p, the piezoelectric coefficient, $e_{31,f}$ was estimated to be -7.1±0.35 C/m^2. Numbers in bold indicate the maximum tensile stress for the sample. To calculate the applied stress in the x ($\sigma_{a,x}$) direction the Poisson's ratio of 0.3, and Young's modulus of 90 GPa for (001) oriented PZT was used [93]. Values are in MPa unless otherwise noted.

Electrode	σ_r	σ_p	$\sigma_{a,y}$	$\sigma_{a,x}$	$\sigma_{tot,y}$	$\sigma_{tot,x}$
a	130 ± 30	350 ± 20	-45	14	455	**514**
b	130 ± 30	350 ± 20	-32	10	468	**510**
c	130 ± 30	350 ± 20	0	0	**480**	**480**
d	130 ± 30	350 ± 20	18	-5	**518**	495
e	130 ± 30	350 ± 20	27	-8	**527**	492
f	130 ± 30	350 ± 20	46	-14	**546**	485

The reduction in total stress required for crack initiation may be a result of several factors and was investigated in **Section 6.3**. These factors include the piezoelectric stress, changes in the local stresses with field, and a reduction in domain wall motion. Overall, this initial study reveals that under electromechanical failure, there is a correlation between cracks and thermal breakdown events and the failure pattern depends on the applied strain direction. Cracking would occur when the total stress reaches the crack initiation stress of the film, which was reduced with applied electric fields parallel to the remanent polarization direction.

6.3   Influence of Electrical History on Failure of Lead Zirconate Titanate Thin Films

This section aims to understand how the electrical history of the piezoelectric film affects its performance by investigating property changes and changes in mechanical limits of films with difference electrical histories (virgin, poled, and under DC bias). Dielectric and piezoelectric properties of PZT thin films with various electrical conditions are measured in order to quantify the figures of merit (FoM) for different applications based on the electrical history. The FoMs used in this study are related to the piezoelectric coefficient ($e_{31,f}$) and dielectric

constant (ε_r) of the film; for actuators, the FoM is $e_{31,f}$, for voltage-based sensors, FoM is $\frac{e_{31,f}}{\varepsilon_r}$, and for energy harvesters, FoM is $\frac{e_{31,f}^2}{\varepsilon_r}$ [23–26]. This section employs Ball on three Ball (B3B) testing on PZT films with various electrical history to quantify the effects of electric field on the crack initiation stress and crack propagation in the PZT thin film and PZT/Si stacks. The results are analyzed and compared with the response of similar PZT films under pure mechanical loading.

6.3.1 Experimental Details

6.3.1.1 *Sample preparation and materials characterization*

Niobium doped PZT ($Pb_{0.99}(Zr_{0.52}Ti_{0.48})_{0.98}Nb_{0.02}O_3$) films were grown by chemical solution deposition on a platinized 4-inch Si wafers (NOVA Electronic Materials) as described in **Section 3.2.1.** A total of 20 layers (each layer thickness was ~80 nm) was deposited on the substrate, which yielded a thickness of ~1.6 μm, as measured over an etch step using a contact profilometer (KLA Tencor 16+). The stack has six layers: a 1.6 μm PZT layer, a 100 nm Pt bottom electrode, a 20 nm Ti/TiO$_2$ adhesion layer, 1 μm SiO$_2$ layer, ~500 μm Si substrate, and a 1 μm SiO$_2$ layer. The structure of the stack is shown in **Figure 6-3**. The film's crystallographic orientation was determined using XRD with a PANalytical Empyrean diffractometer with a Cu Kα X-Ray source. The grain size was determined using the line intercept method [199] on several micrographs, taken with a FeSEM.

Pt top electrodes were deposited to a thickness of 100 nm using a Kurt Lesker CMS-18 sputter tool (**Section 3.2.3**). The design of the top electrode (shown in **Figure 6-3**, top right) covers the center of the sample, with a 1 mm diameter circle and a contact pad to the side. This electrode design allows for easy contact during mechanical loading and makes it possible to pole the center

without damaging the surface with a probe tip, which could affect subsequent mechanical measurements.

The wafers were diced into square specimens of 12 x 12 mm^2. Specimens cut from the die were randomly classified into three samples, referred to as virgin, poled, and under DC bias. The virgin specimens did not see any electric fields prior to or during mechanical measurements, and were taken as reference material. The poled samples were heated to 150°C and a DC bias of 13 V (~80 kV/cm) was applied using Hewlett-Packard PA-meter for 15 minutes. Wires were attached to the sample under DC bias using silver epoxy (Ted Pella silver conductive epoxy) to apply the electric field only during the mechanical tests. The exposed part of the wires was covered with insulating epoxy to avoid a short circuit inside the B3B setup.
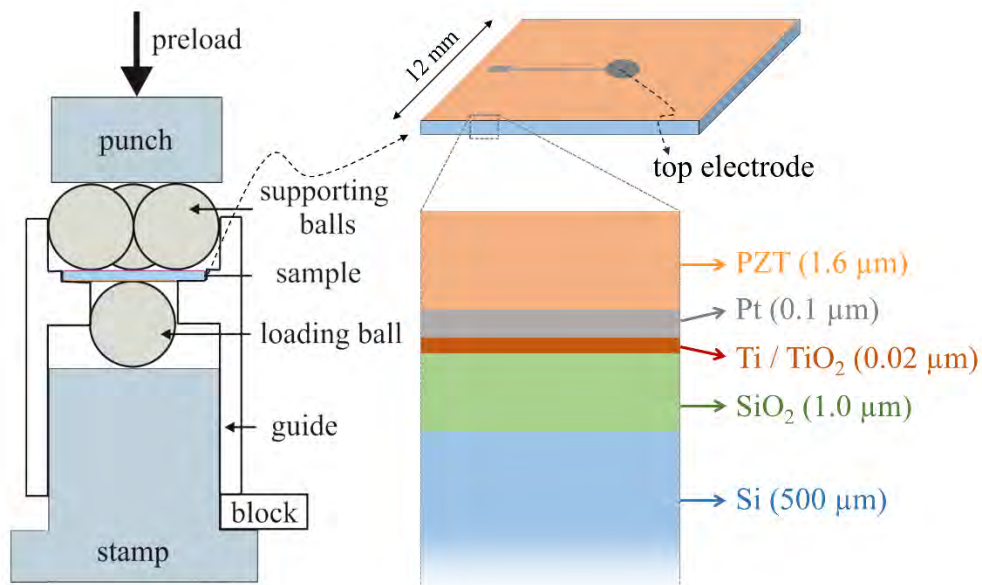
Figure 6-3: The B3B setup, showing the 4 balls and the specimen in the middle, as well as the structure of the samples from the 12 x12 mm^2 specimen. A Pt electrode (gray) is deposited on the PZT top surface (orange layer) to enable contact to the center of the specimen. It consists of a circle with a diameter of 1 mm in the center, a 100 μm wide trace and a 400 μm x 400 μm square close to the edge. A cross section showing each layer in the stack is also depicted (not to scale).

6.3.1.2   Measurement of electrical properties

The film's permittivity and loss were recorded as a function of frequency (100 Hz to 100 kHz) using a Hewlett Packard 4284A precision LCR meter with a small (30 mV) AC signal applied to the bottom electrode. The polarization electrical field (P-E) hysteresis loop was measured at 100 Hz using a Radiant Precision Multiferroic Ferroelectric Tester [44]. Additionally, the Rayleigh behavior of the permittivity was measured up to 35 kV/cm (~ ½ the coercive field, E_c, at 1 kHz). The $e_{31,f}$ was measured using the wafer flexure method described by Wilke *et al.* [200]. All experiments were conducted under ambient conditions (~20°C and ~40-60% RH), and a minimum of three specimens per sample type was used for each measurement.

6.3.1.3   Electromechanical loading: Ball on three ball testing

The relationship between the electric fields and the structural limits of PZT thin films was tested using the B3B biaxial bending test using plate-like test setup [172], as described in **Section 5.2.2**. This leads to a well-defined biaxial stress field, with the highest tensile stresses acting in the middle of the surface, opposite to the one loading ball [201]. Using the B3B set up, the characteristic stack strength of the different samples (loading to failure) and the stress required for crack initiation in the PZT layer (pre-loading and unloading for inspection) were determined.

The strength of the virgin, poled, and under DC bias samples was determined using a minimum of 12 specimens (per sample) tested following the same procedure (preload of about 10 N and a displacement-controlled rate of 0.1 mm/min) using a universal tester (Instron, Ma). The strength of the Pt/Ti/TiO$_2$/SiO$_2$/Si/SiO$_2$ substrate was also measured for comparison. The poled samples were all aged a minimum of 20 hours after poling. The samples under DC bias had 13 V (~80 kV/cm) applied during the mechanical measurements and had no exposure to an electric field prior to measurement. The DC field was applied using a Keysight E4980A precision LCR meter

and the permittivity was also measured during the mechanical testing using the same LCR meter with a 30 mV 1 kHz signal superimposed on the DC bias. The strength of the stack was determined introducing the fracture force, F, into **Equation 5-4**. For this work, since most of the stack thickness is from the Si substrate, it is assumed σ_{max} is the stress in the Si layer. The stresses in each of the layers is calculated as described in **Section 5.2.2** and the supplemental materials in [138].

In order to determine the crack initiation stress, an additional set of five specimens of each sample with distinct electrical history was loaded between 20-70% of the corresponding characteristic load using the B3B setup (see **Section 5.2.2**). The pre-cracks initiated during the loading process were identified using an optical microscope in dark field mode. The force at which cracks were first observed was recorded as the applied force for cracking.

6.3.2   Results and Discussion

6.3.2.1   Structural Characterization

Figure 6-4a shows the microstructure of the PZT layer, with an average lateral grain size of 126 ± 54 nm. **Figure 6-4b** shows the cross section of the sample, in which individually deposited layers can be identified; a small amount of pyrochlore or fluorite grains is apparent at individual crystallization interfaces. The thickness of the PZT films was ~1.6 µm. **Figure 6-5** shows the XRD patterns corresponding to the PZT layer. The film had an approximately random orientation.
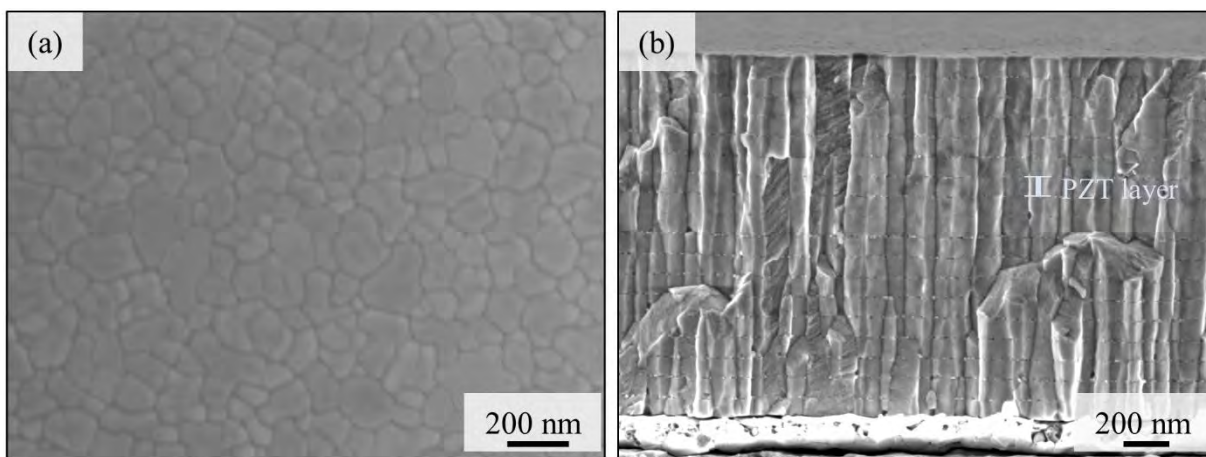
Figure 6-4: *(a*) Top view SEM image showing the grain size of the PZT layer. **(b)** Cross sectional SEM image showing the layered structure of the 1.6 μm thick PZT layer, as well as the platinum bottom electrode.
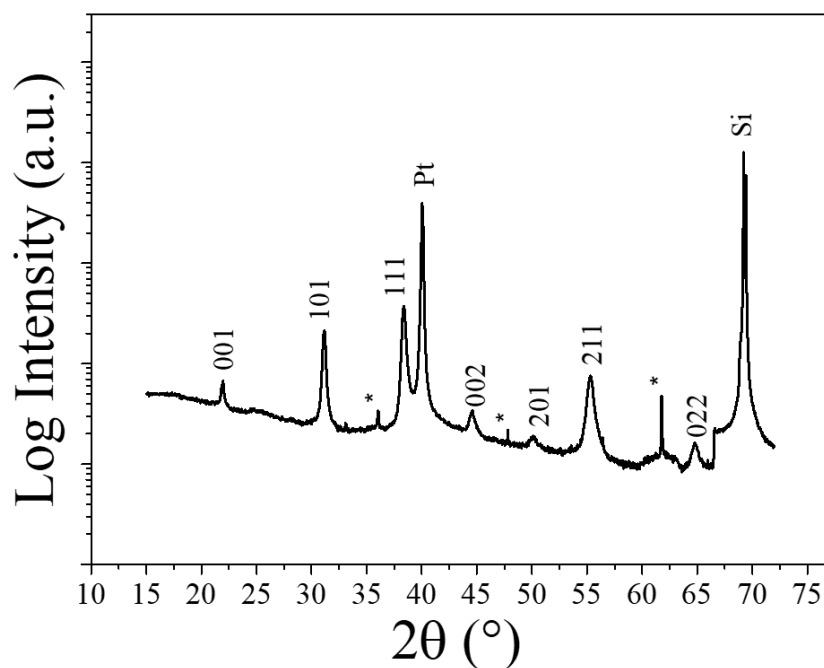
Figure 6-5: XRD pattern of the PZT layer, showing random orientation. The symbol "*" indicates background peaks from the substrate.

6.3.2.2 Electrical Characterization

At 1 kHz under low oscillating electric fields (18.75 V/cm), ε_r was 1100 ± 24, 1073 ± 16, and 740 ± 16 for the virgin, poled, and under DC bias samples, respectively. As the frequency

increased, ε_r decreased slightly for all samples. The relative permittivity was also measured as a function of increasing AC field (**Figure 6-6**). In this low field regime, a linear Rayleigh-like regime was identified using **Equation 2-11**. The irreversible Rayleigh parameter, α_{ray}, captures the irreversible domain wall motion contribution and ε_{init} includes both the reversible domain wall motion and intrinsic contributions to the permittivity. A linear Rayleigh regime for all samples was fitted between 7 and 23 kV/cm (~10-50% of E_c) with R^2 of 0.994 or greater. In the Rayleigh regime, ε_{init} was 1099 ± 17, 1059 ± 17, 735 ± 17 for the virgin, poled, and film under DC bias, respectively. α was 22 ± 2, 15.75 ± 1.25, 5.5 ± 0.14 cm/kV for the virgin, poled, and film under DC bias, respectively.
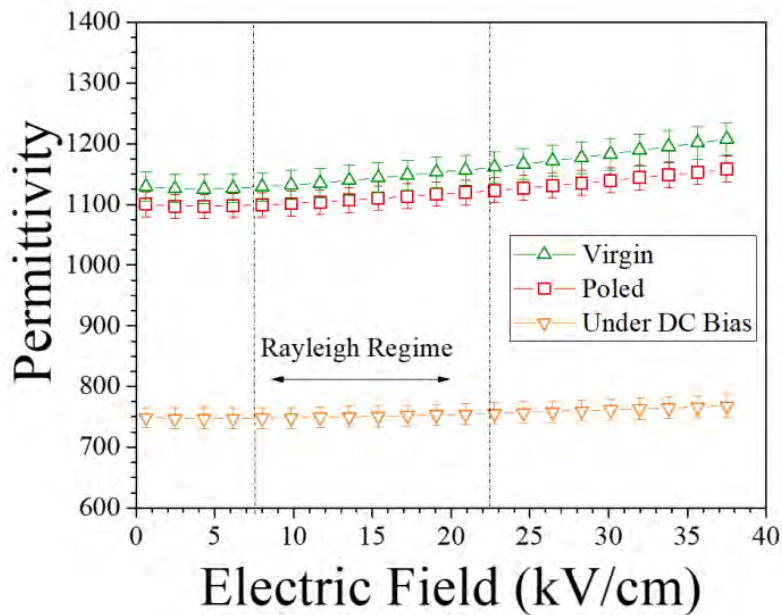
Figure 6-6: Relative permittivity as a function of AC signal for the virgin (green upward triangle), poled (red square), and under DC bias (orange downward triangle) films. The linear Rayleigh regime is denoted between the two vertical dashed lines and was consistent for all the films.

The low ε_{init} for the sample under DC bias is due to dielectric stiffening. The difference between ε_{init} for the virgin and poled sample was modest, suggesting that there is a limited

ferroelastic reorientation with an applied field. As expected, the sample under DC bias has the lowest α_{ray}, which is due to the stabilization of the domain structure [42]. The observation that $\alpha_{ray,virgin} > \alpha_{ray,poled}$ is believed to be due to the removal of domain walls as a result of poling the sample.

The polarization versus electric field hysteresis loops (**Figure 6-7**), shows the changes in the polarization with applied fields. The positive remanent polarization (P_r) was $16.7 \pm 0.2\ \mu C/cm^2$, $18.5 \pm 0.2\ \mu C/cm^2$, $17.7 \pm 0.1\ \mu C/cm^2$ for the virgin, poled, and under DC bias film, respectively. The virgin film's negative P_r was $-19.2\ \mu C/cm^2$ and this slight imprint was removed by applying an electric field as shown by the symmetric loop for the poled and under DC bias films.
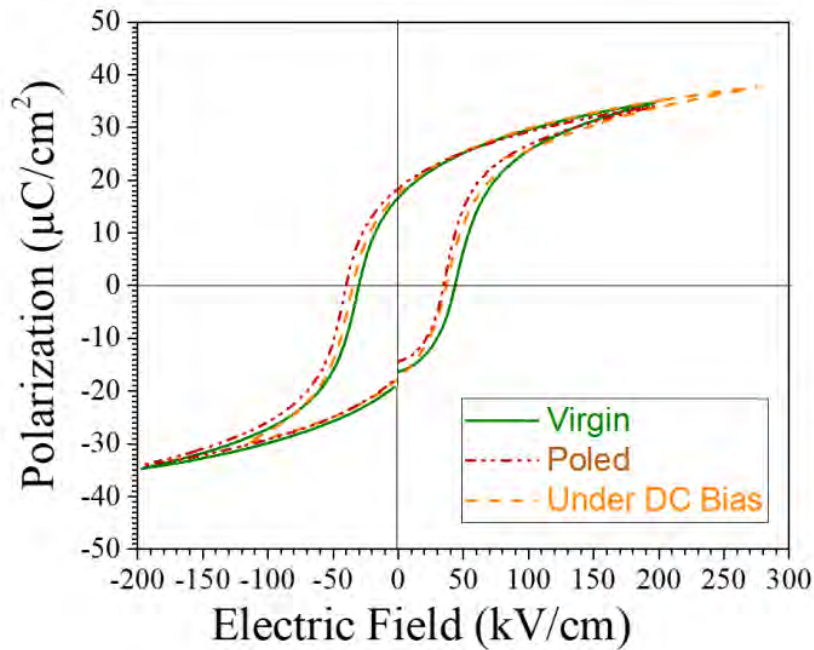
Figure 6-7: Polarization electric field hysteresis (PE loops) for the virgin (green solid lines), poled (red dotted line), and under DC bias (orange dashed line) samples.

The changes in α, P_r, and E_c suggests changes in the domains structure and domain alignment. A schematic illustration of possible domain structures for the different samples is given

in **Figure 6-8**. As indicated by the largest P_r, the poled sample should have more domains aligned with the applied electric field compared to the virgin sample. The sample under DC bias is also expected to have more domains aligned and fewer domain walls than the virgin sample. However, this alignment is incomplete since the film under DC bias is only under electric field during the measurement.
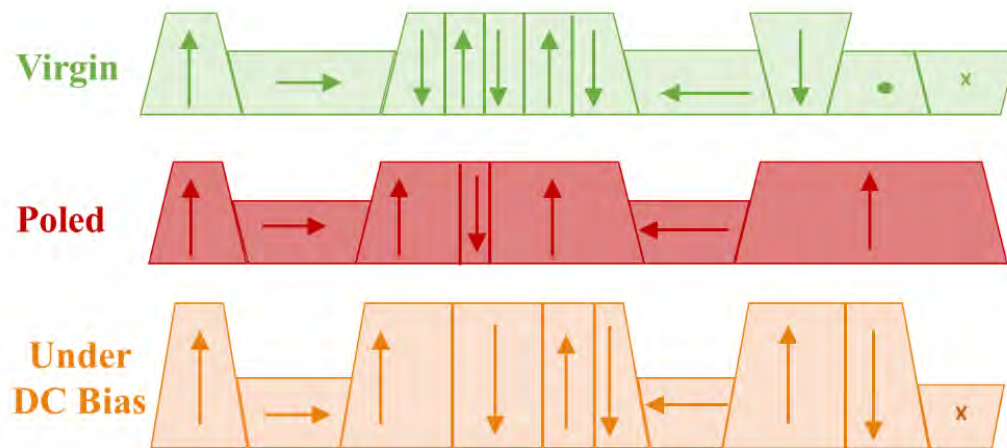
Figure 6-8: Schematic illustration of the domain structure for the virgin (green), poled (red) and under DC bias (orange) sample. Arrows represent the polarization direction for the respective domains.

Due to the differences in domain structure, the films have different piezoelectric coefficients and FoM. The various FoM are shown in Table *6-2*. Table of the calculated figure of merits (FoM) for the various applications for sensors, actuators and energy harvesting devices. **Table 6-2**, where the piezoelectric coefficient, $e_{31,f,}$ was measured to be 0 C/m^2, -6.5 ± 0.6 C/m^2 and -4.1 ± 0.3 C/m^2 for the virgin, poled, and under DC bias sample, respectively. The poled sample has the largest coefficient, presumably because the sample under DC bias was only partially poled. The poled sample also had the highest FoM for all applications compared to the virgin and the sample under a DC bias. An additional sample that was poled, aged for 24 hrs., and then measured under a DC bias is also reported in **Table 6-2**. The piezoelectric coefficient was slightly lower than the poled

sample due to aging, and the permittivity was also lower because of the DC bias. As a result, it had the largest FoM for sensors and energy harvesters.

Table 6-2. Table of the calculated figure of merits (FoM) for the various applications for sensors, actuators and energy harvesting devices.

FoM / Sample state	Sensors $\frac{|e_{31,f}|}{\varepsilon_r}\left(\frac{C}{m^2}\right)$	Actuators $e_{31,f}\left(\frac{C}{m^2}\right)$	Energy Harvesters $\sim\frac{e_{31,f}^2}{\varepsilon_r}\left(\frac{C}{m^4}\right)$
Virgin	0	0	0
Poled	6.0×10^{-3}	-6.5	3.9×10^{-2}
Under DC Bias	5.5×10^{-3}	-4.1	2.3×10^{-2}
Poled and under DC Bias	9.1×10^{-3}	-6.8	6.2×10^{-2}

6.3.2.3   Strength distributions and fracture analyses

Figure 6-9 shows the probability of failure, P_f, versus the failure stress, σ_f, in a Weibull diagram for the virgin, poled, and under DC bias samples, as well as for the Pt/Si substrate. The Weibull parameters (i.e. characteristic strength, σ_0, and Weibull modulus, m) were calculated according to the ENV-845 standards [202] and are given in **Table 6-3**, along with the 90% confidence intervals. The Weibull modulus ranged between $m = 26$ and $m = 30$ for the virgin, poled, and under DC bias sample, where the substrate's modulus was ~3. There was no significant difference in the characteristic stack strength between virgin, poled, and under DC bias samples.
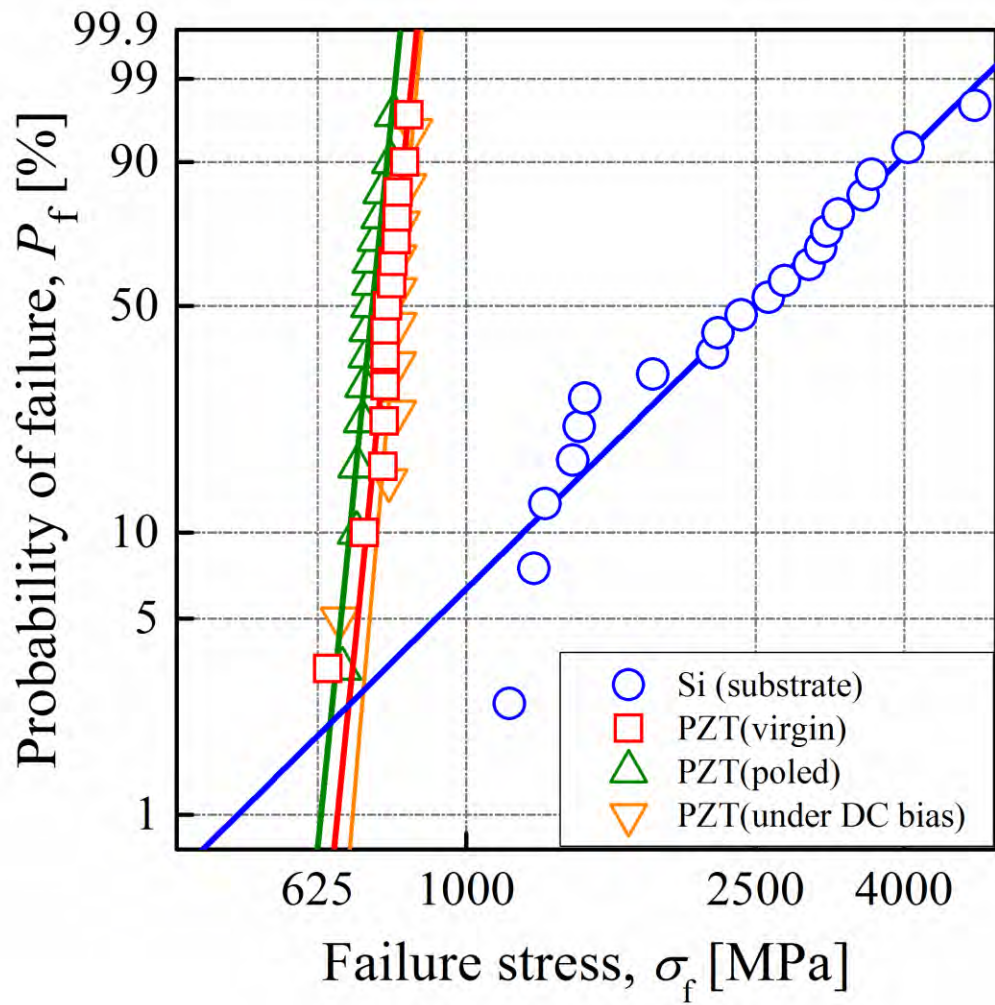
Figure 6-9: Probability of failure versus failure stress in a Weibull diagram for the three samples: virgin (green upward triangle), poled (red square) and under DC bias (orange downward triangle) and the Pt/Si sample (blue circles), as a reference.

Table 6-3: Weibull modulus, m, and characteristic strength, σ_0, for failure of the difference sample stacks. Values in [] represent the 90% confidence interval.

Sample state	Weibull modulus m [-]	Characteristic strength σ_0 [MPa]
Virgin	26 [17-34]	795 [780-811]
Poled	26 [17-34]	754 [739-769]
Under DC bias	30 [16-40]	815 [797-833]
Si	2.6 [1.8 – 3.3]	2851 [2428 – 3356]

At lower loads, cracks were visible on the surface of the PZT film; this initial crack did not propagate through the entire stack. A focused ion beam etch was used to determine the initial crack length, as shown in **Figure 6-10**. The crack propagated through the PZT layer, and stopped at the Pt layer. Pt, being metallic, may prevent crack propagation through plastic deformation. Similar to results in **Section 5.4.4**, cracking occurs first in the PZT layer, followed by crack propagation through the subsequent layers. The initial crack in the PZT layer acts as the critical flaw for the failure of the remaining layers in the stack. This yields higher Weibull moduli of the PZT stacks as compared to the substrate, and is similar to the results in **Section 5.4.4** [138].
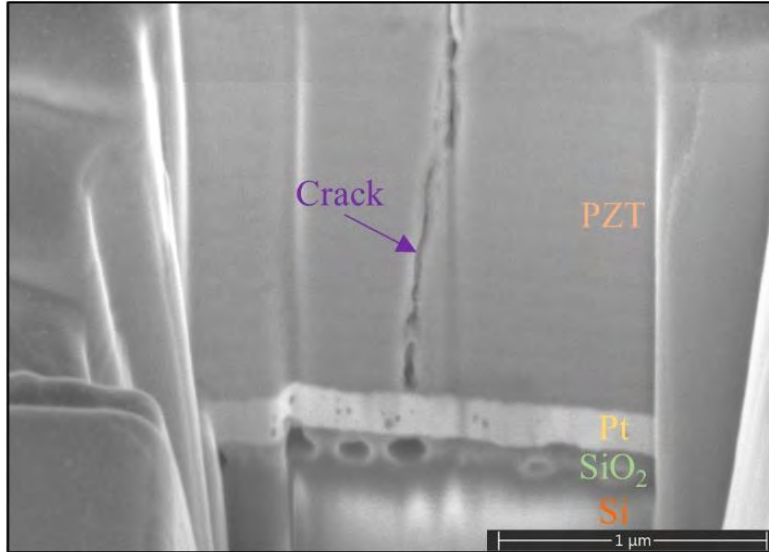
Figure 6-10: FIB image showing the crack stop at the interface of the PZT and Pt seed layer beneath. The image was prepared using a FEI Scios Focused Ion Beam (FIB) system. The porosity in the SiO_2 layer may be due to lead diffusion through the stack, and some damage from the FIB.

The stress to initiate a crack in the PZT layer depended on the electrical history as shown in **Table 6-4**. The virgin sample had cracks initiate at stresses around 500 MPa. Although the film has a random orientation and some pyrochlore present, this stress to initiate a crack is similar to the predicted crack initiation stress range for PZT films with similar thicknesses (1.8 μm) reported in **Section 5.3.3** [138,147]. However, crack initiation occurred at lower stresses for both the poled sample, and the sample measured under DC bias (around 400 MPa). Initially, this difference was attributed to inaccuracies in the calculated piezoelectric stress. It was assumed that the $e_{31,f}$ did not change with applied mechanical load or time, but other reports suggest that the piezoelectric coefficient will change with both field and stress [44,100]. However, this does not account for the decrease in crack initiation stress for the poled sample, since it was not under an applied electric field during B3B loading and there is a statistically significant decrease in the crack initiation stress compared to the virgin sample.

Table 6-4. Calculated stresses (applied, piezoelectric, and residual stresses) in the PZT films and total stress for crack initiation for each film based on its electric history. There is an additional systematic error of the residual stress and crack initiation stress of ± 30 MPa.

Sample	Force Cracking observed [N]	Applied Stress in the PZT layer [MPa]	Residual Stresses [MPa]	Piezoelectric Stress [MPa]	Total Stress for Crack Initiation [MPa]
Virgin	49 ± 3.8[δ]	335 ± 26	150	0	485 ± 26
Poled	37.5 ± 3.8	260 ± 26	150	0	410 ± 26
Under DC bias	35.2 ± 3.8	240 ± 26	150	33 ± 3	430 ± 29

[δ] The error corresponds to the interval of applied forces between no-cracking and cracking observation on each sample.

There are a few hypotheses for the observed reduction in the film's crack initiation stress with applied fields. First, there may be some differences in the domain wall motion between the films. The irreversible Rayleigh coefficient was largest for the virgin sample. Non-180° domain wall motion and ferroelastic domain reorientation have been shown to enhance the fracture resistance [184,185]. If domains are unable to reorient to reduce the applied stress, then PZT would have a lower apparent fracture toughness. However, the reduction in the irreversible Rayleigh coefficient may be due to the large reduction in the number of 180° domain walls, and it is inconclusive if the amount of ferroelastic domain reorientation is also changed during mechanical loading. Alternatively, the creation of local strain during the poling process is also proposed to cause this reduction in crack initiation stress. Under an applied electric field, domains align to the polarization direction, and previous reports suggest limited ferroelastic reorientation occurs in clamped films [46]. Ferroelastic domain reorientation will create localized stresses, and may result in the lower fracture resistance in the poled sample. Both the poled sample and the film under DC bias may experience some ferroelastic domain reorientation. However, it is anticipated that the

poled film may have more domain alignment and may also have slightly more local strains from ferroelastic switching. The extent of ferroelastic domain reorientation is not measured in this study and therefore future work should explore the mechanism governing this trend. Overall, this study suggests that poling and electric fields can reduce the crack initiation stress up to 15% and confirms the failure observation in **Section 6.2**.

6.4   In situ property measurements under electromechanical loads

To further explore the relationship between electromechanical loading and the changes in properties, PZT films under DC bias had their relative permittivity and loss tangent recorded during the B3B loading experiment (**Figure 6-11**). The plots are segmented into three regions (I, II, and III). Region I is the preload region, where the PZT sample is loaded up to 10 N prior to the start of the experiment. Region II begins when the DC bias of 80 kV/cm is applied, the permittivity is recorded, and a downward force on the mechanical fixture is applied at a rate of 0.1 mm/s. During this stage, cracks were not observed on the film's surface, since the stresses are lower than the reported crack initiation stress. Region III corresponds to the forces at which surface cracks are observed.
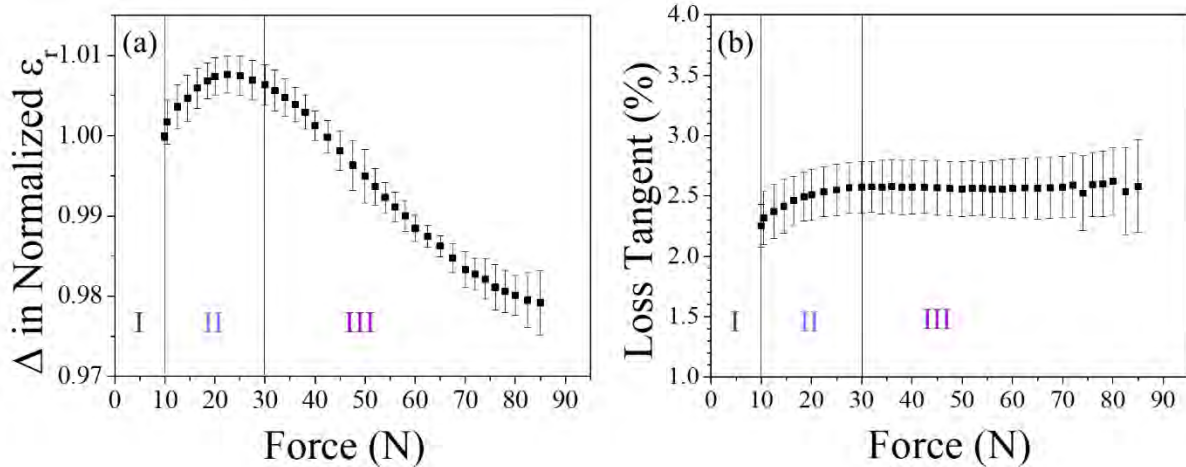
Figure 6-11: Change in normalized relative permittivity (a) and change in loss tangent (b) as a function of the load force during the B3B measurements. The three regions can be allocated to three different conditions, governing the electrical properties of the PZT layer. Region I is the preload region. Region II is the regions before cracks are observed and Regions III is the regions after cracks were observed on the surface. Each of the three lines represent a separate sample tested.

In this electromechanical loading condition, the electric field is out-of-plane, which would favor out-of-plane polarization. However, the mechanical loading would favor more in-plane domains. It is suggested that competition between these two loads on the film may destabilize the domain structure. This would account for the initial increase in the relative permittivity and loss tangent for Region II. Around 20 N in Region II, the permittivity begins to decrease and this continues in Region III, where cracks are formed on the surface. The decrease in the calculated value of permittivity may be due a variety of factors. There may be a reduction in domain wall motion at a certain stress level. This decrease could also be related to the formation of internal cracks, where air would act as a parasitic capacitor layer, reducing the overall capacitance. Alternatively, the effective electrode area may decrease due to delamination, such that the calculated permittivity is underestimated. Lastly, the PZT film may be locally de-clamped as the crack forms, such that domains can align with the electric field out-of-plane. This would lower the overall relative permittivity.

To further probe the effects of mechanical loads on the destabilization of the domain structure, the aging rate of the permittivity was determined after removing the mechanical preload (10 N) on virgin and poled films. **Figure 6-12** shows the normalized change in the permittivity as a function of time after removal of the preload. A linear fit of the permittivity suggests an aging rate of 1.2% per decade for both poled and virgin samples. This is in good agreement with the dielectric aging rates recorded after removal of an electric field [203], suggesting the rate at which the global domain structure approaches equilibrium is independent of a mechanical or electrical load.
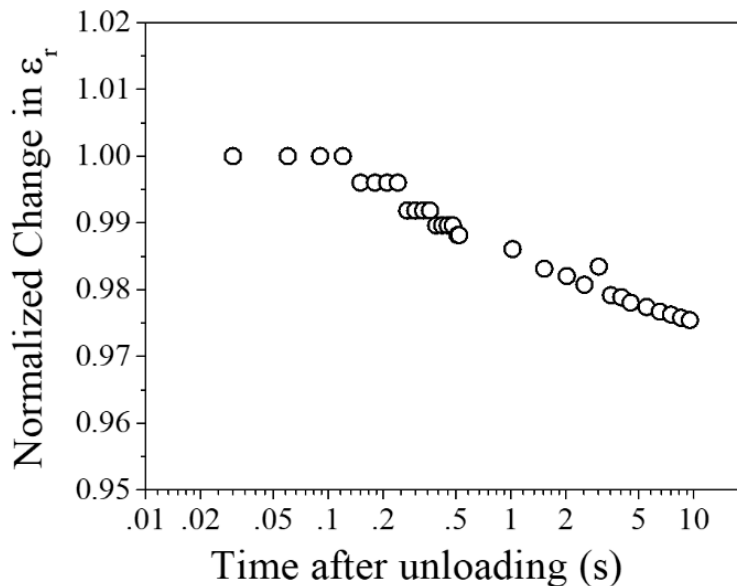
Figure 6-12: Normalized change in the relative permittivity as a function of time (log) to determine the aging rate after the removal of a mechanical load. The dielectric aging rate was 1.2% per decade.

6.5   Conclusions

This chapter explored the effects of electric history, and electromechanical loads on the failure and mechanical limits of PZT thin films. Crack patterns in electromechanically loaded PZT films depend on the directionality of in-plane tensile stresses and cracking is observed at lower

loads than virgin films made on the same wafer. Failure under electromechanical loading conditions was observed as a combination of thermal breakdown events and cracks in films clamped to a Si substrate. Additionally, the electric history of the sample dictates the performance of the films, influences the FoM, and may reduce the crack initiation stress. While poling enhances the piezoelectric response of the film, it reduces the stress that the films can withstand during operation, prior to cracking. While this reduction may be due to a series of factors, this observation was noted for a series of films under different loading conditions. Lastly, the application of electromechanical loads may destabilize the domain structure and the removal of mechanical loads leads to similar dielectric aging rates that are reported after the removal of electrical loads. This suggests that the time for the domain structure to reach a new equilibrium position is independent of the type of load. This chapter emphasizes the necessity to quantify the mechanical loads on piezoelectric films, as they may destabilize the domain structure, and in electromechanical applications, failure may ensue at lower loads than predicted from mechanical-only testing.

Chapter 7.   <u>**Conclusions and Future Work**</u>

7.1   Conclusions

This thesis discusses the influence of mechanical stresses (applied, residual, and piezoelectrically-induced) on the dielectric and piezoelectric properties of PZT thin films. The limits of stress that PZT films could tolerate was found to be a function of film thickness, electrical history, and loading conditions. In particular, thicker films tend to have lower mechanical limits compared to thinner films, and the electric history and the substrate can play a critical role in the applied stress limits of the film. Additionally, compressive stresses were shown to improve piezoelectric properties, increase applied stress limits before failure, and increase the number of out-of-plane domains. Tailoring the residual stress in thin films can tune dielectric and piezoelectric properties, reduce the propensity for cracking, and improve their performance in various piezoMEMS applications.

The effect of total stress on the dielectric and piezoelectric properties of PZT films grown on Ni and Si foils was investigated (**Chapter 3**). PZT films grown on Ni foil experience compressive residual stresses and had larger piezoelectric coefficients ($e_{31,f} = -9.7 \pm 0.45$ C/m^2) and remanent polarizations ($P_r = 39.5 \pm 2.3$ μC/cm^2) compared to PZT films grown on Si wafers ($e_{31,f} = -7 \pm 0.35$ C/m^2, $P_r = 21 \pm 0.2$ μC/cm^2). Due to tensile residual stress, PZT on Si had a larger relative permittivity ($\varepsilon_r = 1040 \pm 20$) than PZT on Ni ($\varepsilon_r = 600 \pm 80$). With additional compressive strains applied to films on either substrate, the remanent polarization and piezoelectric properties increased and the relative permittivity decreased. The opposite occurred under tensile stress, suggesting some ferroelastic domain reorientation could occur in these films. Property changes were approximately linear with stress changes; the slope differed between the two substrates. The slope of the remanent polarization versus stress was -0.013 MPa/(μC/cm^2) and -0.021

MPa/(μC/cm^2) for PZT on Ni and Si, respectively. Within the stress limits, the properties of PZT on Ni and Si did not overlap, indicating that residual stress and the resulting domain structure dictate the range and tunability of both dielectric and piezoelectric properties.

To further probe the relationship between the changes in the properties with stresses in the film, **Chapter 4** revealed differences in the intrinsic and extrinsic contributions to the dielectric and pyroelectric properties. PZT on Ni is under 530 MPa of compressive residual stress and PZT on Si is under 130 MPa of tensile residual stress. The magnitude of residual stress significantly influenced the extrinsic contributions to film properties. Both the Rayleigh and Preisach responses show a large reduction in irreversible property contributions for PZT films on Ni as the temperature decreased towards 0 K. At room temperature, α_{ray} was 15.5 ± 0.1 cm/kV and 28.4 ± 1.6 cm/kV for PZT on Si and Ni, respectively and the large amount of irreversible domain wall motion for PZT on Ni may be due to the flexibility of Ni foil. However, as thermal energy decreased, domain wall motion decreased at a higher rate for PZT on Ni, which may be due to a combination of increased residual stress at lower temperatures and decreased thermal energy. PZT films on Si did not show large changes in residual stress in the films when cooled to 10 K and had a smaller reduction in the irreversible Rayleigh coefficient. This is because PZT and Si have very similar thermal expansion coefficients at lower temperatures. It is believed that these results can be explained by a narrower distribution of pinning potentials for PZT on Ni relative to PZT on Si. Overall, the residual stresses and substrate choice influence the domain structure and the pinning centers causing some films to have less domain wall motion.

Stress limits in PZT thin films were investigated (**Chapter 5**). First, crack initiation stress was studied as a function of film thickness. Thicker films required lower stresses for crack initiation, where 0.7 μm PZT films required stresses around 590 MPa, and 1.8 μm films required

stresses around 490 MPa to initiate a crack. The literature previously attributed this to either changes in the residual stresses of thick films, or the Weibullian volume effect. This work suggests that instead, the coupled stress-energy criterion for crack initiation affects the mechanical limits of these films. This depends on the thickness of the films, where thinner films require a higher load to reach their energy criteria and fail. The slight deviation between the model and experimental observation may be due to differences in domain wall mobility. Thinner films tend to have less domain wall motion and thus, a lower fracture toughness. The current model only considers one value for the fracture toughness as the fracture toughness for PZT thin films has yet to be determined.

This biaxial ball-on-three-ball test method was also used to explore how cracks initiated and propagated through the entire stack. PZT/LaNiO$_3$/SiO$_2$/Si stack failure occurred in two stages. First, the PZT layer cracked; the crack then arrested at the SiO$_2$ layer due to the significant compressive stress in the SiO$_2$. With a higher applied stress, the crack propagated through the remainder of the stack. As shown by the Griffith-Irwin crack resistance model, stacks with thinner PZT films require higher stresses for failure because the initial crack length is shorter. It was also found that the Weibull modulus was significantly larger for PZT on Si ($m \geq 10$) compared to the Si substrate itself ($m = 3$). This occurred because the stack had a consistent pre-crack length corresponding to the PZT film's thickness. To design stacks with increased strength, thin layers under compressive stress should be considered.

In addition to pure mechanical failure, it was found that electromechanical loading could also affect the PZT layer's mechanical limits in **Chapter 6**. This occurs because the applied electric field creates piezoelectric stress in the films; this can be large in films with high piezoelectric responses and high breakdown strengths. Additionally, the electric field history of the sample may

affect the domain structure, domain wall mobility, and fracture toughness. These results demonstrate a decrease in crack initiation stress in poled films or films under a DC bias. Poled films had the lowest crack initiation stress possibly due to a reduced number of domain walls, and creation of localized stress due to some ferroelastic reorientation; both of these factors would reduce the fracture toughness. Both PZT films that were pre-poled and those under a DC bias during mechanical testing showed larger piezoelectric properties, and required less stress to initiate a crack.

Additionally, the orientation of applied stress and electrical load of PZT films was studied. It was found that failure patterns depended on loading conditions. PZT films on Si wafers typically failed electromechanically, where thermal breakdown appeared along cracks. These cracks propagated perpendicular to the maximum tensile stress direction. The order in which failure events occurred depended on whether the electrical or mechanical failure criterion was met first. It is believed the presence of one failure facilitates subsequent failure events, as indicated by the numerous correlated cracks and thermal breakdown events.

In the course of this thesis, stresses in PZT thin films were shown to affect the domain wall motion, as well as the dielectric and piezoelectric properties. The influences of stress on the performance of PZT thin films indicate that stresses can be used to tailor properties and improve the functionality. In particular, compressive stresses enhance the piezoelectric coefficient. In addition, compressive residual stress should also increase the applied stress limits of these brittle films. Ultimately stresses may be used to improve the functionality of PZT thin films and proper stress management can also ensure high structural integrity. Both of these will improve the performance of PZT thin films for various piezoMEMS applications.

7.2   Future Work

This section explores several avenues of future research that would further quantify the relationships between stress and the domain orientation, properties, and failure limits of PZT thin films and other brittle, layered materials. **Section 7.2.1** describes possible material characterization techniques that could be used to determine structural changes in PZT films under stress. **Section 7.2.2** proposes a method to determine the fracture toughness and strength of PZT films. **Section 7.2.3** suggests techniques to quantify the oxygen vacancy concentrations $[V_O^{\cdot\cdot}]$ for PZT films on Ni and Si, which also may affect trends found in this thesis. **Section 7.2.4** explores the effect of strain on the aging rates of dielectric and piezoelectric properties to determine if certain strains can further stabilize the poled domain structure. This chapter ends in **Section 7.2.5** with a discussion of the procedures utilized in this work and their potential application to other material systems.

7.2.1   Structural characterization of films under strain

To complement the electrical characterization in **Chapter 3**, structural characterization of domain orientation as a function of applied strain can be used to further validate the hypothesis that some ferroelastic domain reorientation occurs in PZT films under strain. In particular, it would be useful to be able to determine the coercive stresses in PZT films as a function of Zr/Ti ratio, grain size, thickness, and residual stress state. It is proposed here that Raman analysis or X-Ray Diffraction (XRD) can be used to distinguish these differences.

Raman analysis has previously been used to understand the phase assemblages in PZT and quantify changes in stress and domain structures in piezoelectric thin films [98,204–211]. The Raman peaks of the $A_1(TO_1)$, $A_1(TO_2)$, $A_1(TO_3)$ and $E(LO_3)$ modes depend on stress and domain orientation, i.e. the percentage of the "c" domains, in PZT thin films [98,210,211]. For example, the $E(LO_3)$ mode intensity has been shown to increase when the percentage of "c" domains

decrease in PZT [98,210]. An increase in relative peak intensity with increasing tensile strain would thus confirm a decrease in "c" domains with applied tensile strain.

In an initial study to assess the viability of using Raman to determine domain reorientation, 0.6 μm PZT films on Ni foil substrates were subjected to different applied strains using the radius of curvature method (**Section 3.2.4**). Raman data were collected using a Horiba Scientific Labram HR Evolution Raman Spectrometer; a 633 nm wavelength laser with 0.9 numerical aperture and 1.5 mW power was used. In addition, Raman data were acquired for samples of Ni with only HfO_2 and $LaNiO_3$ (LNO) films to determine which Raman peaks corresponded to the underlying layers. At each applied stress state, 15 spots were scanned for a minimum of 6 minutes each.

The Raman data between 0 and 1000 cm^{-1} (**Figure 7-1**) show a number of broad peaks from different PZT and LNO modes, as detailed in

Table *7-1* [205,212]. The broad peak 6, from 700 to 730 cm^{-1}, corresponds to both the $E(LO_3)$ and $A_1(LO_3)$ modes [98]. To fit this peak, two Gaussian profiles at 700 and 733 cm^{-1} were used. To compare the changes in intensity with strain, the relative intensity of this peak was determined by dividing by a well-defined second peak that is ideally independent of stress and the PZT layer. To confirm the trend, the relative intensity of peak 6 should be normalized to multiple peaks, or the background.

Initially in this spectrum, the relative intensity of peak 6 was normalized using peak 4 because of its sharpness. Peak 4, which corresponded with the LNO E_g mode [212], was fitted at 400 cm^{-1} with a Gaussian profile. While $\frac{I_{peak\,6}}{I_{peak\,4}}$ increased linearly under tensile stress [212] (**Figure 7-1b**), the LNO layer may also have changed with strain. Therefore, the Raman spectra of stacks of the underlying layers (LNO/HfO_2/Ni) under the same applied strain were subtracted from the equivalent PZT/LNO/Ni spectra in order to remove the LNO peak. Unfortunately, after completing

126

this additional analysis, no clear trend between $I_{peak\ 6}$ and tensile strain was detected. This could suggest that the LNO mode changes with strain and convolutes the trend found in **Figure 7-1b**. Overall, no conclusive trend can be drawn from these initial results.

In future work, modified Raman analysis may be used to quantify the domain state changes in PZT. Removing the LNO layer to reduce overlap with lower intensity PZT peaks at lower Raman shifts will improve the results as has been widely reported in the literature [98,210,211]. The use of Pt bottom electrodes on Ni foil would ensure that no peaks from the underlying layers are in the spectrum. Polarized Raman should also be used to help decouple PZT modes that have similar Raman shifts with strain [98,207,209]. Additionally, the use of PZT films with larger grain size and narrower Raman peaks would improve peak fitting.
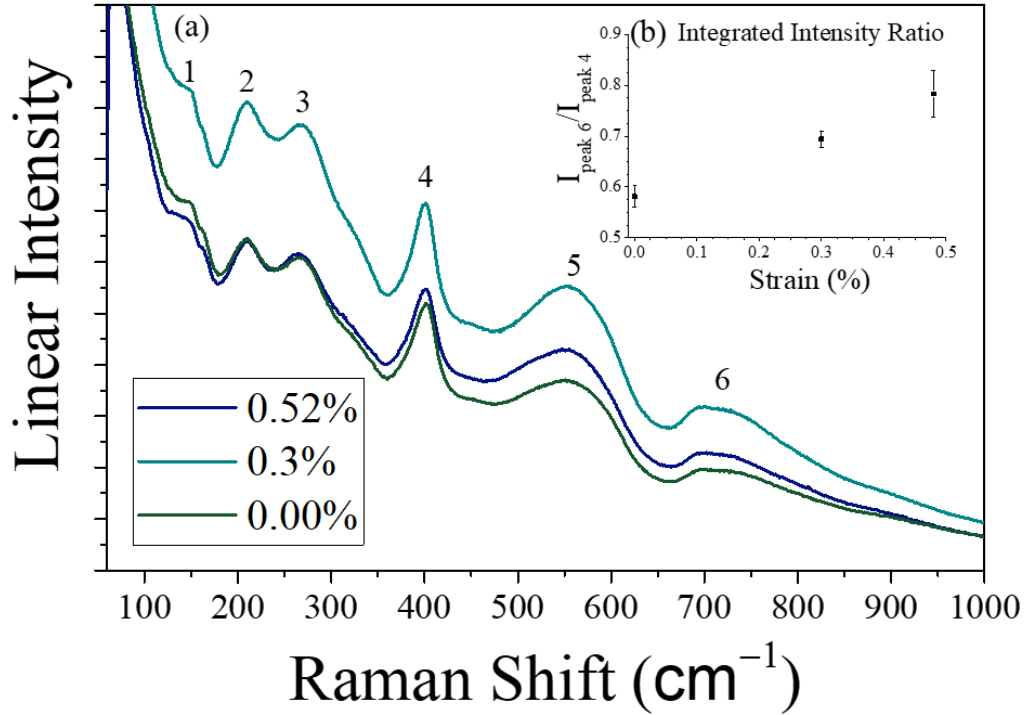
Figure 7-1. a) Raman spectra on Ni foil under different strain levels. The inset shows changes in $\frac{I_{peak\,6}}{I_{peak\,4}}$ as a function of applied strain level (b) Peak 4 corresponds to the 400 cm^{-1} E$_g$ LNO peak. Peak 6 corresponds with the E(LO$_3$) and the A$_1$(LO$_3$) PZT mode, which is dependent on the domain structure and the relative intensity decreases with a higher number of "c" domains.

Table 7-1. List of the PZT and LNO modes corresponding to the peaks in **Figure 7-1** [205,212].

Peak	Frequency (cm^{-1})	PZT Modes	LNO Modes
1	140-180	A$_1$(TO$_1$)	E$_g$ (at 150 cm^{-1})
2	~180-230	E(TO$_2$)	A$_1$g (at 220 cm^{-1})
3	~230-350	B$_1$, E(TO)$_4$	--
4	~350-420	--	E$_g$
5	~470-640	E(TO$_3$), ELO$_3$, ETO$_3$, A$_1$TO$_3$, A$_1$TO$_3$	--
6	~650-800	E(LO$_3$) and A$_1$(LO$_3$)	--

128

XRD could also be used to distinguish the changes in the domain structure with strain. Several studies have shown that the 001 and 002 peak intensities increase, while the 100 and 200 peak intensities decreases in tetragonal PZT thin films with an applied out-of-plane [46,70,213,214] electric field. Here, a similar study is proposed as a function of strain. While the data would be hard to collect on MPB films, due to the strong smearing between peaks, it is suggested that more interpretable data could be obtained with tetragonal compositions. Since ferroelastic reorientation may be limited for clamped films [46,215,216], films on more flexible substrates, like Ni foil, which show higher irreversible Rayleigh coefficients at room temperature and can achieve higher strains, should be used. Additional experiments combining electric fields and temperature sweeps with applied strain may further probe the energy barriers that reduce domain reorientation in thin films.

7.2.2   Determine the fracture toughness of PZT thin films

The PZT film's strength and fracture toughness (K_{IC}) influence the crack initiation stresses. In this thesis, bulk PZT K_{Ic} values were used in the finite fracture mechanics model [166] (**Chapter 5**) since data are not available for films. However, in PZT, the fracture toughness has been shown to vary with domain wall motion [182–185]. Since PZT films are clamped to the substrate and have limited domain wall motion [43,146], the lower reported fracture toughness values were used in the models of this thesis. However, it is likely that the fracture toughness is not constant. Instead, it is proposed that fracture toughness may change with film thickness, with thinner films having lower fracture toughness, due to reductions in ferroelastic wall mobility in thinner films.

To determine the fracture toughness of PZT thin films, a novel micromachined cantilever experiment is proposed [167,217–219]. In previous work on single crystal tungsten and CrN

coatings, micromachined cantilevers were etched using a focused ion beam [217–219]. A notch was etched into these beams and K_{Ic} was determined using **Equation 7-1,** where σ_f is the fracture stress, a is the notch depth, f is a shape factor, and t is the thickness [219].

$$K_{Ic} = \sigma_F \sqrt{\pi a} f \left(\frac{a}{t}\right) \tag{7-1}$$

For PZT films, σ_f is not well known but can be determined from un-notched micromachined cantilevers by using **Equation 7-2**, where l is the length from the fixed cantilever end to the applied force, $F,$ and B is the cantilever's width [219].

$$\sigma_F = 6\frac{Fl}{Bt^2} \tag{7-2}$$

In these studies, the cantilevers were made with focused ion beam etching; however this process is serial, and so limits generation of a statically significant set of data [218]. Thus, in order to increase the number of samples that may be tested, an array of PZT cantilevers can be fabricated through conventional microfabrication processes. For this purpose, PZT films should be grown on a Si wafer to various thicknesses in order to determine if the thickness of the film affects the PZT film's $K_{Ic.}$ Then, the PZT, LNO, and SiO_2 layers can be etched with CF_4, Cl_2, and Ar gas via a ULVAC plasma etching tool. Then the Si substrate would be etched in the Si deep reactive ion etch (DRIE) chamber using the Bosch method [220]. Finally, an isotropic etch of the Si using XeF_2 [221] would finish the process. These etching steps are shown schematically in **Figure 7-2**.
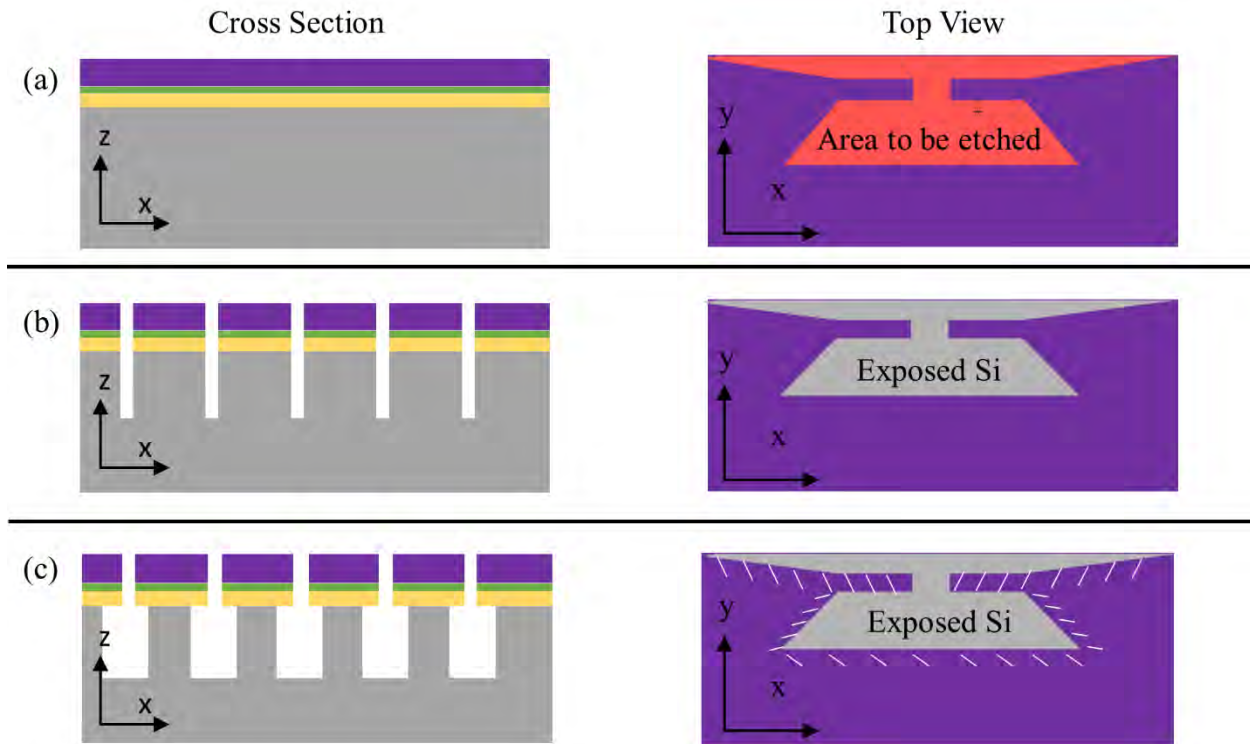
Figure 7-2. A schematic of the proposed nanofabrication of a series of released PZT thin film beams. (a) shows a schematic cross section of the as grown PZT layer (purple) on the LNO layer (green), on SiO_2 (yellow) and Si (gray) and a top view. (b) shows the first etches to create pits down through the Si layer. (c) shows the undercut of the Si layer which would release the PZT cantilever beams. The top view has white tick marks to represent the region that has been released.

Once the cantilevers are released, they can be tested in the micromachine nanoindenter (e.g. at the University of Leoben) to determine the film's strength and fracture toughness. A focused ion beam would then etch a notch on the cantilevers. The notch on the sample would act as a flaw of known size, such that when the sample breaks, the fracture toughness can be determined using **Equation 7-1**. Unnotched samples would be used to determine the material's strength.

Figure 7-3 shows a SEM cross section of an initial attempt to make PZT cantilevers. Unfortunately, process flaws precluded interpretable measurements during the course of this thesis. In particular, plasma etching damaged the PZT layer along the sidewall, exposing the

underlying SiO$_2$ layer (marked as "SiO$_2$ ledge"). Breaking these cantilevers with a nanoindenter did not accurately determine the fracture toughness. Future work should explore ways to create PZT cantilevers where the PZT edge is not damaged and SiO$_2$ layer exposure is minimized. For example, a sacrificial ZnO oxide layer deposited on a Si wafer via atomic layer deposition, replacing the SiO$_2$ layer, could be removed later in acetic acid [20]. Alternatively, a thinner SiO$_2$ layer could be used. A hard mask, instead of photoresist, should be used to better protect the PZT layer during etching.
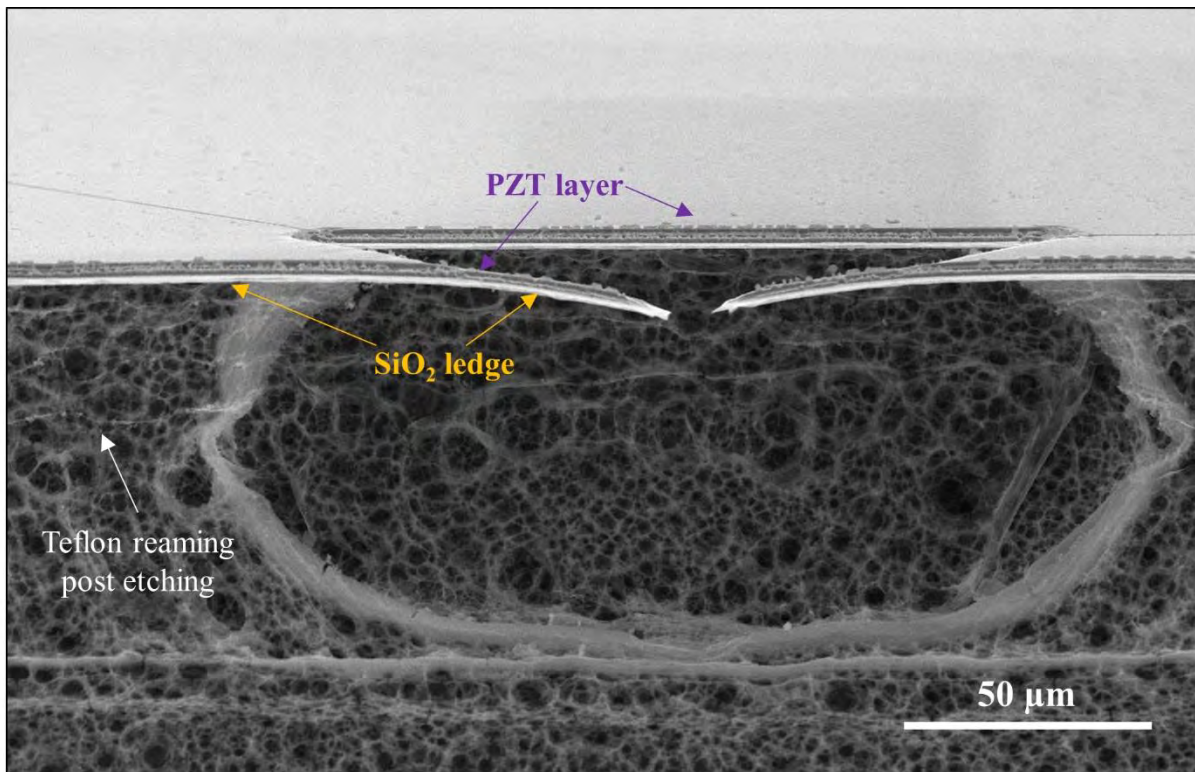
Figure 7-3. SEM cross section of the first generation of the nanofabricated PZT cantilevers. The cantilevers had SiO$_2$ ledge around the PZT layer leading to incorrect strength and fracture toughness measurements of the PZT layer.

In addition, PZT with higher fracture toughness will help improve the mechanical integrity and strain limits. Additional studies investigating the importance of grain size, domain size, and/or compositions such as PbO excess should also be explored. Additionally, device designs should

consider electrodes or layers on top and below the PZT layer to create some compressive stress in the PZT layer to enhance the applied stresses and strains that the PZT layer could withstand during application.

7.2.3 Investigate differences in defect chemistry

Chapter 4 links the differences in residual stresses with different pinning center distributions, domain wall mobilities, and tunability of various properties. However, different concentrations of domain boundaries, grain boundary, defect dipoles, and various mobile ionic species could also affect potentially the film's pinning center distribution [222,223]. In particular, there may be some differences in concentrations of $V_O^{\cdot\cdot}$ if the Ni substrate is severely oxidized during the crystallization steps, if the temperature distributions in the RTA step differ for different substrates, or if diffusion of PbO to the LaNiO$_3$ bottom electrode differs from that in Pt. Therefore, the differences in defect chemistry (especially the $V_O^{\cdot\cdot}$ concentration) should be determined for PZT on Ni and Si substrates. These factors can be studied via thermally stimulated depolarization current (TSDC) [224], energy dispersive X-Ray (EDX) using a transmission electron microscope, and electron energy loss spectroscopy (EELS) analysis [225].

TSDC current peaks can be used to differentiate trapped charges, defect dipoles, and ionic space charges [224,226]. By changing the poling temperature and heating ramp rate after poling, the types of ionic carriers and their associated activation energies can be determined [224–227]. For Nb doped PZT films made through a similar chemical solution deposition process, a peak for $V_O^{\cdot\cdot}$ is reported [227]; changes in the integrated peak intensity can be used to quantify the [$V_O^{\cdot\cdot}$] for PZT grown on Ni and Si substrates [227]. Additional samples of PZT grown on Ni with varying amounts of Ni oxidation could also be used to determine the effects of processing on the [$V_O^{\cdot\cdot}$].

133

7.2.4   Investigate relationship between strain and aging rates

This thesis investigated the coupling between mechanical and electrical loading, the functional properties, and the electromechanical limits. It is possible that the long-term retention of polarization may be affected by the applied stress in the film. Strains have been widely reported to affect domain switching and imprint [222]. It is proposed that in-plane strains in the film may affect the aging rate and the extent of domain backswitching. To explore this, PZT films under different amounts of in-plane strain (using the uniaxial beam bending method described in **Chapter 3**) could be interrogated to map the aging rates of the piezoelectric and dielectric properties as a function of strain. Beyond aging rates, the relaxation or resonance in the microwave region may suggest differences in the domain walls contributions and at which frequencies domains are contributing under various stress states. In addition, the role of strain gradients on imprint (with or without poling) could also be explored.

For this purpose, PZT can be grown on a Si substrate and cut into cantilever beams and uniaxial strain can be applied down the length of the cantilever, as described in **Section 3.2.4.** Under various applied strains, the film should be poled and the aging rate of the dielectric and piezoelectric properties post poling can be measured under the various applied strains. It is possible that the aging rate may decrease slightly with applied compressive strain since compressive strains favor the out-of-plane polarization and may reduce backswitching. These results can further expand upon the differences of the pinning centers work in **Chapter 4** and the relationship between compressive strains and stability of the poled domain structure.

7.2.5   Additional applications

The research conducted in this thesis relating stress to the mechanical limits in PZT thin films is applicable to other materials systems such as ceramic coatings and multilayer ceramic capacitors

(MLCCs). The methods used to determine stress limits for crack initiation and propagation in PZT films may improve coating thickness and MLCCs designs in other applications.

Ceramic coatings are widely used in the automotive [228], medical [229], and aerospace industries [228,230]. These coatings act as environmental and thermal shields; their high hardness improves resistance to abrasion. They are typically under large amounts of stress because of thermal cycling and deposition procedures [228]. Ceramic coatings deposited on metals are susceptible to mechanical failure through cracking or delamination due to the large differences in thermal expansion coefficients and elasticity between the materials [230]. Understanding the mechanical limits of ceramic coatings based on film thickness will likely identify improved coating thickness requirements for various applications [166,231,232]. The B3B biaxial test method and finite fracture mechanic models (**Chapter 5**) may prove useful in other ceramic coating systems. These test methods may determine the types and degree of stress ceramic coatings can withstand during operation based on their thickness.

Additionally, mechanical failure of MLCCs limits their performance and reliability in multiple electronic devices [233,234]. MLCCs are susceptible to cracking due to stresses in the dielectric layer from fabrication, board assembly (bending), and application [230,233,235]. These cracks create a short in the dielectric layer. This leads to localized heating, drains the power source, and results in device failure. Using the B3B biaxial method to test the stress limits in MLCCs may prove useful.

Overall, the methods presented in this thesis, particularly calculations of the film stresses, finite fracture mechanics, and ball on three ball testing can be adapted for other brittle materials systems, including coatings and multilayer stacks. The B3B method could overall be further expanded

135

beyond just *in situ* DC measurements. For example, temperature studies could also be performed. Additionally, optical sensing could be used to potentially determine the point of cracking in the samples. These methods may solve stress problems in other systems and help design systems with improved performance.

References

[1]   P. Muralt, R.G. Polcawich, S. Trolier-McKinstry, Piezoelectric thin films for sensors, actuators, and energy harvesting, MRS Bull. 34 (2009) 658–664. doi:10.1557/mrs2009.177.

[2]   N. Izyumskaya, Y.I. Alivov, S.J. Cho, H. Morkoç, H. Lee, Y.S. Kang, Processing, structure, properties, and applications of PZT thin films, Crit. Rev. Solid State Mater. Sci. 32 (2007) 111–202. doi:10.1080/10408430701707347.

[3]   C.B. Roundy, R.L. Byer, Sensitive $LiTaO_3$ pyroelectric detector, J. Appl. Phys. 44 (1973) 929–931. doi:10.1063/1.1662294.

[4]   S.B. Lang, S. Muensit, Review of some lesser-known applications of piezoelectric and pyroelectric polymers, Appl. Phys. A. 85 (2006) 125–134. doi:10.1007/s00339-006-3688-8.

[5]   B. Hanrahan, F. Sze, A. Smith, N. Jankowski, Thermodynamic cycle optimization for pyroelectric energy conversion in the thin film regime, Int. J. Energy Res. 41 (2017) 135–147. doi:10.1002/er.

[6]   G. Velarde, S. Pandya, L. Zhang, D. Garcia, E. Lupi, R. Gao, J.D. Wilbur, C. Dames, L.W. Martin, Quantifying intrinsic, extrinsic, dielectric, and secondary pyroelectric responses in $PbZr_{1-x}Ti_xO_3$ thin films, ACS Appl. Mater. Interfaces. 11 (2019) 35146–35154. doi:10.1021/acsami.9b12191.

[7]   R.B. Olsen, D.A. Bruno, J.M. Briscoe, Pyroelectric conversion cycles, J. Appl. Phys. 58 (1985) 4709–4716. doi:10.1063/1.336244.

[8]   M.E. Lines, A.M. Glass, Principles and Applications of Ferroelectrics and Related Materials, Oxford, 1977.

[9]   S.P. Alpay, J. Mantese, S. Trolier-McKinstry, Q. Zhang, R.W. Whatmore, Next-generation electrocaloric and pyroelectric materials for solid-state electrothermal energy interconversion, MRS Bull. 39 (2014) 1099–1109. doi:10.1557/mrs.2014.256.

[10]   J. Cooper, A fast-response pyroelectric thermal detector, J. Sci. Instrum. 39 (1962) 467–472. doi:10.1088/0950-7671/39/9/308.

[11]   R.W. Whatmore, P.C. Osbond, N.M. Shorrocks, Ferroelectric materials for thermal IR detectors, Ferroelectrics. 76 (1987) 351–367. doi:10.1080/00150198708016956.

[12]   N.M. Shorrocks, R.W. Wahtmore, P.C. Osbond, Lead scandium tantalate for thermal detector applications, Ferroelectrics. 106 (1990) 387–392. doi:10.1080/00150199008214614.

[13]   H. Kohlstedt, Y. Mustafa, A. Gerber, A. Petraru, M. Fitsilis, R. Meyer, U. Böttger, R. Waser, Current status and challenges of ferroelectric memory devices, Microelectron. Eng. 80 (2005) 296–304. doi:10.1016/j.mee.2005.04.084.

[14]   D. Damjanovic, Ferroelectric, dielectric and piezoelectric properties of ferroelectric thin films and ceramics, Reports Prog. Phys. 61 (1998) 1267–1324. doi:10.1088/0034-4885/61/9/002.

[15]   H.G. Yeo, S. Trolier-McKinstry, {001} Oriented piezoelectric films prepared by chemical solution deposition on Ni foils, J. Appl. Phys. 116 (2014) 014105. doi:10.1063/1.4886597.

[16]   H.G. Yeo, X. Ma, C. Rahn, S. Trolier-McKinstry, Efficient piezoelectric energy harvesters utilizing (001) textured bimorph PZT films on flexible metal foils, Adv. Funct. Mater. 26 (2016) 5940–5946. doi:10.1002/adfm.201601347.

[17]   S.C. Lin, W.J. Wu, Fabrication of PZT MEMS energy harvester based on silicon and stainless-steel substrates utilizing an aerosol deposition method, J. Micromechanics Microengineering. 23 (2013) 125028. doi:10.1088/0960-1317/23/12/125028.

[18]   B.A. Tuttle, J.A. Voigt, T.J. Garino, D.C. Goodnow, R.W. Schwartz, D.L. Lamppa, T.J. Headley, M.O. Eatough, Chemically prepared $Pb(Zr,Ti)O_3$ thin films: the effects of orientation and stress, ISAF '92 Proc. Eighth IEEE Int. Symp. Appl. Ferroelectr. (1992) 344–348. doi:10.1109/ISAF.1992.300703.

[19]   C.B. Yeager, Y. Ehara, N. Oshima, H. Funakubo, S. Trolier-McKinstry, Dependence of $e_{31,f}$ on polar axis texture for tetragonal $Pb(Zr_x,Ti_{1-x})O_3$ thin films, J. Appl. Phys. 116 (2014) 104907. doi:10.1063/1.4895339.

[20]   T. Liu, M. Wallace, S. Trolier-McKinstry, T.N. Jackson, High-temperature crystallized thin-film PZT on thin polyimide substrates, J. Appl. Phys. 122 (2017). doi:10.1063/1.4990052.

[21]   H.D. Chen, K. Udayakumar, K.K. Li, C.J. Gaskey, L.E. Cross, Dielectric breakdown strength in sol-gel derived PZT thick films, Integr. Ferroelectr. 15 (1997) 89–98. doi:10.1080/10584589708015699.

[22]   X. Ma, A. Wilson, C.D. Rahn, S. Trolier-McKinstry, Efficient energy harvesting using piezoelectric compliant mechanisms: theory and experiment, J. Vib. Acoust. Trans. ASME. 138 (2016) 1–9. doi:10.1115/1.4032178.

[23]   J.F. Tressler, S. Alkoy, R.E. Newnham, Piezoelectric sensors and sensor materials, J. Electroceramics. 2 (1998) 257–272. doi:10.1023/A:1009926623551.

[24]   S. Tadigadapa, K. Mateti, Piezoelectric MEMS sensors: State-of-the-art and perspectives, Meas. Sci. Technol. 20 (2009). doi:10.1088/0957-0233/20/9/092001.

[25]   S. Trolier-McKinstry, P. Muralt, Thin film piezoelectrics for MEMS, J. Electroceramics. 12 (2004) 7–17. doi:10.1023/B:JECR.0000033998.72845.51.

[26]   C.A. Randall, A. Kelnberger, G.Y. Yang, R.E. Eitel, T.R. Shrout, High strain piezoelectric multilayer actuators - A material science and engineering challenge, J. Electroceramics. 14 (2005) 177–191. doi:10.1007/s10832-005-0956-5.

138

[27]   F. Jona, G. Shirane, Ferroelectric Crystals, Pergamon Press Inc, Frankfurt, 1962.

[28]   T. Furukawa, Piezoelectricity and pyroelectricity in polymers, IEEE Trans. Electr. Insul. 24 (1989) 375–394. doi:10.1109/14.30878.

[29]   S. Trolier-McKinstry, R. Newnham, Materials Engineering: Bonding, Structure, and Structure-Property Relationships, Cambridge University Press, Cambridge, 2017. doi:10.1017/9781316217818.

[30]   R. Newnham, Properties of Materials: Anisotropy, Symmetry, Structure, Oxford University Press, Oxford, 2005.

[31]   M.A. Dubois, P. Muralt, Measurement of the effective transverse piezoelectric coefficient $e_{31,f}$ of AlN and $Pb(Zr_x,Ti_{1-x})O_3$ thin films, Sensors Actuators, A Phys. 77 (1999) 106–112. doi:10.1016/S0924-4247(99)00070-9.

[32]   C.B. Eom, S. Trolier-McKinstry, Thin-film piezoelectric MEMS, MRS Bull. 37 (2012) 1007–1017. doi:10.1557/mrs.2012.273.

[33]   B. Jaffe, W. Cooke, H. Jaffe, Piezoelectric Ceramics, Academic Press Limited, London, 1971.

[34]   T. Schenk, E. Yurchuk, S. Mueller, U. Schroeder, S. Starschich, U. Böttger, T. Mikolajick, About the deformation of ferroelectric hystereses, Appl. Phys. Rev. 1 (2014). doi:10.1063/1.4902396.

[35]   B. Akkopru-Akgun, W. Zhu, M.T. Lanagan, S. Trolier-McKinstry, The effect of imprint on remanent piezoelectric properties and ferroelectric aging of $PbZr_{0.52}Ti_{0.48}O_3$ thin films, J. Am. Ceram. Soc. 102 (2019) 5328–5341. doi:10.1111/jace.16367.

[36]   K. Kuramoto, E. Nakamura, Nonlinear dielectric constant of KH_2PO_4 in the ferroelectric phase, Ferroelectrics. 157 (1994) 57–62. doi:10.1080/00150199408229482.

[37]   Lord Rayleigh, XXV. Notes on Electricity and Magnetism. III. On the behaviour of iron and steel under the operation of feeble magentic forces, Philos. Mag. J. Sci. (1887) 225–245.

[38]   L. Néel, Theorie des Lois D'aimantation de Lord Rayleigh. 1re Partie: Les Deplacements d'une Paroi Isolee, Cah. Phys. 12 (1942).

[39]   L. Néel, Theorie des Lois D'aimantation de Lord Rayleigh. 2e Partie: Multiples Domaines et Champ Coercitif, Cah. Phys. 13 (1943).

[40]   D. Damjanovic, M. Demartin, The Rayleigh law in piezoelectric ceramics, J. Phys. D. Appl. Phys. 29 (1996) 2057–2060. doi:10.1088/0022-3727/29/7/046.

[41]   D. Damjanovic, Chapter 4: Hysteresis in piezoelectric and ferroelectric materials, in: Sci. Hysteresis, Elsevier, Oxford, 2005: pp. 337–465. doi:10.1016/B978-012480874-4/50022-

1.

[42]   N. Bassiri-Gharb, I. Fujii, E. Hong, S. Trolier-McKinstry, D. V. Taylor, D. Damjanovic, Domain wall contributions to the properties of piezoelectric thin films, J. Electroceramics. 19 (2007) 47–65. doi:10.1007/s10832-007-9001-1.

[43]   L.M. Denis, G. Esteves, J. Walker, J.L. Jones, S. Trolier-McKinstry, Thickness dependent response of domain wall motion in declamped {001} $Pb(Zr_{0.3}Ti_{0.7})O_3$ thin films, Acta Mater. 151 (2018) 243–252. doi:10.1016/j.actamat.2018.03.046.

[44]   K. Coleman, J. Walker, T. Beechem, S. Trolier-McKinstry, Effects of stresses on the dielectric and piezoelectric properties of $Pb(Zr_{0.52}Ti_{0.48})O_3$ thin films, J. Appl. Phys. 126 (2019) 034101. doi:10.1063/1.5095765.

[45]   W. Zhu, I. Fujii, W. Ren, S. Trolier-McKinstry, Influence of Mn doping on domain wall motion in $Pb(Zr_{0.52}Ti_{0.48})O_3$ films, J. Appl. Phys. 109 (2011) 064105. doi:10.1063/1.3552298.

[46]   M. Wallace, R.L. Johnson-Wilke, G. Esteves, C.M. Fancher, R.H.T. Wilke, J.L. Jones, S. Trolier-McKinstry, In situ measurement of increased ferroelectric/ferroelastic domain wall motion in declamped tetragonal lead zirconate titanate thin films, J. Appl. Phys. 117 (2015) 054103. doi:10.1063/1.4907394.

[47]   R.K. Vasudevan, D. Marincel, S. Jesse, Y. Kim, A. Kumar, S. V. Kalinin, S. Trolier-McKinstry, Polarization dynamics in ferroelectric capacitors: Local perspective on emergent collective behavior and memory effects, Adv. Funct. Mater. 23 (2013) 2490–2508. doi:10.1002/adfm.201203422.

[48]   D. Piazza, L. Stoleriu, L. Mitoseriu, A. Stancu, C. Galassi, Characterisation of porous PZT ceramics by first-order reversal curves (FORC) diagrams, J. Eur. Ceram. Soc. 26 (2006) 2959–2962. doi:10.1016/j.jeurceramsoc.2006.02.026.

[49]   D.J. Kim, J.H. Park, D. Shen, J.W. Lee, A.I. Kingon, Y.S. Yoon, S.H. Kim, Thickness dependence of submicron thick $Pb(Zr_{0.3}Ti_{0.7})O_3$ films on piezoelectric properties, Ceram. Int. 34 (2008) 1909–1915. doi:10.1016/j.ceramint.2007.07.016.

[50]   C.R. Cho, W.J. Lee, B.G. Yu, B.W. Kim, Dielectric and ferroelectric response as a function of annealing temperature and film thickness of sol-gel deposited $Pb(Zr_{0.52}Ti_{0.48})O_3$ thin film, J. Appl. Phys. 86 (1999) 2700–2711. doi:10.1063/1.371114.

[51]   L. Jin, V. Porokhonskyy, D. Damjanovic, Domain wall contributions in $Pb(Zr,Ti)O_3$ ceramics at morphotropic phase boundary: A study of dielectric dispersion, Appl. Phys. Lett. 96 (2010) 242902. doi:10.1063/1.3455328.

[52]   F. Wolf, A. Sutor, S.J. Rupitsch, R. Lerch, A generalized Preisach approach for piezoceramic materials incorporating uniaxial compressive stress, Sensors Actuators A. Phys. 186 (2012) 223–229. doi:10.1016/j.sna.2011.12.031.

[53] D.A. Hall, Rayleigh behaviour and the threshold field in ferroelectric ceramics, Ferroelectrics. 223 (1999) 319–328. doi:10.1080/00150199908260586.

[54] D. V. Taylor, D. Damjanovic, Domain wall pinning contribution to the nonlinear dielectric permittivity in Pb(Zr,Ti)O$_3$ thin films, Appl. Phys. Lett. 73 (1998) 2045–2047. doi:10.1063/1.122362.

[55] F. Preisach, Uber die madnetische Nachwirkung, Z. Phys. 94 (1935) 277–302.

[56] I.D. Mayergoyz, Mathematical Models of Hysteresis and Their Applications, Elsevier, Oxford, 2003.

[57] G. Robert, D. Damjanovic, N. Setter, A. Turik, Preisach modeling of piezoelectric nonlinearity in ferroelectric ceramics, J. Appl. Phys. 89 (2001) 5067–5073. doi:10.1063/1.1359166.

[58] A.T. Bartic, D.J. Wouters, H.E. Maes, J.T. Rickes, R.M. Waser, Preisach model for the simulation of ferroelectric capacitors, J. Appl. Phys. 89 (2001) 3420–3425. doi:10.1063/1.1335639.

[59] J.F. Shepard, P.J. Moses, S. Trolier-McKinstry, The wafer flexure technique for the determination of the transverse piezoelectric coefficient (d_{31}) of PZT thin films, Sensors Actuators A Phys. 71 (1998) 133–138. doi:10.1016/S0924-4247(98)00161-7.

[60] B.M. Foley, E.A. Paisley, C. Diantonio, T. Chavez, M. Blea-Kirby, G. Brennecka, J.T. Gaskins, J.F. Ihlefeld, P.E. Hopkins, Phonon scattering mechanisms dictating the thermal conductivity of lead zirconate titanate (PbZr$_{1-x}$Ti$_x$O$_3$) thin films across the compositional phase diagram, J. Appl. Phys. 121 (2017) 205104. doi:10.1063/1.4983356.

[61] B. Noheda, D.E. Cox, Bridging phases at the morphotropic boundaries of lead oxide solid solutions, Phase Transitions. 79 (2006) 5–20. doi:10.1080/01411590500467262.

[62] B. Noheda, D.E. Cox, G. Shirane, R. Guo, B. Jones, L.E. Cross, Stability of the monoclinic phase in the ferroelectric perovskite PbZr$_{1-x}$Ti$_x$O$_3$, Phys. Rev. B - Condens. Matter Mater. Phys. 63 (2001) 1–9. doi:10.1103/PhysRevB.63.014103.

[63] B. Noheda, J. Gonzalo, L. Cross, R. Guo, S. Park, D.E. Cox, G. Shirane, Tetragonal-to-monoclinic phase transition in a ferroelectric perovskite: The structure, Phys. Rev. B - Condens. Matter Mater. Phys. 61 (2000) 8687–8695. doi:10.1103/PhysRevB.61.8687.

[64] M.J. Haun, E. Furman, S.J. Jang, L.E. Cross, Thermodynamic thoery of the lead zirconate-titnate solid solution system, Part V: Theoritical calculations, Ferrolectrics. 99 (1989) 63–86.

[65] C.A. Randall, N. Kim, J.-P. Kucera, W. Cao, T.R. Shrout, Intrinsic and extrinsic size effects in fine-grained morphotropic-phase-boundary lead zirconate titanate ceramics, J. Am. Ceram. Soc. 81 (1998) 677–688. doi:10.1111/j.1151-2916.1998.tb02389.x.

[66] J. Petzelt, Dielectric grain-size effect in high-permittivity ceramics, Ferroelectrics. 400 (2010) 117–134. doi:10.1080/00150193.2010.505511.

[67] R.J. Ong, D.A. Payne, N.R. Sottos, Processing effects for integrated PZT: Residual stress, thickness, and dielectric properties, J. Am. Ceram. Soc. 88 (2005) 2839–2847. doi:10.1111/j.1551-2916.2005.00641.x.

[68] T.A. Berfield, R.J. Ong, D.A. Payne, N.R. Sottos, Residual stress effects on piezoelectric response of sol-gel derived lead zirconate titanate thin films, J. Appl. Phys. 101 (2007) 024102. doi:10.1063/1.2422778.

[69] G.A.C.M. Spierings, G.J.M. Dormans, W.G.J. Moors, M.J.E. Ulenaers, P.K. Larsen, Stresses in Pt/Pb(Zr,Ti)O$_3$/Pt thin-film stacks for integrated ferroelectric capacitors, J. Appl. Phys. 78 (1995) 1926–1933. doi:10.1063/1.360230.

[70] M. Eatough, D. Dimos, B.A. Tuttle, W.L. Warren, R. Bank, A study of switching behaivor in Pb (Zr, Ti)O$_3$ thin films using X-Ray diffraction, Mater. Res. Soc. Symp. Proc. 361 (1995) 111–116. http://journals.cambridge.org/abstract_S0883769400003614.

[71] Y. Bastani, T. Schmitz-Kempen, A. Roelofs, N. Bassiri-Gharb, Critical thickness for extrinsic contributions to the dielectric and piezoelectric response in lead zirconate titanate ultrathin films, J. Appl. Phys. 109 (2011) 014115. doi:10.1063/1.3527970.

[72] R.J. Zednik, A. Varatharajan, M. Oliver, N. Valanoor, P.C. McIntyre, Mobile ferroelastic domain walls in nanocrystalline PZT films: The direct piezoelectric effect, Adv. Funct. Mater. 21 (2011) 3104–3110. doi:10.1002/adfm.201100445.

[73] J. Ouyang, R. Ramesh, A.L. Roytburd, Intrinsic effective piezoelectric coefficient e$_{31,f}$ for ferroelectric thin films, Appl. Phys. Lett. 86 (2005) 152901. doi:10.1063/1.1899252.

[74] T. Oikawa, M. Aratani, H. Funakubo, K. Saito, M. Mizuhira, Composition and orientation dependence of electrical properties of epitaxial Pb(Zr$_x$Ti$_{1-x}$)O$_3$ thin films grown using metalorganic chemical vapor deposition, J. Appl. Phys. 95 (2004) 3111–3115. doi:10.1063/1.1645646.

[75] M.D. Nguyen, M. Dekkers, E. Houwman, R. Steenwelle, X. Wan, A. Roelofs, T. Schmitz-Kempen, G. Rijnders, Misfit strain dependence of ferroelectric and piezoelectric properties of clamped (001) epitaxial Pb(Zr$_{0.52}$,Ti$_{0.48}$)O$_3$ thin films, Appl. Phys. Lett. 99 (2011) 252904. doi:10.1063/1.3669527.

[76] B.A. Tuttle, R.W. Schwartz, Solution deposition of ferroelectric thin films, MRS Bull. 21 (1996) 49–54. doi:10.1557/S088376940004608X.

[77] H. Hoshyarmanesh, N. Nehzat, M. Salehi, M. Ghodsi, X-ray diffraction measurement of residual stress in sol-gel grown lead zirconate titanate thick films on nickel-based super alloy substrate, J. Mech. Sci. Technol. 29 (2015) 715–721. doi:10.1007/s12206-015-0131-0.

[78] S.B. Desu, Influence of stresses on the properties of ferroelectric BaTiO$_3$ thin films, J. Electrochem. Soc. 140 (1993) 2981–2987. doi:10.1149/1.2220943.

[79] F. Xu, F. Chu, S. Trolier-McKinstry, Longitudinal piezoelectric coefficient measurement for bulk ceramics and thin films using pneumatic pressure rig, J. Appl. Phys. 86 (1999) 588–594. doi:10.1063/1.370771.

[80] M.B. Kelman, P.C. McIntyre, B.C. Hendrix, S.M. Bilodeau, J.F. Roeder, Effect of applied mechanical strain on the ferroelectric and dielectric properties of thin films, 9231 (2006) 9231. doi:10.1063/1.1569431.

[81] R.F. Brown, Effect of two-dimensional mechanical stress on the dielectric properties of poled ceramic barium titanate and lead zirconate titanate, Can. J. Phys. 39 (1961) 741–753. doi:10.1139/p61-082.

[82] R.F. Brown, G.. McMahon, Material constants of ferroelectric ceramics at high pressure, Can. J. Phys. 40 (1962) 672–674. doi:10.1139/p62-070.

[83] D.A. Berlincourt, H.H.A. Krueger, Behavior of piezoelectric ceramics under various environmental and opertation conditions of radiating sonar trasnducers, Washington DC, 1964.

[84] S. Trolier-McKinstry, C.A. Randall, J.P. Maria, C. Theis, D.G. Schlom, J. Shepard, K. Yamakawa, Size effects and domains in ferroelectric thin film actuators, MRS Proc. 433 (1996) 363–374. doi:10.1557/PROC-433-363.

[85] J.F. Shepard, S. Trolier-McKinstry, M. Hendrickson, R. Zeto, The effects of biaxial stress on the ferroelectric characteristics of PZT thin films, Mater. Res. Soc. Symp. Proc. 459 (1997) 47–51.

[86] J.F. Shepard, S. Trolier-McKinstry, M.A. Hendrickson, R. Zeto, Properties of PZT thin films as a function of in-plane biaxial stress, ISAF '96. Proc. Tenth IEEE Int. Symp. Appl. Ferroelectr. 1 (1996) 161–165. doi:10.1109/ISAF.1996.602728.

[87] J.F. Ihlefeld, D.T. Harris, R. Keech, J.L. Jones, J.P. Maria, S. Trolier-McKinstry, Scaling effects in perovskite ferroelectrics: Fundamental limits and process-structure-property relations, J. Am. Ceram. Soc. 99 (2016) 2537–2557. doi:10.1111/jace.14387.

[88] Y. Pauleau, Generation and evolution of residual stresses in physical vapour-deposited thin films, Vacuum. 61 (2001) 175–181. doi:10.1016/S0042-207X(00)00475-9.

[89] J.A. Thornton, Influence of apparatus geometry and deposition conditions on the structure and topography of thick sputtered coatings, J. Vac. Sci. Technol. 11 (1974) 666–670. doi:10.1116/1.1312732.

[90] B.A. Movchan, A. V. Demchishin, Study of the structure and properties of thick vacuum condensates of nickel, titanium, tungsten, aluminium oxide and zirconium dioxide, Fix. Met. Met. 28 (1969) 653–660.

[91] C.B. Yeager, S. Trolier-McKinstry, Epitaxial $Pb(Zr_x,Ti_{1-x})O_3$ ($0.30 \leq x \leq 0.63$) films on (100) MgO substrates for energy harvesting applications, J. Appl. Phys. 112 (2012) 074107. doi:10.1063/1.4754015.

[92] R. Treml, D. Kozic, J. Zechner, X. Maeder, B. Sartory, H.P. Gänser, R. Schöngrundner, J. Michler, R. Brunner, D. Kiener, High resolution determination of local residual stress gradients in single- and multilayer thin film systems, Acta Mater. 103 (2016) 616–623. doi:10.1016/j.actamat.2015.10.044.

[93] D. Das, L. Sanchez, J. Martin, B. Power, S. Isaacson, R.G. Polcawich, I. Chasiotis, Control of mechanical response of freestanding $PbZr_{0.52}Ti_{0.48}O_3$ films through texture, Appl. Phys. Lett. 109 (2016) 131905. doi:10.1063/1.4963348.

[94] C. Brinker, G. Scherer, Sol-gel science: The physics and chemistry of sol-gel processing, Academic Press, Inc, 1990.

[95] M. Ohring, Mechanical properties of thin films, in Materials Science of Thin Films Deposition and Structure, in: Second, Academic Press, Inc, San Diego, 2002: pp. 711–781. doi:10.1017/CBO9781107415324.004.

[96] G.C.A.M. Janssen, M.M. Abdalla, F. van Keulen, B.R. Pujada, B. van Venrooy, Celebrating the 100th anniversary of the Stoney equation for film stress: Developments from polycrystalline steel strips to single crystal silicon wafers, Thin Solid Films. 517 (2009) 1858–1867. doi:10.1016/j.tsf.2008.07.014.

[97] E. Chason, P.R. Guduru, Tutorial: Understanding residual stress in polycrystalline thin films through real-time measurements and physical models, J. Appl. Phys. 119 (2016) 191101. doi:10.1063/1.4949263.

[98] K. Nishida, M. Osada, S. Wada, S. Okamoto, R. Ueno, H. Funakubo, T. Katoda, A new method to characterize a relative volume to the c-domain in PZT films based on Raman spectra, Integr. Ferroelectr. 78 (2006) 281–287. doi:10.1080/10584580600663425.

[99] G.G. Stoney, The tension of metallic films deposited by electrolysis, Proc. R. Soc. London A. 82 (1909) 172–175.

[100] Z. Qiu, J.S. Pulskamp, X. Lin, C. Rhee, T. Wang, R.G. Polcawich, K. Oldham, Large displacement vertical translational actuator based on piezoelectric thin films, J. Micromechanics Microengineering. 20 (2010) 075016. doi:10.1088/0960-1317/20/7/075016.

[101] D. Kim, J. Maria, A.I. Kingon, Compositional effects on the piezoelectric and ferroelectric properties of chemical solution deposited PZT thin films, 688 (2020) 1–6.

[102] L.M. Garten, S. Trolier-McKinstry, The field induced $e_{31,f}$ piezoelectric and Rayleigh response in barium strontium titanate thin films, Appl. Phys. Lett. 105 (2014) 132905. doi:10.1063/1.4897299.

[103] H. Nagata, S.W. Ko, E. Hong, C.A. Randall, S. Trolier-McKinstry, P. Pinceloup, D. Skamser, M. Randall, A. Tajuddin, Microcontact printed $BaTiO_3$ and $LaNiO_3$ thin films for capacitors, J. Am. Ceram. Soc. 89 (2006) 2816–2821. doi:10.1111/j.1551-2916.2006.01137.x.

[104] Y. Zhang, X. Tang, G. Wang, X. Dong, Effect of acetic acid/water ratio on the microstructure and properties of $LaNiO_3$ thin films by metal organic solution deposition, Mater. Sci. Forum. 815 (2015) 89–93. doi:10.4028/www.scientific.net/MSF.815.89.

[105] T. Tani, D.A. Payne, Lead oxide coatings on sol-gel-derived lead lanthanum zirconium titanate thin layers for enhanced crystallization into the perovskite structure, J. Am. Ceram. Soc. 77 (1994) 1242–1248.

[106] F. Weitzer, P. Rogl, H. Noël, The ternary system: Hafnium-silicon-uranium, J. Alloys Compd. 387 (2005) 246–250. doi:10.1016/j.jallcom.2004.06.067.

[107] JCPDS 33–0710, Wustenberg, H., Hahn, Inst. fur Kristallogr., Technische Hochschule, Aachen, Germany, ICDD Grant-in-Aid, 1981, (n.d.).

[108] D. P. Rodionov, I. V. Gervas'eva, Yu. V. Khlebnikova, V. A. Sazonova, and B. K. Sokolov, Effect of alloying and heat treatment on the formation of recrystallization cube texture in nickel alloys, Phys. Met. Metallogr. 99 (2005) 80–89, (n.d.).

[109] M. Zinkevich, Constitution of the Sr-Ni-O system, J. Solid State Chem. 178 (2005) 2818–2824. doi:10.1016/j.jssc.2005.06.035.

[110] T. Mori, R. Manory, G. Kimmel, No, Ben-Gurion Univ. Negev, ICDD Grant-in Aid. (2002).

[111] K. Kakegawa, J. Mohri, T. Takahashi, H. Yamamura, S. Shirasaki, A compositional fluctuation and properties of $Pb(Zr,Ti)O_3$, Solid State Commun. 24 (1977) 769–772. doi:10.1016/0038-1098(77)91186-3.

[112] Y. Okada, Y. Tokumaru, Precise determination of lattice parameter and thermal expansion coefficient of silicon between 300 and 1500 K, J. Appl. Phys. 56 (1984) 314–320. doi:10.1063/1.333965.

[113] L. Jordan, W.H. Swanger, The properties of pure nickel, Bur. Stand. J. Res. 5 (1930) 1291–1307.

[114] W.R. Cook, D.A. Berlincourt, F.J. Scholz, Thermal expansion and pyroelectricity in lead titanate zirconate and barium titanate, J. Appl. Phys. 34 (1963) 1392–1398. doi:10.1063/1.1729587.

[115] M.J. Haun, Z.Q. Zhuang, E. Furman, S.J. Jang, L.E. Cross, Thermodynamic thoery of the lead zirconate-titnate solid solution system, part III: Curie constant and sixth-order polarization interaction dielectric stiffness coefficients, Ferroelectrics. 99 (1989) 45–54.

[116] W.L. Warren, D. Dimos, B.A. Tuttle, G.E. Pike, M. V Raymond, R.D. Nasby, R. Ramesh,

J.T. Evans, R. Bank, Mechanism(s) for the suppression of the swtichable polarization in PZT and BaTiO₃, Mat. Res. Soc. Symp. Proc. 361 (1995) 51–65.

[117] J.J. Wang, Y. Wang, J.F. Ihlefeld, P.E. Hopkins, L.Q. Chen, Tunable thermal conductivity via domain structure engineering in ferroelectric thin films: A phase-field simulation, Acta Mater. 111 (2016) 220–231. doi:10.1016/j.actamat.2016.03.069.

[118] R.W. Whatmore, Pyroelectric devices and materials, Reports Prog. Phys. 49 (1986) 1335–1386.

[119] N.M. Shorrocks, A. Patel, M.J. Walker, A.D. Parson, Integrated thin film PZT pyroelectric detector arrays, Microelectron. Eng. 29 (1995) 59–65.

[120] D. Setiadi, H. Weller, T.D. Binnie, A pyroelectric polymer infrared sensor array with a charge amplifier readout, Sensors & Actuators. 76 (1999) 145–151.

[121] R.W. Whatmore, Q. Zhang, C.P. Shaw, R.A. Dorey, J.R. Alcock, Pyroelectric ceramics and thin films for applications in uncooled infra-red sensor arrays, Phys. Scr. T129 (2007) 6–11. doi:10.1088/0031-8949/2007/T129/002.

[122] S. Pandya, G.A. Velarde, R. Gao, A.S. Everhardt, J.D. Wilbur, R. Xu, J.T. Maher, J.C. Agar, C. Dames, L.W. Martin, J.D. Zook, S.T. Liu, T.A. Patel, K. Co, R.J. Hebert, S.P. Alpay, G.A. Velarde, S. Pandya, L. Zhang, D. Garcia, E. Lupi, R. Gao, J.D. Wilbur, C. Dames, L.W. Martin, Ferroelectric films on metal substrates: The role of thermal expansion mismatch on dielectric, piezoelectric, and pyroelectric properties, J. Appl. Phys. 11 (2019) 1803312. doi:10.1063/1.325442.

[123] Z. Zhang, B. Hanrahan, C. Shi, A. Khaligh, Management and storage of energy converted via a pyroelectric heat engine, Appl. Energy. 230 (2018) 1326–1331. doi:10.1016/j.apenergy.2018.09.101.

[124] S. Pandya, G.A. Velarde, R. Gao, A.S. Everhardt, J.D. Wilbur, R. Xu, J.T. Maher, J.C. Agar, C. Dames, L.W. Martin, Understanding the role of ferroelastic domains on the pyroelectric and electrocaloric effects in ferroelectric thin films, Adv. Mater. 31 (2019) 1803312. doi:10.1002/adma.201803312.

[125] M.E. Lines, A.M. Glass, Chapter 16, in: Princ. Appl. Ferroelectr. Relat. Mater., 1977.

[126] R. Bruchhaus, D. Pitzer, R. Primig, M. Schreiter, W. Wersing, Sputtering of PZT thin films for surface micromachined IR-detector arrays Sputtering of PZT Thin Films for Surface, Integr. Ferroelectr. 25 (1999) 1–11. doi:10.1080/10584589908210154.

[127] R.W. Whatmore, Pyroelectric arrays: ceramics and thin films, J. Electroceramics. 13 (2004) 139–147.

[128] P. Muralt, Micromachined infrared detectors based on pyroelectric thin films, Reports Prog. Phys. 64 (2001) 1339–1388.

[129] I. Lubomirsky, O. Stafsudd, Invited review article: Practical guide for pyroelectric measurements, Rev. Sci. Instrum. 83 (2012) 051101. doi:10.1063/1.4709621.

[130] J.D. Zook, S.T. Liu, Pyroelectric effects in thin film, J. Appl. Phys. 49 (1978) 4604–4606. doi:10.1063/1.325442.

[131] Y. Ivry, V. Lyahovitskaya, I. Zon, I. Lubomirsky, E. Wachtel, A. Roytburd, Enhanced pyroelectric effect in self- supported films of BaTiO3 with polycrystalline macrodomains, Appl. Phys. Lett. 90 (2007) 172905. doi:10.1063/1.2730749.

[132] J. Karthik, J.C. Agar, A.R. Damodaran, L.W. Martin, Effect of 90° domain walls and thermal expansion mismatch on the pyroelectric properties of epitaxial $PbZr_{0.2}Ti_{0.8}O_3$ thin films, Phys. Rev. Lett. 109 (2012) 257602. doi:10.1103/PhysRevLett.109.257602.

[133] B. Hanrahan, Y. Espinal, C. Neville, R. Rudy, M. Rivas, A. Smith, M.T. Kesim, S.P. Alpay, Accounting for the various contributions to pyroelectricity in lead zirconate titanate thin films, J. Appl. Phys. 123 (2018) 124104. doi:10.1063/1.5012984.

[134] R. Keech, L. Ye, J.L. Bosse, G. Esteves, J. Guerrier, J.L. Jones, M.A. Kuroda, B.D. Huey, S. Trolier-McKinstry, Declamped piezoelectric coefficients in patterned 70/30 lead magnesium niobate − lead titanate thin films, Adv. Funct. Mater. 27 (2017) 1605014. doi:10.1002/adfm.201605014.

[135] R.E. Eitel, T.R. Shrout, C.A. Randall, Nonlinear contributions to the dielectric permittivity and converse piezoelectric coefficient in piezoelectric ceramics, J. Appl. Phys. 99 (2006) 124110. doi:10.1063/1.2207738.

[136] S. Shetty, S. Trolier-McKinstry, Non-linearity in engineered lead magnesium niobate ($PbMg_{1/3}Nb_{2/3}O_3$) thin films., J. Appl. Physics, Submitt. (2019).

[137] I. Fujii, E. Hong, S. Trolier-McKinstry, Thickness dependence of dielectric nonlinearity of lead zirconate titanate films, IEEE Trans. Ultrason. Ferroelectr. Freq. Control. 57 (2010) 1717–1723. doi:10.1109/TUFFC.2010.1610.

[138] K. Coleman, R. Bermejo, D. Leguillon, S. Trolier-McKinstry, Thickness dependence of crack initiation and propagation in piezoelectric microelectromechanical stacks, Acta Mater. 191 (2020) 245–252. doi:10.1016/j.actamat.2020.03.030.

[139] Y.S. Touloukian, R.K. Kirby, R.E. Taylor, P.D. Desal, Thermophysical properties of matter-The TPRC data series-Vol. 12. Thermal Expansion Metallic elements and Alloys, 1975. doi:10.1007/s13398-014-0173-7.2.

[140] Y.S. Touloukian, R.K. Kirby, R.E. Taylor, T.Y.R. Lee, Thermophysical Properties of Matter - the TPRC Data Series. Volume 13. Thermal Expansion - Nonmetallic Solids, 1975.

[141] M.J. Haun, E. Furman, H.A. McKinstry, L.E. Cross, Thermodynamic theory of the lead zirconate-titanate solid solution system, Part II Tricritical Behaivor, Ferroelectrics. 99 (1989) 27–44.

[142] B. Noheda, D.E. Cox, G. Shirane, J.A. Gonzalo, L.E. Cross, S.E. Park, A monoclinic ferroelectric phase in the $Pb(Zr_{1-x}Ti_x)O_3$ solid solution, Appl. Phys. Lett. 74 (1999) 2059–2061. doi:10.1063/1.123756.

[143] D.E. Cox, B. Noheda, G. Shirane, Y. Uesu, K. Fujishiro, Y. Yamada, Universal phase diagram for high-piezoelectric perovskite systems, Appl. Phys. Lett. 79 (2001) 400–402. doi:10.1063/1.1384475.

[144] A.J. Bell, E. Furman, An alternative thermodynamic model for PZT, IEEE Int. Symp. Appl. Ferroelectr. (2002) 19–24. doi:10.1109/isaf.2002.1195860.

[145] M.I. Morozov, D. Damjanovic, Hardening-softening transition in Fe-doped $Pb (Zr,Ti) O_3$ ceramics and evolution of the third harmonic of the polarization response, J. Appl. Phys. 104 (2008). doi:10.1063/1.2963704.

[146] G. Han, J. Ryu, W.H. Yoon, J.J. Choi, B.D. Hahn, D.S. Park, Effect of film thickness on the piezoelectric properties of lead zirconate titanate thick films fabricated by aerosol deposition, J. Am. Ceram. Soc. 94 (2011) 1509–1513. doi:10.1111/j.1551-2916.2010.04276.x.

[147] A. Mazzalai, D. Balma, N. Chidambaram, P. Muralt, L. Colombo, T. Schmitz-Kempen, Dynamic and long-time tests of the transverse piezoelectric coefficient in PZT thin films, IEEE Int. Symp. Appl. Ferroelectr. Proc. (2014) 1–4. doi:10.1109/ISAF.2014.6922998.

[148] W. Zhu, T. Borman, K. Decesaris, B. Truong, M.M. Lieu, S.W. Ko, P. Mardilovich, S. Trolier-McKinstry, Influence of PbO content on the dielectric failure of Nb - doped {100} - oriented lead zirconate titanate films, J. Am. Ceram. Soc. 102 (2018) 1734–1740. doi:10.1111/jace.16000.

[149] T.M. Borman, W. Zhu, K. Wang, S.W. Ko, P. Mardilovich, S. Trolier-McKinstry, Effect of lead content on the performance of niobium-doped {100} textured lead zirconate titanate films, J. Am. Ceram. Soc. (2017) 3558–3567. doi:10.1111/jace.14892.

[150] Z. Luo, S. Pojprapai, J. Glaum, M. Hoffman, Electrical fatigue-induced cracking in lead zirconate titanate piezoelectric ceramic and its influence quantitatively analyzed by refatigue method, J. Am. Ceram. Soc. 95 (2012) 2593–2600. doi:10.1111/j.1551-2916.2012.05232.x.

[151] T.M. Borman, {001} textured growth of doped, gradient free lead zirconate titanate thin films by chemical solution deposition, Pennsylvania State University, 2016.

[152] O.M. Jadaan, N.N. Nemeth, J. Bagdahn, W.N. Sharpe, Probabilistic Weibull behavior and mechanical properties of MEMS brittle materials, J. Mater. Sci. 38 (2003) 4087–4113. doi:10.1023/A:1026317303377.

[153] W. Weibull, A statistical distribution function of wide applicability, J. Appl. Mech. (1951) 293–297.

[154] W. Weibull, A statistical theory of strength of materials, Royal Swedish Institute for Engineering Research, 1939.

[155] D. Leguillon, E. Martin, Prediction of multi-cracking in sub-micron films using the coupled criterion, Int. J. Fract. 209 (2018) 187–202. doi:10.1007/s10704-017-0255-6.

[156] D. Damjanovic, F. Chu, D. V Taylor, M.D. Maeder, L. Sagalowicz, P.D. Martin, N. Setter, Engineering of piezoelectric properties in ferroelectric, Cerámica Vidr. 38 (1999) 538–544.

[157] K.S. Chen, A. Ayon, S.M. Spearing, Controlling and testing the fracture strength of silicon on the mesoscale, J. Am. Ceram. Soc. 83 (2000) 1476–1484. doi:10.1111/j.1151-2916.2000.tb01413.x.

[158] C. Funke, E. Kullig, M. Kuna, H.J. Möller, Biaxial fracture test of silicon wafers, Adv. Eng. Mater. 6 (2004) 594–598. doi:10.1002/adem.200400406.

[159] D.H. Alsem, B.L. Boyce, E.A. Stach, R.O. Ritchie, Effect of post-release sidewall morphology on the fracture and fatigue properties of polycrystalline silicon structural films, Sensors Actuators, A Phys. 147 (2008) 553–560. doi:10.1016/j.sna.2008.05.027.

[160] J.B. Wachtman, W.R. Cannon, M.J. Mathewson, Statistical treatment of strength, in: Mech. Prop. Ceram., Second, John Wiley & Sons Inc, Hoboken, 2009: pp. 119–149.

[161] P. Cornetti, A. Sapora, Penny-shaped cracks by finite fracture mechanics, Int. J. Fract. 219 (2019) 153–159. doi:10.1007/s10704-019-00383-9.

[162] A.A. Griffith, The phenomena of rupture and flow in solids, Philos. Trans. R. Soc. London. Ser. A. (1921) 163–198.

[163] J.B. Wachtman, W.R. Cannon, M.J. Matthewson, Stable Crack Propagation and R-Curve Behavior, in: J.W. and Sons (Ed.), Mech. Prop. Ceram., Second, Hoboken, 2009: pp. 177–187. doi:10.1002/9780470451519.ch9.

[164] G. R. Irwin, Linear fracture mechanics, fracture transition, and fracture control, Eng. Fract. Mech. 1 (1968) 241–257.

[165] R. Hertzberg, R. Vinci, J. Hertzberg, Elements of fracture mechanics, in: Deform. Fract. Mech. Eng. Mater., 5th ed., 2013: pp. 299–381.

[166] D. Leguillon, Strength or toughness? A criterion for crack onset at a notch, Eur. J. Mech. A/Solids. 21 (2002) 61–72. doi:10.1016/S0997-7538(01)01184-6.

[167] R. Bermejo, R. Daniel, C. Schuecker, O. Paris, R. Danzer, C. Mitterer, Hierarchical architectures to enhance structural and functional properties of brittle materials, Adv. Eng. Mater. 19 (2017) 1600683. doi:10.1002/adem.201600683.

[168] D. Leguillon, É. Martin, M.C. Lafarie-Frenot, Flexural vs. tensile strength in brittle materials, Comptes Rendus - Mec. 343 (2015) 275–281. doi:10.1016/j.crme.2015.02.003.

[169] D. Taylor, The theory of critical distances, Eng. Fract. Mech. 75 (2008) 1696–1705. doi:10.1016/j.engfracmech.2007.04.007.

[170] O. Ševeček, M. Kotoul, D. Leguillon, E. Martin, R. Bermejo, Modelling of edge crack formation and propagation in ceramic laminates using the stress–energy coupled criterion, Eng. Fract. Mech. 167 (2016) 45–55. doi:10.1016/j.engfracmech.2016.03.039.

[171] A. Börger, P. Supancic, R. Danzer, The ball on three balls test for strength testing of brittle discs: Part II: Analysis of possible errors in the strength determination, J. Eur. Ceram. Soc. 24 (2004) 2917–2928. doi:10.1016/j.jeurceramsoc.2003.10.035.

[172] R. Danzer, P. Supancic, W. Harrer, Biaxial tensile strength test for brittle rectangular plates, J. Ceram. Soc. Japan. 114 (2006) 1054–1060. doi:10.2109/jcersj.114.1054.

[173] M. Deluca, R. Bermejo, M. Pletz, P. Supancic, R. Danzer, Strength and fracture analysis of silicon-based components for embedding, J. Eur. Ceram. Soc. 31 (2011) 549–558. doi:10.1016/j.jeurceramsoc.2010.10.029.

[174] M. Deluca, R. Bermejo, M. Pletz, M. Wießner, P. Supancic, R. Danzer, Influence of deposited metal structures on the failure mechanisms of silicon-based components, J. Eur. Ceram. Soc. 32 (2012) 4371–4380. doi:10.1016/j.jeurceramsoc.2012.06.027.

[175] R. Bermejo, P. Supancic, R. Danzer, Influence of measurement uncertainties on the determination of the Weibull distribution, J. Eur. Ceram. Soc. 32 (2012) 251–255. doi:10.1016/j.jeurceramsoc.2011.09.008.

[176] ASTM C1239-13(2018), Standard practice for reporting uniaxial strength data and estimating Weibull distribution parameters for advanced ceramics, ASTM International, West Conshohocken, PA, 2018, n.d.

[177] T. Yi, L. Li, C.-J. Kim, Microscale material testing of single crystalline silicon: process effects on surface morphology and tensile strength, Sensors Actuators A Phys. 83 (2000) 172–178. doi:10.1016/S0924-4247(00)00350-2.

[178] I. Chasiotis, W.G. Knauss, The mechanical strength of polysilicon films: Part 1. The influence of fabrication governed surface conditions, J. Mech. Phys. Solids. 51 (2003) 1533–1550. doi:https://doi.org/10.1016/S0022-5096(03)00051-6.

[179] R. Bermejo, "Toward seashells under stress": Bioinspired concepts to design tough layered ceramic composites, J. Eur. Ceram. Soc. 37 (2017) 3823–3839. doi:10.1016/j.jeurceramsoc.2017.04.041.

[180] L. Hai-Bo, C. Mao-Sheng, Y. Jie, W. Da-Wei, Z. Quan-Liang, W. Fu-Chi, Enhanced mechanical behaviour of lead zirconate titanate piezoelectric composites incorporating zinc oxide nanowhiskers, Chinese Phys. B. 17 (2008) 4323–4327. doi:10.1088/1674-1056/17/11/060.

[181] K. Zhang, F.W. Zeng, H. Wang, H.T. Lin, Biaxial flexural strength of poled lead zirconate

titanate under high electric field with extended field range, Ceram. Int. 39 (2013) 2023–2030. doi:10.1016/j.ceramint.2012.08.054.

[182] S.L. dos Santos e Lucato, D.C. Lupascu, J. Rödel, Effect of poling direction on R-curve behavior in lead zirconate titanate, J. Am. Ceram. Soc. 83 (2000) 424–426. doi:10.1111/j.1151-2916.2000.tb01210.x.

[183] K. Mehta, A. V. Virkar, Fracture mechanisms in ferroelectric-ferroelastic lead zirconate titanate (Zr: Ti=0.54:0.46) ceramics, J. Am. Ceram. Soc. 73 (1990) 567–574. doi:10.1111/j.1151-2916.1990.tb06554.x.

[184] R. Bermejo, H. Grünbichler, J. Kreith, C. Auer, Fracture resistance of a doped PZT ceramic for multilayer piezoelectric actuators: Effect of mechanical load and temperature, J. Eur. Ceram. Soc. 30 (2010) 705–712. doi:10.1016/j.jeurceramsoc.2009.08.013.

[185] Y.H. Seo, A. Benčan, J. Koruza, B. Malič, M. Kosec, K.G. Webber, Compositional dependence of R-curve behavior in soft $Pb(Zr_{1-x}Ti_x)O_3$ ceramics, J. Am. Ceram. Soc. 94 (2011) 4419–4425. doi:10.1111/j.1551-2916.2011.04889.x.

[186] H. Wang, A. Wereszczak, Effects of electric field on the biaxial strength of poled PZT, in: Adv. Electron. Ceram. Proc., 2008: pp. 57–67.

[187] T. Fett, D. Munz, Stress intensity factor and weight functions, Universitätsverlag Karlsruhe, Southampton, 1997. doi:10.5860/choice.35-2724.

[188] L. Sestakova, R. Bermejo, Z. Chlup, R. Danzer, Strategies for fracture toughness, strength and reliability optimisation of ceramic – ceramic laminates, Int. J. Mater. Reserach. 102 (2011) 613–627.

[189] Y. Tsuru, M. Shimazu, M. Shiono, M. Morinaga, Evaluation of linear thermal expansion coefficients of perovskite oxides using ab-initio molecular dynamics with small cell sizes for materials design, Jpn. J. Appl. Phys. 49 (2010) 0457011–15. doi:10.1143/JJAP.49.045701.

[190] S. Masys, V. Jonauskas, Elastic properties of rhombohedral, cubic, and monoclinic phases of $LaNiO_3$ by first principles calculations, Comput. Mater. Sci. 108 (2015) 153–159. doi:10.1016/j.commatsci.2015.06.034.

[191] S.G. Kim, S. Priya, I. Kanno, Piezoelectric MEMS for energy harvesting, MRS Bull. 37 (2012) 1039–1050. doi:10.1557/mrs.2012.275.

[192] S. Priya, H.-C. Song, Y. Zhou, R. Varghese, A. Chopra, S.-G. Kim, I. Kanno, L. Wu, D.S. Ha, J. Ryu, R.G. Polcawich, A review on piezoelectric energy harvesting: materials, methods, and circuits, Energy Harvest. Syst. 4 (2017) 3–39. doi:10.1515/ehs-2016-0028.

[193] T. Fett, D. Munz, G. Thun, Bending strength of a PZT ceramic under electric fields, J. Eur. Ceram. Soc. 23 (2003) 195–202. doi:10.1016/S0955-2219(02)00174-7.

[194] D. Munz, T. Fett, S. Mueller, G. Thun, Deformation and strength behavior of a soft PZT ceramic, SPIE Proc. Math. Control Smart Struct. 3323 (1998) 84–95. doi:10.1117/12.316289.

[195] P.H. Moon, The theory of thermal breakdown of solid dielectrics, Trans. Am. Inst. Electr. Eng. 50 (1931) 1008–1021. doi:10.1109/T-AIEE.1931.5055909.

[196] J.J. O'Dwyer, Chapter 6. thermal breakdown, in: Theory Dielectr. Break. Solids, Clarendon Press, Oxford, 1964: pp. 183–205.

[197] R.G. Polcawich, C. Feng, P. Vanatta, R. Piekarz, S. Trolier-McKinstry, M. Dubey, M. Ervin, Highly accelerated lifetime testing (HALT) of lead zirconate titanate (PZT) thin films, IEEE Int. Symp. Appl. Ferroelectr. 1 (2000) 357–360. doi:10.1109/isaf.2000.941571.

[198] M. Ritter, K. Coleman, R. Bermejo, S. Trolier-McKinstry, Effect of electrical history on the mechanical response of PZT thin films, Prep. (2020).

[199] EN 623-3 : "200x Advanced technical ceramics – Monolithic ceramics – General and textural properties - Part 3 : Determination of Grain Size and Size Distribution (Characterized by the Linear Intercept Method)," (n.d.) 1–21.

[200] R.H.T. Wilke, P.J. Moses, P. Jousse, C. Yeager, S. Trolier-McKinstry, Wafer mapping of the transverse piezoelectric coefficient, $e_{31,f}$, using the wafer flexure technique with sputter deposited Pt strain gauges, Sensors Actuators, A Phys. 173 (2012) 152–157. doi:10.1016/j.sna.2011.10.030.

[201] A. Börger, P. Supancic, R. Danzer, The ball on three balls test for strength testing of brittle discs: Stress distribution in the disc, J. Eur. Ceram. Soc. 22 (2002) 1425–1436. doi:10.1016/S0955-2219(01)00458-7.

[202] EN 843-5, "Advanced technical ceramics - Mechanical properties of monolithic ceramics at room temperature - Part 5: Statistical analysis," 1996., (n.d.).

[203] R.G. Polcawich, S. Trolier-McKinstry, Piezoelectric and dielectric reliability of lead zirconate titanate thin films, J. Mater. Res. 15 (2000) 2505–2513. doi:10.1557/JMR.2000.0360.

[204] W.-H. Xu, D. Lu, T.-Y. Zhang, Determination of residual stresses in $Pb(Zr_{0.53}Ti_{0.47})O_3$ thin films with Raman spectroscopy, Appl. Phys. Lett. 79 (2001) 4112. doi:10.1063/1.1426271.

[205] E. Buixaderas, M. Berta, L. Kozielski, I. Gregora, Raman spectroscopy of $Pb(Zr_{1-x}Ti_x)O_3$ graded ceramics around the morphotropic phase boundary, Phase Transitions. 84 (2011) 528–541. doi:10.1080/01411594.2011.552049.

[206] M. Deluca, H. Fukumura, N. Tonari, C. Capiani, N. Hasuike, K. Kisoda, C. Galassi, H. Harima, Raman spectroscopic study of phase transitions in undoped morphotropic $PbZr_{1-x}Ti_xO_3$, J. Raman Spectrosc. 42 (2011) 488–495. doi:10.1002/jrs.2714.

[207] P. Kaufmann, S. Röhrig, P. Supancic, M. Deluca, Influence of ferroelectric domain texture on the performance of multilayer piezoelectric actuators, J. Eur. Ceram. Soc. 37 (2017) 2039–2046. doi:10.1016/j.jeurceramsoc.2016.12.029.

[208] M. Deluca, G. Pezzotti, First-order transverse phonon deformation potentials of tetragonal perovskites, J. Phys. Chem. A. 112 (2008) 11165–11171. doi:10.1021/jp805278u.

[209] M. Deluca, R. Bermejo, H. Grünbichler, V. Presser, R. Danzer, K.G. Nickel, Raman spectroscopy for the investigation of indentation-induced domain texturing in lead zirconate titanate piezoceramics, Scr. Mater. 63 (2010) 343–346. doi:10.1016/j.scriptamat.2010.04.040.

[210] M. Osada, K. Nishida, S. Wada, S. Okamoto, R. Ueno, H. Funakubo, T. Katoda, Domain distributions in tetragonal $Pb(Zr,Ti)O_3$ thin films probed by polarized Raman spectroscopy, Appl. Phys. Lett. 87 (2005) 232902. doi:10.1063/1.2139844.

[211] S.H. Lee, H.M. Jang, S.M. Cho, G.C. Yi, Polarized Raman scattering of epitaxial $PbTiO_3$ thin film with coexisting c and a domains, Appl. Phys. Lett. 80 (2002) 3165–3167. doi:10.1063/1.1473864.

[212] N. Chaban, M. Weber, S. Pignard, J. Kreisel, Phonon Raman scattering of perovskite $LaNiO_3$ thin films, Appl. Phys. Lett. 97 (2010) 31913–31915. doi:10.1063/1.3464958.

[213] M. Kohli, P. Muralt, N. Setter, Removal of 90° domain pinning in (100) $Pb(Zr_{0.15}Ti_{0.85})O_3$ thin films by pulsed operation, Appl. Phys. Lett. 72 (1998) 3217–3219. doi:10.1063/1.121554.

[214] H. Morioka, K. Saito, H. Nakaki, R. Ikariyama, T. Kurosawa, H. Funakubo, Impact of 90°-domain wall motion in $Pb(Zr_{0.43}Ti_{0.57})O_3$ film on the ferroelectricity induced by an applied electric field, Appl. Phys. Express. 2 (2009) 0414011. doi:10.1143/APEX.2.041401.

[215] G. Esteves, C.M. Fancher, M. Wallace, R. Johnson-Wilke, R.H.T. Wilke, S. Trolier-McKinstry, R.G. Polcawich, J.L. Jones, In situ X-ray diffraction of lead zirconate titanate piezoMEMS cantilever during actuation, Mater. Des. 111 (2016) 429–434. doi:10.1016/j.matdes.2016.09.011.

[216] G. Esteves, M. Wallace, R. Johnson-Wilke, C.M. Fancher, R.H.T. Wilke, S. Trolier-McKinstry, J.L. Jones, Effect of mechanical constraint on domain reorientation in predominantly {111}-textured lead zirconate titanate films, J. Am. Ceram. Soc. 99 (2016) 1802–1807. doi:10.1111/jace.14159.

[217] S. Wurster, C. Motz, R. Pippan, Characterization of the fracture toughness of micro-sized tungsten single crystal notched specimens, Philos. Mag. 14 (2012) 1803–1825. doi:10.1080/14786435.2012.658449.

[218] B.S. Wurster, C. Motz, M. Jenko, R. Pippan, Micrometer-sized specimen preparation based on ion slicing technique, Adv. Eng. Mater. 12 (2010) 61–64. doi:10.1002/adem.200900263.

[219] A. Riedl, R. Daniel, M. Stefenelli, T. Scho, A novel approach for determining fracture toughness of hard coatings on the micrometer scale, Scr. Mater. 67 (2012) 708–711. doi:10.1016/j.scriptamat.2012.06.034.

[220] F. Laermer, A. Schilp, Method of anisotropically etching silicon, US Patent: 55018893, 1996.

[221] Y. Qiu, J. V. Gigliotti, M. Wallace, F. Griggio, C.E.M. Demore, S. Cochran, S. Trolier-McKinstry, Piezoelectric micromachined ultrasound transducer (PMUT) arrays for integrated sensing, actuation and imaging, Sensors. 15 (2015) 8020–8041. doi:10.3390/s150408020.

[222] A. Gruverman, B.J. Rodriguez, A.I. Kingon, R.J. Nemanich, A.K. Tagantsev, J.S. Cross, M. Tsukada, Mechanical stress effect on imprint behavior of integrated ferroelectric capacitors, Appl. Phys. Lett. 83 (2003) 728–730. doi:10.1063/1.1593830.

[223] Y. Zhou, H.K. Chan, C.H. Lam, F.G. Shin, Mechanisms of imprint effect on ferroelectric thin films, J. Appl. Phys. 98 (2005) 024111. doi:10.1063/1.1984075.

[224] A.K. Jonscher, Chapter 8. thermally stimulated depolarisation, in: Univers. Relax. Law, Chelsea Dielectrics Press, London, 1995: pp. 233–250.

[225] B. Akkopru-Akgun, The role of defect chemistry in DC resistance degradation of lead zitconate titanate thin films, The Pennsylvania State University, 2019.

[226] P. Dash, Dynamics of space charge polarization and electrical conduction in low alkali boroaluminosilicate glasses, The Pennsylvania State University, 2013.

[227] B. Akkopru-Akgun, W. Zhu, C.A. Randall, M.T. Lanagan, S. Trolier-McKinstry, Polarity dependent DC resistance degradation and electrical breakdown in Nb doped PZT films, APL Mater. 7 (2019) 120901. doi:10.1063/1.5115391.

[228] A. Abdul-Aziz, Durability modeling review of thermal- and environmental-barrier-coated fiber-reinforced ceramic matrix composites part I, Materials (Basel). 10 (2018) 1251. doi:10.3390/ma11071251.

[229] F. Traina, M. De Fine, A. Di Martino, C. Faldini, Fracture of ceramic bearing surfaces following total hip replacement: A systematic review, Biomed Res. Int. 2013 (2013) 157247. doi:10.1155/2013/157247.

[230] K. Wang, F. Zhang, R.K. Bordia, FEM modeling of in-plane stress distribution in thick brittle coatings/films on ductile substrates subjected to tensile stress to determine interfacial strength, Materials (Basel). 11 (2018) 497. doi:10.3390/ma11040497.

[231] J. Li, D. Leguillon, Finite element implementation of the coupled criterion for numerical simulations of crack initiation and propagation in brittle materials, Theor. Appl. Fract. Mech. 93 (2018) 105–115. doi:10.1016/j.tafmec.2017.07.010.

[232] D. Leguillon, J. Li, E. Martin, Multi-cracking in brittle thin layers and coatings using a FFM model, Eur. J. Mech. A/Solids. 63 (2017) 14–21. doi:10.1016/j.euromechsol.2016.12.003.

[233] W.L. Johnson, S.A. Kim, G.S. White, J. Herzberger, K.L. Peterson, P.R. Heyliger, Time-domain analysis of resonant acoustic nonlinearity arising from cracks in multilayer ceramic capacitors, AIP Conf. Proc. 1706 (2016) 060005. doi:10.1063/1.4940511.

[234] T.L. Baker, S.W. Freiman, Fracture behaivor of ceramics used in multilayer capacitors, MRS Proc. 72 (1986) 81–90. doi:10.1557/PROC-72-81.

[235] M. Keimasi, M.H. Azarian, M. Pecht, Isothermal aging effects on flex cracking of multilayer ceramic capacitors with standard and flexible terminations, Microelectron. Reliab. 47 (2007) 2215–2225. doi:10.1016/j.microrel.2006.12.005.

Appendix

Chapter 4: First, Second, and Third Harmonics of Dielectric Displacement, Permittivity, and Phase Angles for PZT on Ni and Si:
    Only the first three harmonics were collected in this study and used in these calculations

1. **First, Second, and Third Harmonics of Dielectric Displacement, Permittivity, and Phase Angles for PZT on Ni and Si:**
    Only the first three harmonics were collected in this study and used in these calculations
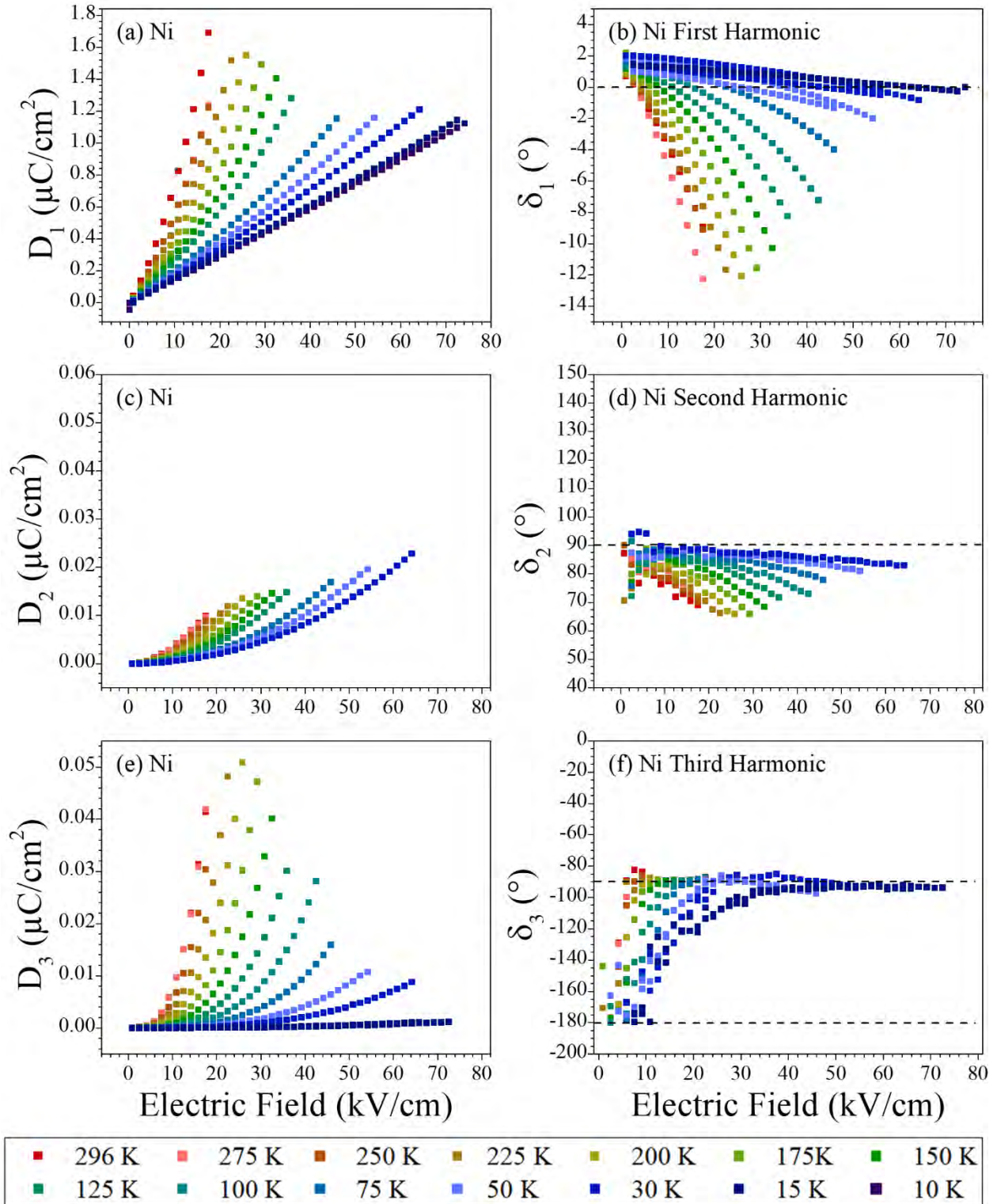
Figure SI.1- The dielectric displacement (D) for the first (a), second (c), and third (e) harmonic and phase angles (b, d, f, respectively) for PZT on Ni.
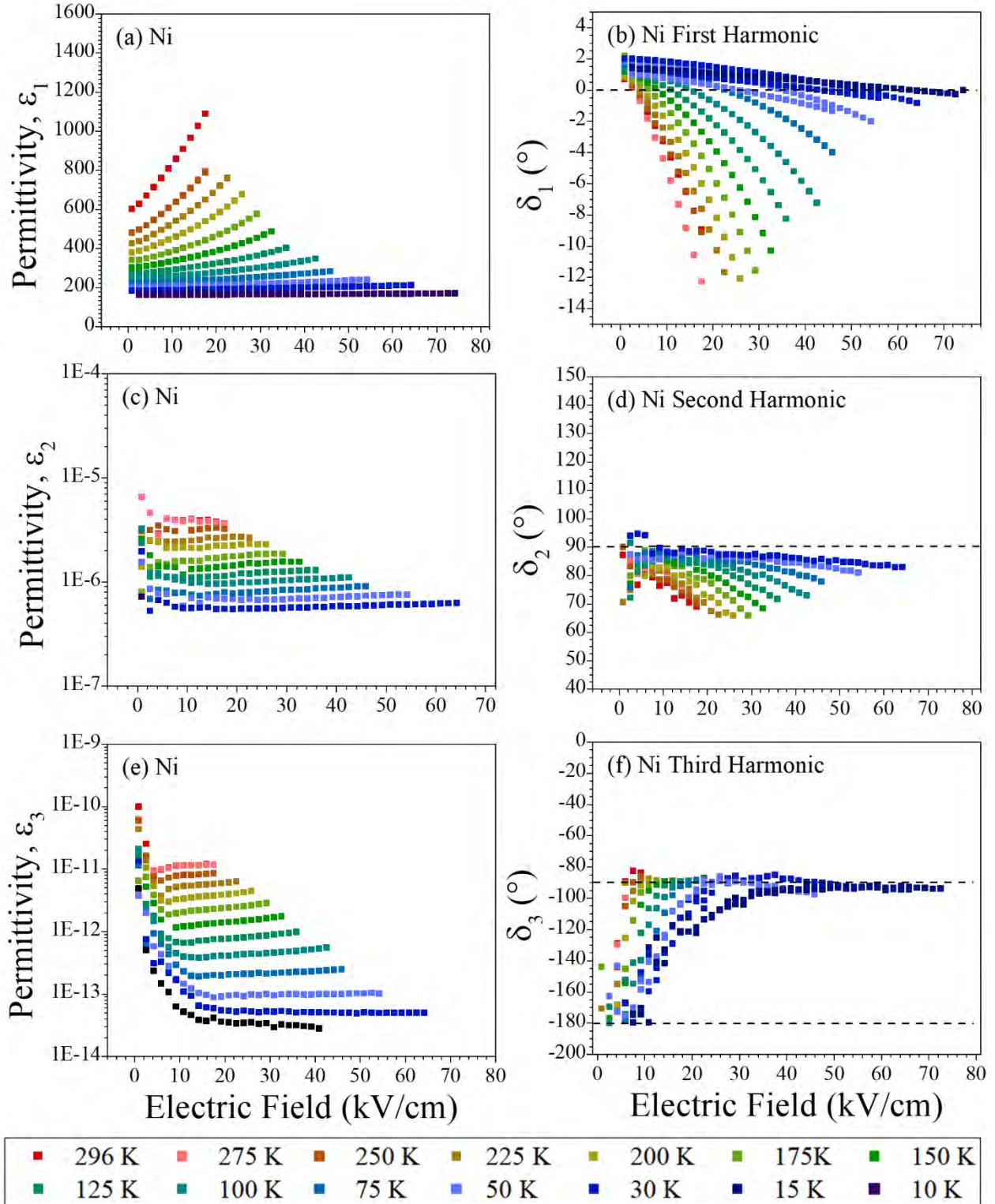
Figure SI.2- The permittivity's first (a), second (c), and third (e) harmonic and phase angles (b, d, f, respectively) for PZT on Ni.
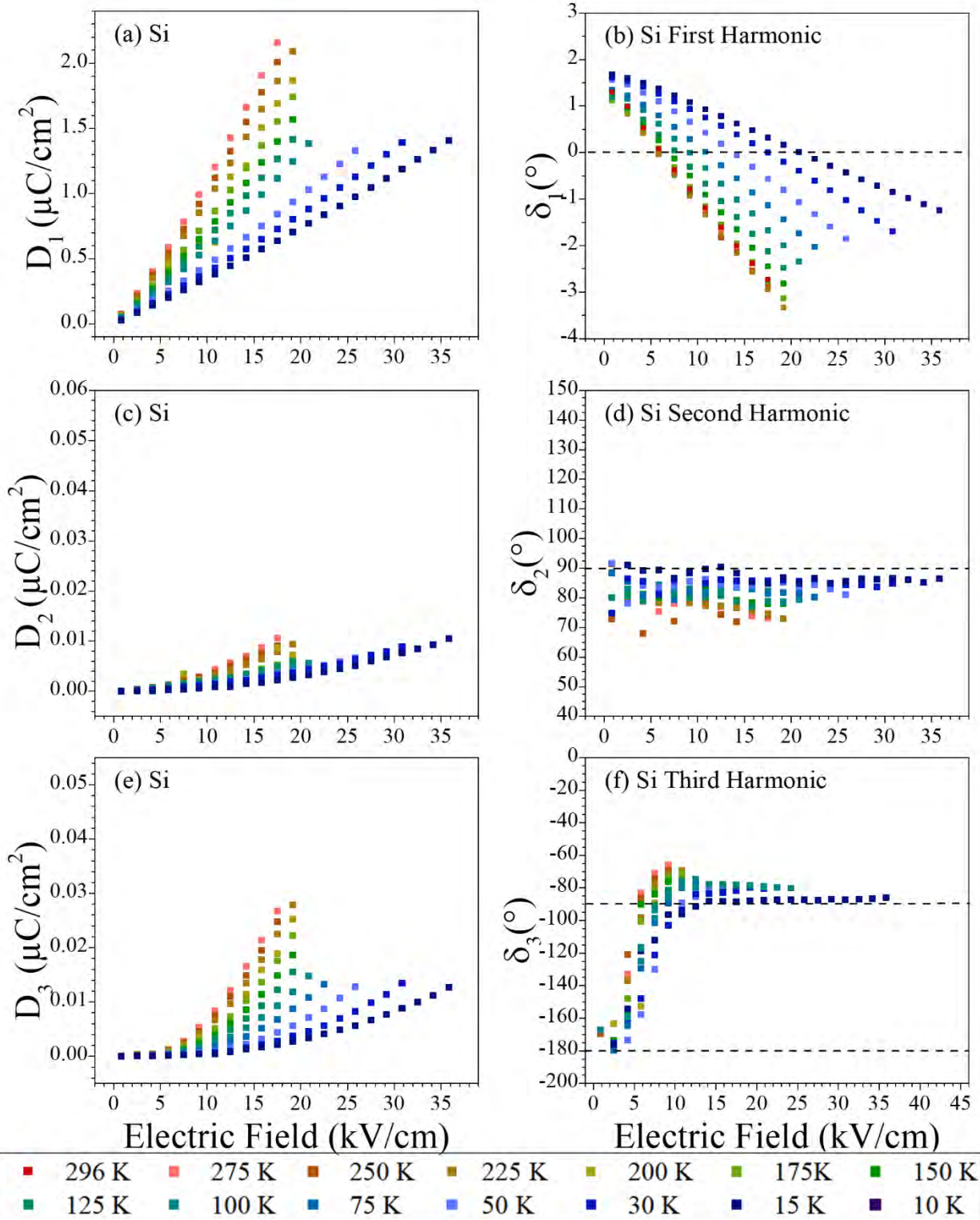
Figure SI.3- The dielectric displacement (D) for the first (a), second (c), and third (e) harmonic and phase angles (b, d, f, respectively) for PZT on Si.
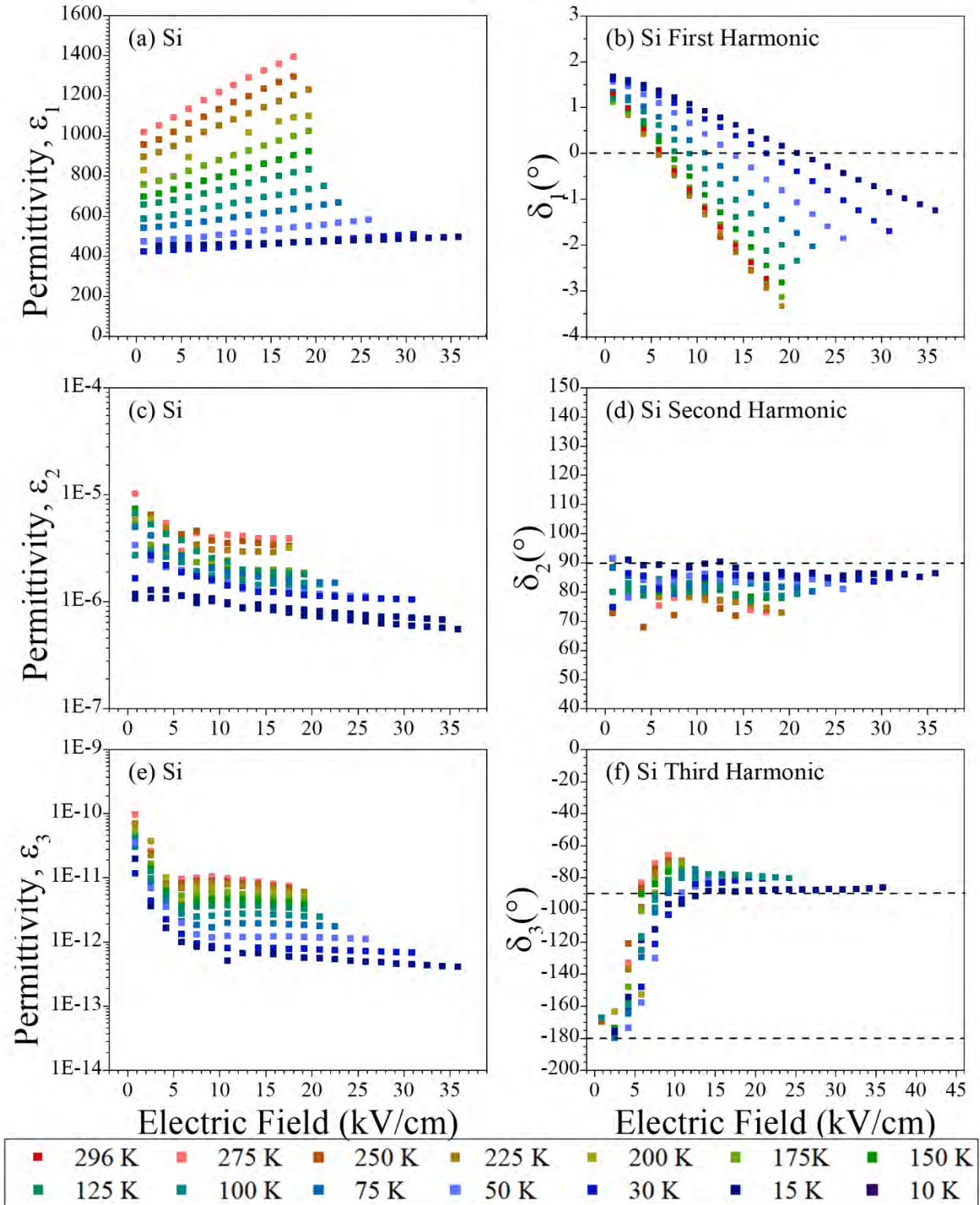
Figure SI.4- The permittivity's first (a), second (c), and third (e) harmonic and phase angles (b, d, f, respectively) for PZT on Si.

VITA

Kathleen Coleman

Kathleen Coleman was born in to Josie and Brian Coleman and grew up in Pearl River, NY with her older brother, Michael, and younger sister, Maryanne. Kathleen graduated Pearl River high school in June 2012. In July, Kathleen began her studies at the University of Connecticut in the Bridge Engineering Diversity Program. After switching majors five times, she pursued her bachelor in Materials Science and Engineering with a minor in Mathematics. In May 2016, Kathleen received her bachelors of science and engineering *summa cum lauda.* In August 2016, Kathleen joined Professor Susan Trolier-McKinstry's group at the Pennsylvania State University. Upon graduation, Kathleen will work at the Army Research Lab.